EXPERIMENTAL AND COMPUTATIONAL INVESTIGATION OF THE MICROSTRUCTURE-MECHANICAL DEFORMATION RELATIONSHIP IN POLYCRYSTALLINE MATERIALS, APPLIED TO ADDITIVELY MANUFACTURED TITANIUM ALLOYS

Submitted in partial fulfillment of the requirements for the degree of

Doctor of Philosophy

in

Materials Science and Engineering

Tugce Ozturk

B.S., Mechanical Engineering, Koc University
M.S., Materials Science and Engineering, Carnegie Mellon University

Carnegie Mellon University
Pittsburgh, PA

May 2017

Dedicated to my birth family, Gokce, Nurdan, Ugur,

and my new family, Evan

Abstract

Parts made out of titanium alloys demonstrate anisotropic mechanical properties when manufactured by electron beam melting, an emerging additive manufacturing technique. Understanding the process history dependent heterogeneous microstructure, and its effect on mechanical properties is crucial in determining the performance of additively manufactured titanium alloys as the mechanical behavior heavily relies on the underlying microstructural features. This thesis work focuses on combined experimental and computational techniques for microstructure characterization, synthetic microstructure generation, mechanical property measurement, and mechanical behavior modeling of polycrystalline materials, with special focus on dual phase titanium alloys. Macroscopic mechanical property measurements and multi-modal microstructure characterizations (high energy X-ray diffraction, computed tomography and optical microscopy) are performed on additively manufactured Ti-6Al-4V parts, revealing the heterogeneity of the microstructure and properties with respect to the build height. Because characterizing and testing every location within a build is not practical, a computational methodology is established in order to reduce the time and cost spent on microstructure-property database creation. First a statistical volume element size is determined for the Fast Fourier Transform based micromechanical modeling technique through a sensitivity study performed on an experimental Ni-based superalloy and synthetic W, Cu, Ni and Ti structures, showing that as the contrast of properties (e.g., texture, field localization, anisotropy, rate-sensitivity) increases, so does the minimum simulation domain size requirement. In all deformation regimes a minimum volume element is defined for both single and dual phase materials. The database is then expanded by generating statistically representative Ti structures which are modified for features of interest, e.g., lath thickness, grain size and orientation distribution, to be used in spectral full-field micromechanical modeling. The relative effect of the chosen microstructural features is quantified through comparisons of average and local field distributions. Fast Fourier transform based technique, being a spectral, full-field deformation modeling tool, is shown to be capable of capturing the relative contribution from varying microstructural features such as phase fractions, grain morphology/size and texture on the overall mechanical properties as the results indicate that the mean field behavior is predominantly controlled by the alpha phase fraction and the prior beta phase orientation.

ACKNOWLEDGEMENTS

There are many people I wish to thank for their help, guidance, support, love and friendship during my time in graduate school. I feel indebted to everyone for making this journey possible and successful for me, which has certainly been a group effort. First and foremost, I would like to thank my advisor, Tony Rollett, for his support, patience and invaluable guidance during my time at Carnegie Mellon University. His endless support for his students' professional development and love of science made me the researcher I am today. Thanks to him, today I am proud to call myself not only an engineer, but also a passionate scientist. I would also like to thank the members of my committee, Liz Holm, Bryan Webler and Bob Suter for their time and efforts in guiding the work presented in this thesis document. Especially Prof. Suter's guidance and help in advanced characterization has been vital for this thesis work and my personal research career. Thank you to my professors in the undergraduate mechanical engineering program at Koc University, namely Demircan Canadinc and Murat Sozer, for igniting my interest in research. I would like to thank and acknowledge Sector-1 beamline scientists at Advanced Photon Source, Dr. Jun-Sang Park and Dr. Peter Kenesei for their countless hours of assistance, and Dr. Ricardo Lebensohn for his invaluable advice on computational mechanics. I extend a special thank and appreciation to Dr. David Menasche, who mentored, assisted and accompanied me even at 400^{th} hour of beamtime, and from whom I learned countless tips and tricks for diffraction microscopy.

The members of the Rollett research group, past and present, are profoundly thanked for generously sharing their expertise, time and insights: Dr. Samikshya Subedi, Sudipto Mandal, Shivram Kashyap, Ross Cunningham, Dr. Brian Lin, Dr. Brian Gockel, Dr. Ben Anglin, Dr. Reeju Pokharel, Dr. Sean Donegan, Dr. Clay Stein and Dr. Vahid Tari to name a few. Without them, this journey would not have been as valuable and enjoyable as it has been. A big, sincere thank you goes to my friends I gained during graduate school: Megha, Samikshya, Basak, Lezgin, all of the Brians,

Sudipto, Ankita, Dave, Shivram, Sila, Eylul, Ekin, and Togan for being great friends throughout grad school to share my successes and failures. The continued friendship and support of my friends from Turkey has and will always mean a lot. Thank you to Ozgecan Atasoy, Ozge Cakir, Cansu Bilge, all members of Ev group, Gencay Cubuk and many more. Thank you to my new family, the Knutsons, for your support. Lori and Charles, thank you for accepting me in to your family as one of your own. Karen, thank you for your friendship and happy horas. To my biggest fans, my support system, my band of joy, my family: thank you, Mom, Dad, and Gokce for all the unconditional love and endless support. I cannot begin to thank them enough for everything they have done for me, as without them I would not have been where I am today. Lastly, the biggest thank you goes to the best part of Pittsburgh: To my best friend, my companion, my partner in crime and in life Evan Knutson. Thank you, Evan, for everything: For always being understanding, loving and supportive, for spending your weekends with me in coffee shops, for making me a better person and a better researcher. You are my biggest fan, as I am yours.

This thesis work is supported by the National Science Foundation, under the award number DMREF-1435544. Partial support by AFOSR Discovery Challenge Thrust grant number FA9550-10-1-0213 is also acknowledged. For computing resources, this research extensively used local computer clusters and resources of the National Energy Research Scientific Computing Center, a DOE Office of Science User Facility supported by the Office of Science of the U.S. Department of Energy under Contract No. DE-AC02-05CH11231. Use of the Advanced Photon Source was supported by the Office of Science of the U. S. Department of Energy under contract No. DE-AC02-06CH11357, The use of the Materials Characterization Facility at Carnegie Mellon University by grant MCF-677785 is also acknowledged.

Tugce Ozturk
Pittsburgh, PA
May 2017

List of Publications

Directly resulted from this dissertation work:

1. Ozturk T., Stein C., Pokharel R. et al. (2016). "Simulation domain size requirements for elastic response of 3D polycrystalline materials". *Modeling and Simulation in Materials Science and Engineering*, 24,015006.

2. Ozturk, T., Rollett, A.D. (2017) "Effect of microstructure on the elasto-viscoplastic deformation of dual phase titanium structures." *Computational Mechanics*, in review.

3. Ozturk, T., Menasche D., Suter R, Rollett A.D. (2017). "Synchrotron based high energy X-Ray diffraction characterization of 3D printed dual-phase titanium alloys." *Applied Crystallography*, in preparation.

4. Ozturk, T., Gong X., Cong S. et al. (2017). "Multiscale mechanical property measurement and microstructural characterization of additively manufactured Ti-6Al-4V components." *Additive Manufacturing*, in preparation.

Supported by this dissertation work:

1. Stein C., Cerrone A, Ozturk T. et al. (2014). "Fatigue crack initiation, slip localization and twin boundaries in a nickel-based superalloy." *Current Opinion in Solid State and Materials Science*, 18:244-252.

2. Cunningham R., Narra S.P., Ozturk T. et al. (2016). "Evaluating the effect of processing parameters on porosity in e-beam melted Ti-6Al-4V via synchrotron X-ray microtomograpy." *JOM*, 68(3):1-7.

3. Rao S., Cunningham R., Ozturk T, Rollett A.D. (2016). "Measurement and analysis of porosity in Al-10Si-1Mg components additively manufactured by selective laser melting." *Materials Performance and Characterization*, 5(5):701-716.

TABLE OF CONTENTS

LIST OF TABLES

LIST OF FIGURES

LIST OF SYMBOLS AND ABBREVIATIONS

AM	additive manufacturing
$3D$	three dimensional
$EBSD$	electron backscatter diffraction
α	hexagonal closed packed alpha phase of titanium
β	body centered cubic beta phase of titanium
$HEDM$	high energy X-ray diffraction microscopy
nf	near-field
ff	far-field
FFT	fast Fourier transform
CT	computed tomography
OM	optical microscopy
EBM	electron beam melting
$SRVE$	statistically representative volume element
DOF	degrees of freedom
$VPSC$	visco-plastic self consistent
fcc	face centered cubic
bcc	body centered cubic
hcp	hexagonal closed packed
RD	rolling direction
TD	transverse direction
ND	normal direction
ODF	orientation distribution function
MDF	misorientation distribution function

MRD	multiples of random distribution
GND	geometrically necessary dislocation
$CPFEM$	crystal plasticity finite element model
BOR	Burger's orientation relationship
YS	yield stress
UTS	ultimate tensile stress
$ICME$	integrated computational materials engineering
CAD	computer aided design
SC	self-consistent
FEM	finite element model
$CRSS$	critical resolved shear stress
DCT	diffraction contrast tomography
$3DXRD$	3D X-ray diffraction microscopy
$DAXM$	differential aperture X-ray microscopy
APS	advanced photon source
SEM	secondary electron microscope
BSE	back-scattered electron
XCT	X-ray computed tomography
KAM	kernel average misorientation
IPF	inverse pole figure
EDM	electrical discharge machine
$ANOVA$	analysis of variance
SVE	statistical volume element
RVE	representative volume element
$MSFC$	microstructurally small fatigue crack
SRM	statistically representative microstructure
(x,y,z)	orthonormal sample reference frame
$[uvw]$	crystal directions
(hkl)	crystal plane

$(e1, e2, e3)$	crystal reference frame
(ϕ_1, Φ, ϕ_2)	Euler angles
g_{ij}	rotation matrix
$(\hat{r}, \theta)$	axis-angle pair
$\rho = \hat{r}\tan(\frac{\theta}{2})$	Rodrigues-Frank vector
$q = (q_0, q_1, q_2, q_3)$	unit quaternion
Δg_{AB}	misorientation
g_A	orientation of crystal A
O_c	symmetry operator
$_{ijkl}$	denotes tensors
$(x), (w)$	local values in real and Fourier space
$\hat{}$	Fourier space values
$\dot{}$	denotes rates
σ_{ij}	stress tensor
ε_{ij}	strain tensor
C_{ijkl}	stiffness tensor
N	number of grid points
u	displacement gradient
τ_{ij}	fluctuation from average stress
$\hat{G}$	Green's function
ω	frequency in Fourier space
E	macroscopic strain
σ'	deviatoric stress
p	hydrostatic pressure
v	velocity
E_{tan}	tangent modulus
M^{tg}	tangent compliance
L^{tg}	tangent stiffness
d (x)	local strain rate

S^o	back extrapolated stress
$\Sigma'(x)$	homogenized reference medium
L_o^{tg}	medium stiffness
S^{oo}	medium back extrapolated stress
D	medium strain rate
$\vec{n}$	slip plane normal
$\vec{b}$	slip plane direction
R	transformation matrix for slip to crystal frame
m_{ij}	Schmid tensor
ε_{ij}^{slip}	strain tensor in slip coordinate system
γ	shear strain
τ	resolved shear stress
$\dot{\gamma}^s$	shear rate on slip system s
$\dot{\gamma}_o$	normalization factor
n	1/rate sensitivity
$\tau_0^s(x)$	critical resolved shear stress
δ_{ij}	Kronecker delta
ε^e	elastic strain
ε^p	plastic strain
w_{ij}	reorientation tensor
$\dot{w}_{ij}$	rigid body rotation rate tensor
$\dot{w}_{ij}^p$	plastic rotation rate tensor
$\alpha^s(x)$	local skewsymmetric Schmid tensor
τ_0^S	initial critical resolved shear stress
τ_1^S	initial hardening rate
θ_0^S	asymptotic hardening rate and
θ_1^S	back-extrapolated critical resolved shear stress
L	nf-HEDM detector to sample distance

j	horizontal point of intersection of the focused X- ray beam and the rotation axis on the detector
k	vertical point of intersection of the focused X- ray beam and the rotation axis on the detector
λ	wavelength
Q	scattering vector
G	reciprocal lattice vector
k	wavevector
C	nf-HEDM fit confidence
$N_{overlap}$	number of simulated peaks that overlap with the peak from the segmented image
$N_{simulated}$	total number of peaks observed in more than one detector distance
F	test statistic value
p	significance value
r	Pearson's correlation coefficient

CHAPTER I

Introduction

1.1 Motivation

Powder-bed based additive manufacturing (AM) of metallic components, in which a three dimensional (3D) shape is written into successive layers of powder using an electron or laser beam under computer control, is increasingly being implemented to produce structural parts. Having a wide range of application in the aerospace, automotive and medical industries, AM of titanium components is now valued because of the near-net shape end product, green manufacturing initiatives and reduced machining cost advantages of the technique [1]. Although emergent AM techniques provide certain advantages, location specific rapid cooling rates and thermal spikes caused by the scanning beam makes the process stochastic in nature and introduces obscurity in part quality and mechanical properties. Furthermore, with titanium being an allotropic element that can exist in more than one crystallographic form depending on the chemo-thermo-mechanical process, and it exhibiting a variety of distinct microstructures such as fully lamellar, duplex, or fully equiaxed as a function of the thermomechanical history [2–4], the heterogeneity in AM process history through large thermal gradients and local cooling rates inherently makes for challenges in the prediction of microstructure and mechanical properties of printed titanium alloys.

While there are established structure - property relationships for conventionally manufactured alpha/beta titanium alloys [5–9], studies on additively fabricated components are found to report a wide range of values, and suffer lack of detailed information, whether in terms of processing parameters or build geometry, both of which significantly affect the properties [10–13, 15, 16]. Moreover, due to time and budget restrictions and practical difficulties it is not possible to characterize and test each and every location in the build that undergoes a different thermal history. Compounding the

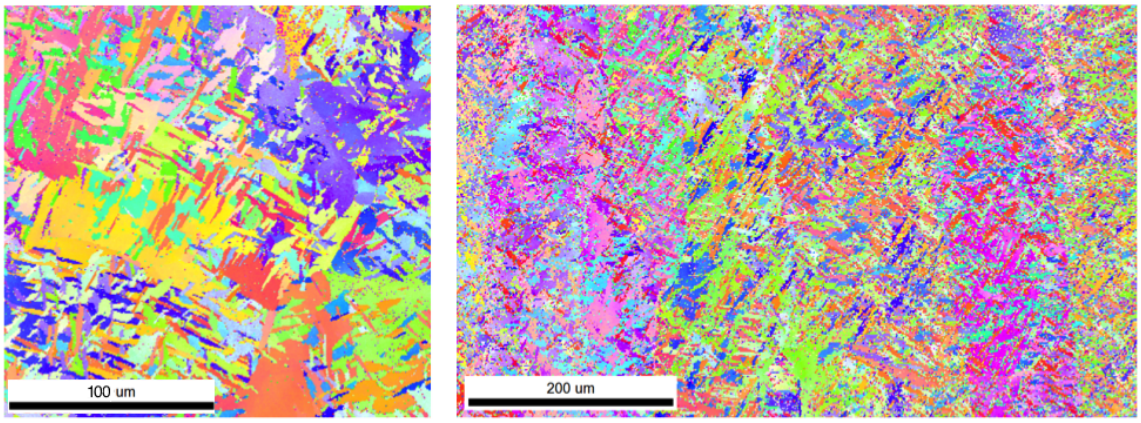

(a) XY surface (b) YZ surface

Figure 1.1: EBSD orientation maps of an as-built AM Ti-6Al-4V, for build direction Z. Average β size is 100 μm and average α size is few μm [EBSD by Ross Cunningham].

problem are the challenges in the characterization of these materials that are either textured or exhibits spatially varying residual stress. As an example, one of the most common characterization techniques, electron back scatter diffraction (EBSD) can be used to evaluate the heterogeneous microstructure of additively manufactured Ti-6Al-4V alloys, Fig.1.1. However since the solidification path can be complicated as a result of subsequent beam passes, the resulting microstructures are highly heterogeneous lamellar $\alpha - \beta$ structures with either a basket weave or a colony α structure which are different in size and morphology in different regions [12]. Hence, from the experimental perspective it is important to characterize large sample regions from different locations to define statistical volume elements, and from the computational perspective it is essential to establish comprehensive and statistically representative models to capture the anisotropic mechanical response.

1.2 Objective

This thesis work focuses on combined experimental and computational techniques for polycrystalline materials' microstructure-property investigation with specific focus on additively manufactured titanium, Fig.1.2, and database generation that can be utilized in designing new process maps and material systems for AM when a particular set of properties are targeted beyond the traditional alloy systems such as Ti-6Al-4V. The experimental part of the dissertation is the non-destructive high energy X-ray diffraction microscopy (HEDM), computed tomography (CT) and optical microscopy (OM) characterization, as well as location specific tensile property measurements of ad-

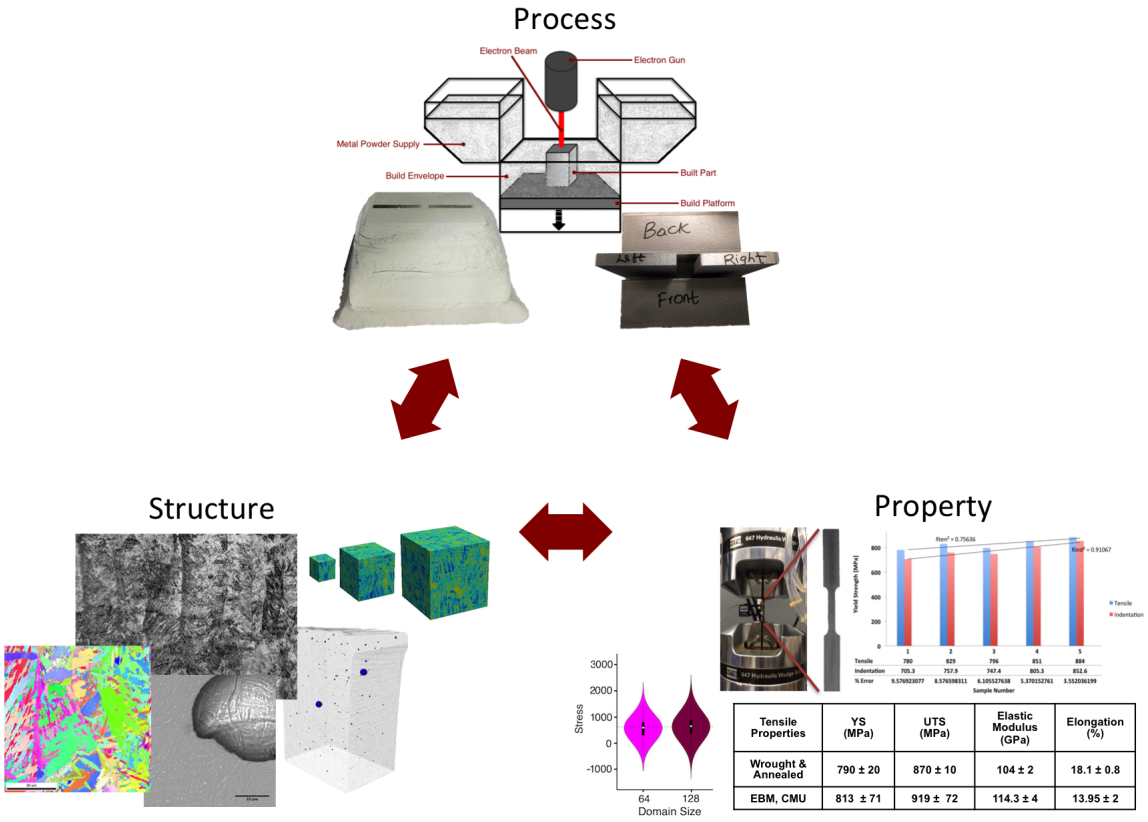

Tensile Properties	YS (MPa)	UTS (MPa)	Elastic Modulus (GPa)	Elongation (%)
Wrought & Annealed	790 ± 20	870 ± 10	104 ± 2	18.1 ± 0.8
EBM, CMU	813 ± 71	919 ± 72	114.3 ± 4	13.95 ± 2

Figure 1.2: Process-structure-property investigation via experimental and computational techniques

ditively fabricated Ti-6Al-4V parts in order to understand the process and location dependent grain structure characteristics and mechanical properties. The computational part is establishing and testing a methodology to create statistically representative dual phase titanium microstructures, specifically additively fabricated Ti-6Al-4V representative structures, and the investigation of the micromechanical field development and the resulting overall properties via the Fast Fourier Transform (FFT) based micromechanical modeling technique to quantify the relative effect of individual microstructure descriptors and to generate the structure-property database.

1.3 Methods and Approach

The heterogeneous microstructure characteristics of Ti-6Al-4V that is manufactured via powder bed based electron beam melting (EBM) process is characterized using both synchrotron and visible light sources. For fast, non-destructive and 3D grain/porosity structure measurements, high-energy X-ray diffraction and high-energy X-ray tomography experiments are performed at Advanced Pho-

ton Source (APS). Samples with different AM processing and post-processing conditions are characterized for investigating the effect of processing parameters on microstructural evolution. Characterization results are then used to determine regions of interest for mechanical property measurements. Macroscopic tensile tests are performed on samples cut from different build locations. Microstructure paired spatial hardening parameters are extracted from experimental results, which are then used in the computational study. The micromechanical deformation of elastic, viscoplastic and elasto-viscoplastic regimes is modeled via the FFT based technique. A statistically representative volume element (SRVE) size is determined for all regimes, both using an experimentally measured HEDM data and synthetically reconstructed microstructures. Results of the sensitivity analysis are used to inform the virtual microstructure reconstruction of dual phase titanium alloys with varying grain sizes, grain morphologies, phase fractions and crystallographic orientations. The computational approach of concurrent synthetic microstructure generation and micromechanical modeling is performed to establish the microstructure-deformation relationship for dual-phase AM representative titanium.

1.4 Hypotheses

As emphasized with the title, the main focus of this thesis work is the investigation of the microstructure-mechanical deformation relationship of polycrystalline materials, specifically additively manufactured titanium, using combined computational and experimental techniques by means of the following hypotheses:

i) Multi-modal microstructure characterization and mechanical behavior measurements are expected to reveal the heterogeneous microstructure and properties along the build height of powder bed based electron beam melting Ti-6Al-4V parts. Due to expected larger alpha platelets at the top of the build [16, 17], decreased yield and tensile strength and increased elongation is anticipated in relation to build direction. Based on the work by Gockel [14], in extracting the location specific material hardening parameters from the tensile stress-strain curves, the Voce hardening model is expected to predict the behavior with less than 10% error.

ii) For increasing the computational efficiency of the FFT based algorithm as a micromechanical modeling technique to study the microstructure-deformation relationship, a simulation domain

size sensitivity study is proposed with the expectation of finding a strong relation between a minimum required simulation domain size, i.e. number of grains included in the calculation, and the contrast ratio of properties for the elastic, viscoplastic and elasto-viscoplastic regimes. Finding a Pearson correlation coefficient r = 0.99 is anticipated when the downsampled simulation results are compared to one another and the largest sized domain.

iii) Being a spectral, image-based, meshless full-field deformation modeling tool, FFT is expected to be able to simulate the large element count and correspondingly large number of degrees of freedom (DOF) two-phase lamellar structures of > 100 parent grain plus > 50000 daughter grain composites, and to predict the stress-strain behavior by capturing the relative contribution from varying microstructural features such as phase fractions and texture on both the macroscale effective and mesoscale spatial properties.

The first part of the hypothesis is tested by performing combined tensile property measurements and optical microscopy/high energy x-ray diffraction microscopy characterizations, investigating the heterogeneity with respect to build height. The tensile data is then used to extract material hardening parameters along the build height, by iteratively comparing the Visco-Plastic Self Consistent (VPSC) simulation results with experimental data and finding the optimized set of parameters by a non-linear least-squares formulation. The second part of the hypothesis, the sensitivity of the FFT method to the number of surrounding grains, is tested through quantification of the divergence of the field values from the largest simulation domain, as successively smaller surrounding volumes are included in the simulation. The importance of property contrast is tested by varying anisotropy, texture and constitutive equations (e.g., elastic vs. viscoplastic regimes). The last part of the hypothesis is tested by creating statistically representative 2-phase Ti structures on a spectrum of microstructural features, and simulating the elasto-viscoplastic deformation to capture the effect phase fraction, phase morphology/size and texture on the mechanical response.

CHAPTER II

Background

The following chapter presents the background on the microstructural representation and mechanical behavior of polycrystalline materials, and general characteristics of titanium and its alloys. The chapter then closes with a literature review of the process-structure-property relationship of titanium, with specific focus on electron beam additive manufacturing and Ti-6Al-4V alloy.

2.1 Microstructural Representation of Polycrystals

2.1.1 Crystal structure

Polycrystalline materials are composed of many crystals (also known as grains), oriented in certain ways in a microstructure whose constituents such as atomic or molecular arrangement is highly ordered, forming an array of unit cells extending in all directions. This spatial arrangement of atoms in a crystal is known as crystal structure. Each crystal structure holds a unique arrangement of atoms, resulting in different atomic packing factors and close-packed directions/planes within the crystal unit cells [18]. For instance, face centered cubic (fcc) elements are usually found to be more ductile than body centered cubic (bcc) or hexagonal closed packed (hcp) elements. Furthermore, both lattice strains and slip activity where dislocations can easily move and cause plastic deformation are associated with certain directions, such as densely packed planes and/or directions, causing crystals to have anisotropic elastic and plastic properties [19]. Single crystal property anisotropy is either translated to the polycrystalline level in the existence of preferred orientation, known as texture, or the directionality is averaged by the abundance of randomly oriented crystals that form the polycrystal [20].

2.1.2 Orientation representations

Polycrystalline materials exhibit anisotropy under external loading as both the elastic and plastic material properties are usually directional. Hence, crystallographic orientation representation is one of the most important microstructure descriptors when interest is in relating microstructural features to mechanical behavior. Crystallographic orientation, g, is defined by three dimensional rotations from the crystal reference frame to the sample reference frame. Since both the crystal and sample reference frames are defined and bounded by symmetry, an orientation is generally represented by a class of crystallographically equivalent rotations. For instance, 24 symmetry operators of cubic symmetry would cause 24 crystallographically equivalent orientations [20]. Working with crystallographic orientations may be challenging because of the different representations and conventions. For instance, the conversion of the hexagonal frame (4 miller index notation) into orthonormal frame (3 miller index notation) can either be performed as $x_{ort} = [10\bar{1}0]_{hex}$, $y_{ort} = [\bar{1}2\bar{1}0]_{hex}$, $z_{ort} = [0001]_{hex}$, or as $x_{ort} = [2\bar{1}\bar{1}0]_{hex}$, $y_{ort} = [01\bar{1}0]_{hex}$, $z_{ort} = [0001]_{hex}$. Another challenge comes from how inconsistent crystallographic orientation analysis softwares are in converting hexagonal frame to orthonormal frame, Fig. 2.1 [21]. Hence, in this thesis work careful attention is paid to be consistent and open about the notations, reference directions and representations while working with crystallographic orientation data.

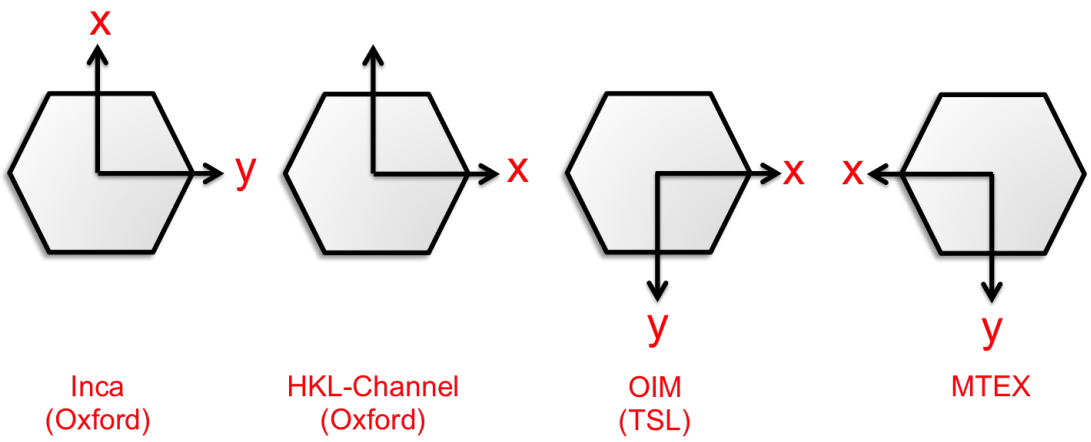

Figure 2.1: Visualization of the differences in hexagonal to orthonormal frame conversion for some of the commercial and open source crystallographic orientation analysis softwares [21].

As long as they are internally consistent, crystal orientations can be represented in multiple ways, each of which has its unique characteristics and advantages:

Miller indices: In this representation, all directions are described as linear combinations of the three orthogonal unit direction vectors that form the chosen reference frame. Using Miller indices as an orientation descriptor is the most straightforward and advantageous for orthonormal systems, e.g., cubic systems. In metallurgy, orthonormal directions of the sample reference frame are often taken as rolling direction (RD) ∥ x, transverse direction (TD) ∥ y, and normal direction (ND) ∥ z. Using metallographic directions, crystallographic orientation is represented by crystal direction [uvw] ∥ RD, and crystal plane (hkl) ∥ ND, Fig. 2.2, giving orientation as (hkl)[uvw] [19].

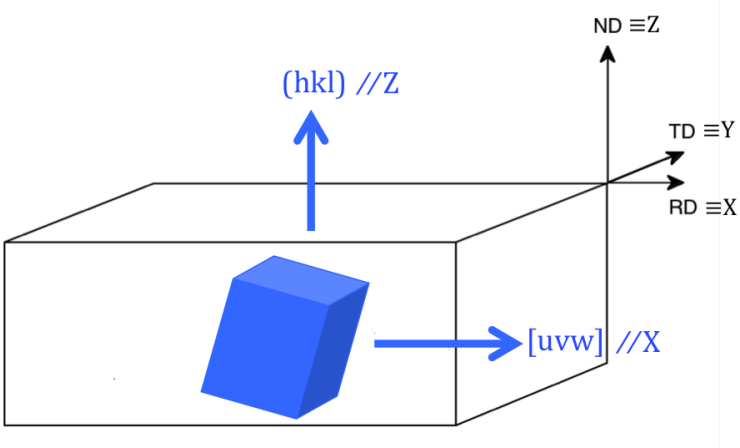

Figure 2.2: Orientation representation using Miller indices, (hkl)[uvw].

Euler angles: Transformation from the crystal reference frame (e_1, e_2, e_3) to the sample reference frame (RD, TD, ND) that brings the two coordinates into coincidence with each other is defined by three rotation angles, commonly represented by the Bunge [22], Roe [23], or Kocks [24] convention. Most common parameterization is the Bunge convention, where an anti-clockwise rotations of the following gives the final orientation of crystal by three Euler angles (ϕ_1, Φ, ϕ_2):

First the sample axes about ND by angle ϕ_1, such that, e_3 coincides with ND

Second the sample axes about RD by angle Φ, such that, e_1 coincides with RD

Third the sample axes about ND by angle ϕ_2, bringing e_3 in coincidence with ND.

Using the set of Bunge Euler angles, the rotation matrix describing an orientation can then be

written as

$$g_{ij} = \begin{pmatrix} \cos\phi_1\cos\phi_2 - \sin\phi_1\sin\phi_2\cos\Phi & \sin\phi_1\cos\phi_2 + \cos\phi_1\sin\phi_2\cos\Phi & \sin\phi_2\sin\Phi \\ -\cos\phi_1\sin\phi_2 - \sin\phi_1\cos\phi_2\cos\Phi & -\sin\phi_1\sin\phi_2 + \cos\phi_1\cos\phi_2\cos\Phi & \cos\phi_2\sin\Phi \\ \sin\phi_1\sin\Phi & -\cos\phi_1\sin\Phi & \cos\Phi \end{pmatrix} \tag{2.1}$$

While Bunge convention is the most widely known and used representation, e.g., how crystal orientation in represented in EBSD maps, constructing rotation matrices from Euler angles and performing orientation calculations through matrix multiplications, Eq. 2.4, is not computationally efficient.

Axis-angle pair: Axis-angle pair is defined such that the crystal frame and the external sample frame is overlapped by a single rotation, θ along a common axis, [uvw]. Commonly written as $(\hat{r}, \theta)$, axis-angle pair representation is the most commonly used misorientation descriptor, and it can very easily be converted to Rodrigues-Frank vectors by $\rho = \hat{r}\tan(\frac{\theta}{2})$, which are computationally efficient. Using the axis-angle pair, the rotation matrix can be formed as

$$g_{ij} = \delta_{ij}\cos\theta + r_i r_j(1-\cos\theta) + \sum_{k=1,3}\varepsilon_{ijk}r_k\sin\theta$$

$$g_{ij} = \begin{pmatrix} \cos\theta + u^2(1-\cos\theta) & uv(1-\cos\theta) + w\sin\theta & uw(1-\cos\theta) - v\sin\theta \\ uv(1-\cos\theta) - w\sin\theta & \cos\theta + v^2(1-\cos\theta) & vw(1-\cos\theta) + u\sin\theta \\ uw(1-\cos\theta) + v\sin\theta & vw(1-\cos\theta) - u\sin\theta & \cos\theta + w^2(1-\cos\theta) \end{pmatrix} \tag{2.2}$$

Unit quaternions: A quaternion is an ordered set of four real numbers, (q_0, q_1, q_2, q_3). Similar to axis-angle pair, the representation is by an angle θ and a unit vector n; $[n_1, n_2, n_3]$, giving the quaternion q and orientation matrix g as

$$q = (q_0, q_1, q_2, q_3) = \cos(\theta/2), \sin(\theta/2)n_1, \sin(\theta/2)n_2, \sin(\theta/2)n_3$$

$$g_{ij} = \begin{pmatrix} 1-2q_2^2-2q_3^2 & 2q_1q_2+2q_0q_3 & 2q_1q_3-2q_0q_2 \\ 2q_1q_2-2q_0q_3 & 1-2q_1^2-2q_3^2 & 2q_2q_3+2q_0q_1 \\ 2q_1q_3+2q_0q_2 & 2q_2q_3-2q_0q_1 & 1-2q_1^2-2q_2^2 \end{pmatrix} \tag{2.3}$$

Quaternions are computationally efficient as a result of their multiplication requiring very few

computations, and they are easily converted to/from axis-angle and Rodrigues-Frank representations.

2.1.3 Misorientation

Misorientation is defined by the minimum rotation required to bring two crystals in coincidence with each other, in other words the orientation of one crystal lattice with respect to another. Conceptually, for A and B being the crystals of interest this means rotating the crystal A first to a reference position, typically to (001) [100] that would align the (001) plane of the crystal with the z direction of the sample and [100] direction of the crystal with the x direction of the sample by the inverse of its orientation, followed by rotating the crystal A to the crystal B position by crystal B orientation, Fig. 2.3 [20]. Since misorientation by definition is the minimum rotation that brings two crystals

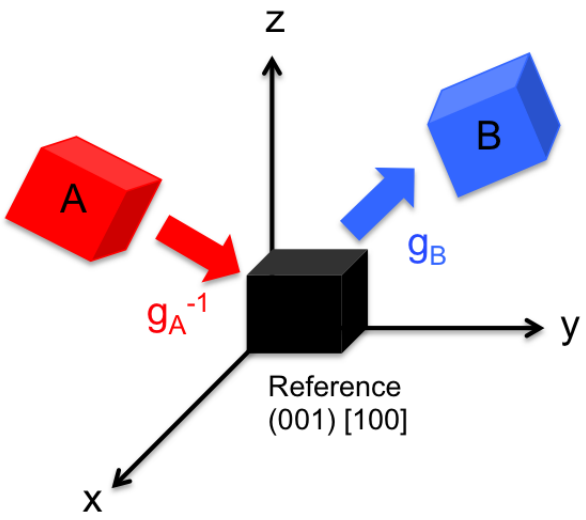

Figure 2.3: Schematic of misorientation representation between two grains

in coincidence, also referred to as disorientation, difference between all symmetrically equivalent orientations should be calculated by applying crystal symmetry operators on the orientations. That is, misorientation Δg_{AB} is defined by

$$\Delta g_{AB} = min[(O_c^A g_A)(O_c^B g_B)^{-1}] \tag{2.4}$$

where g_A and g_B are the orientations of crystals A and B and O_c is the symmetry operator. Since the choice of bringing crystal A to crystal B or B to A is arbitrary, there are 2 x O^2 equivalent mis-

orientations for two crystals. Misorientation is an important microstructural parameter because in orientation mapping of polycrystalline materials, grains are defined by grouping similarly oriented points together, after defining a threshold misorientation angle. Furthermore, it is one of the metrics used in quantifying defect accumulation of polycrystals through orientation gradients. Hence, orientation distributions, misorientation distributions, grain structures and mechanical behavior are closely associated.

2.1.4 Texture

Texture is defined as the average distribution of crystallographic orientations in polycrystals [20]. A material can either have a weak texture if the orientation distribution is random, or have a strong texture if there exist a preferred fiber orientation. Graphically, texture can be represented by pole figures, two dimensional stereographic projections of crystallographic plane normals with respect to the sample reference frame, plotted in crystal frame, or inverse pole figures, how sample coordinates are aligned with crystal coordinates, plotted in sample frame. The units of measure, either the orientation distribution function (ODF) or misorientation distribution function (MDF) measurements, is multiples of random distribution (MRD), indicating texture when the value is different than 1. Quantitative texture representation is important because the both the orientation and axis directionality of grains strongly affects the overall mechanical response of materials, as a result of anisotropic nature.

Summary of orientation and misorientation descriptors are presented in Fig. 2.4.

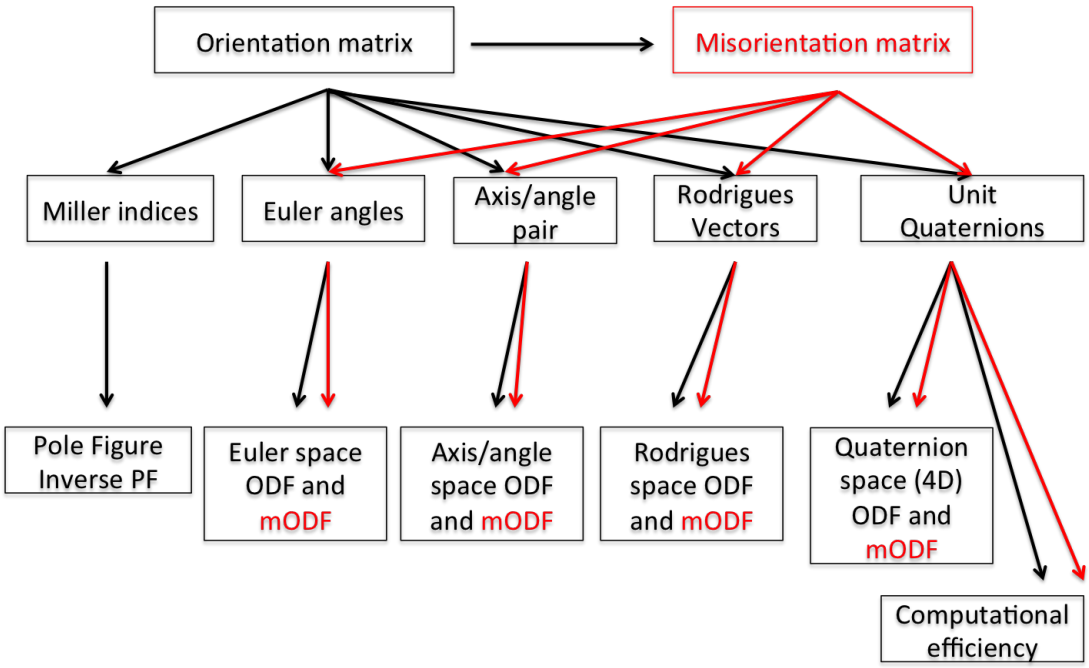

Figure 2.4: Summary of orientation and misorientation descriptors.

2.2 Mechanical Behavior of Polycrystals

In continuum mechanics, mechanical deformation of a material is defined as the transformation of a body from an initial state to a current configuration in the existence of internal or external factors, e.g., stresses and strains [25]. While physical properties are independent of any coordinate system for continuum mechanics, materials science approaches mechanical behavior as a multiscale, path dependent phenomenon. For this thesis, mechanical behavior of polycrystalline materials will be defined as the microstructural mechanisms and meso/macroscale response as seen in Fig. 2.5, affected by the microstructural features such as the grain sizes and shapes, grain interfaces, crystallographic orientation distributions, dislocation densities and internal stresses (caused by either elastic lattice strains or plastic deformation).

In metals, the physical reason for elasticity is the projection of the macroscopic elastic forces to the atomic scale as the stretching of interatomic bonds and small changes in the interatomic spacing. When forces are removed, the interatomic space goes back to the original lower energy state. Because of this atomic scale physical constituent, the magnitude of elastic modulus is a measure of the interatomic bonding forces, resistance to interatomic bonding separation. The linear elastic behavior is a function of the elastic modulus, and for ε as the strain, σ as the stress and C as

the stiffness, it is defined by Hooke's law as

$$\sigma_{ij}(x) = C_{ijkl}(x) : \varepsilon_{kl}(x). \tag{2.5}$$

As a result of Newton's law of motion, stating that in the absence of acceleration all of the forces acting on an element must balance, stress equilibrium has to be satisfied in a body, which means that the derivative of the stress should be equal to zero

$$\sigma_{ij,j}(x) = 0. \tag{2.6}$$

Plastic deformation of metals may occur due to dislocation motion (slip) or deformation twinning. For dislocation based deformation, a single slip system should be activated in a crystallographic slip plane along a crystallographic slip direction in the case of a single crystal. For polycrystal deformation through dislocation motion, defect accumulation at the boundaries between two adjacent grains may cause damage nucleation and failure. A large plastic strain is accommodated through lattice rotations that are accompanied by development of geometrically necessary dislocations (GND) [25, 26]. As previously mentioned, most polycrystalline materials exhibit het-

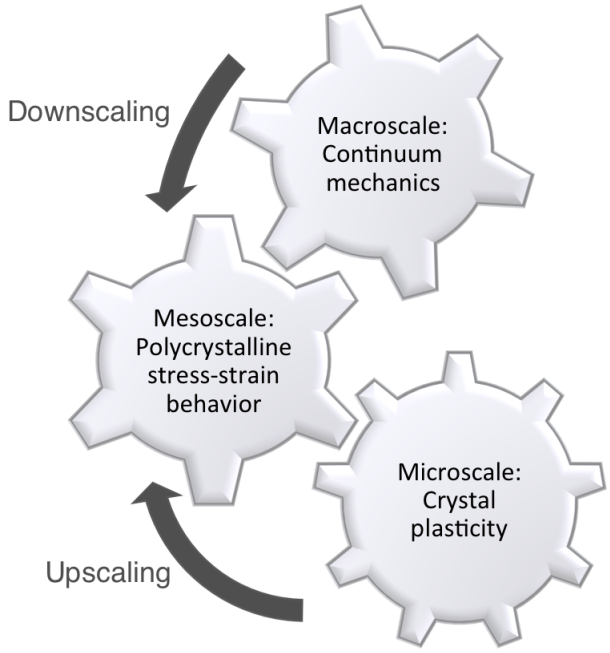

Figure 2.5: Multiscale definition of mechanical behavior.

erogeneous, directional properties due to grain level anisotropy and the crystallographic orientation distributions, and this directionality is quantified by texture. Texture directly affects the overall mechanical behavior since anisotropy gives strong vs. weak orientations, e.g., the [111] in many cubic metals is stiffer than the [100] direction [20]. Since there are many factors responsible for the anisotropic elastic or plastic deformation within a microstructure, simply examining a single crystal does not provide an accurate understanding of the anisotropic deformation process. Some of the analytical methods used in the study of mechanical behavior of polycrystalline materials are

-Voigt bound, assuming constant strains and stiffness component rule of mixture for composite materials [27].

-Reuss bound, assuming constant stresses and compliance component rule of mixture for composite materials [28].

-Self-Consistent Schemes, using Eshelby's elasticity solution for an inhomogeneity embedded in an infinite medium with composite material properties, in order to approximate the effective medium properties [29].

-Mori-Tanaka Method, using Eshelby's elasticity solution for inhomogeneity in infinite medium, relating the average macroscopic stress-strain fields to the average inhomogeneity stress-strain fields through fourth-order concentration tensors in order to approximate the effective medium properties [30].

Based on the analytical solutions, various numerical approaches through linear elasticity and crystal plasticity formulations have been developed to numerically predict macroscopic and local behaviors of polycrystals. Some of these approaches are

-Sachs model, which is based on the activation of a single slip system in each grain under homogenous stress. With this model, strain compatibility condition is satisfied, however stress equilibrium is not, providing the lower bound in predicting macroscopic behavior [31].

-Taylor and Bishop model, which is based on the simultaneous activation of multiple slip systems, satisfying the strain compatibility condition through activation of at least five slip systems via work minimization principle. Each grain is subjected to same strain, hence goes through the same shape change as the polycrystal. Being a constrained model, Taylor-Bishop provides the upper bound in predicting macroscopic behavior [32].

-Viscoplastic self-consistent (VPSC) model, which is based on the self-consistent analytical

effective medium approximation solution, where the local material response is predicted from an incompressible viscoplastic constitutive equation [26].

-Crystal Plasticity Finite Element (CPFEM) model, which can use various analytical solutions that solve an elasto-plastic deformation problem, where dislocation slip is usually considered to be the main mechanism involved in the deformation process. This model is based on both homogenization and full-field schemes, predicting the field distributions and texture evolution. Although being a mesh required, time consuming method, CPFEM is the most commonly and commercially used technique, implemented in various software packages [33].

-Fast Fourier Transform (FFT) based model, which can use various constitutive equations in various deformation regimes, as detailed at the end of this chapter. Being a mesh free, full-field image based scheme, the FFT based algorithm is shown as a numerically and computationally efficient technique [34].

2.3 Physical Metallurgy of Titanium and Its Alloys

2.3.1 Crystal structure

Titanium is an allotropic element that can exist in more than one crystallographic form depending on the chemo-thermomechanical process history and the environment temperature. This phase composition and the microscopic scale arrangement of the phase constituents are important sources of the mechanical property of titanium and in particular titanium alloys [6]. At room temperature, commercially pure titanium exists in hcp structure, which is also referred to as the alpha (α) phase. However, above 883Ê°C, which is also known as beta transus or alpha/beta transition temperature, pure titanium hcp transforms into bcc structure, also referred as the beta (β) phase [35]. Alloying with other elements can alter the room temperature crystal structure, such that aluminum and oxygen stabilizes the alpha phase by increasing the $\alpha+\beta$ transition temperature, or vanadium and molybdenum stabilizes the beta phase by decreasing the $\alpha+\beta$ transition temperature [6]. Phase stabilizing elements are summarized in Table 2.1 [6]. Other alloying elements that do not significantly affect the transus temperature are used as solid solution strengtheners [35]. Titanium and titanium alloys are generally categorized depending on their room temperature crystal structure volume fraction as α alloys, β alloys, or $\alpha+\beta$ alloys. Ti-6Al-4V, one of the focal alloys of this dissertation work, is categorized as a near alpha (above 90 % alpha fraction) $\alpha+\beta$ alloy.

Table 2.1: Phase stabilizing elements for titanium

Stabilized phase	Alloying elements
α	Al, O, La, Ga, N, C
β	V, Mo, W, Ta, Nb, Fe, Mn, Cr, Ni Si, Cu, Ag, Pb, Co

2.3.2 Microstructure in titanium alloys

Depending on the thermomechanical process and the hosted crystal structures, Ti and its alloys can have a wide variety of microstructures. While the literature varies in terminology for different grain properties and how they are produced, the rest of this thesis will follow the definitions presented in this section. α phase of Ti is generally found in either primary alpha or secondary alpha (also referred to as transformed beta) forms. Amongst these two, primary alpha shows close to equiaxed grain characteristics, whereas secondary alpha can be found in a co-oriented, lamellae morphology separated by retained beta, or in a basketweave structure, also known as Widmanstätten [6]. These structures are schematically illustrated in Fig. 2.6.

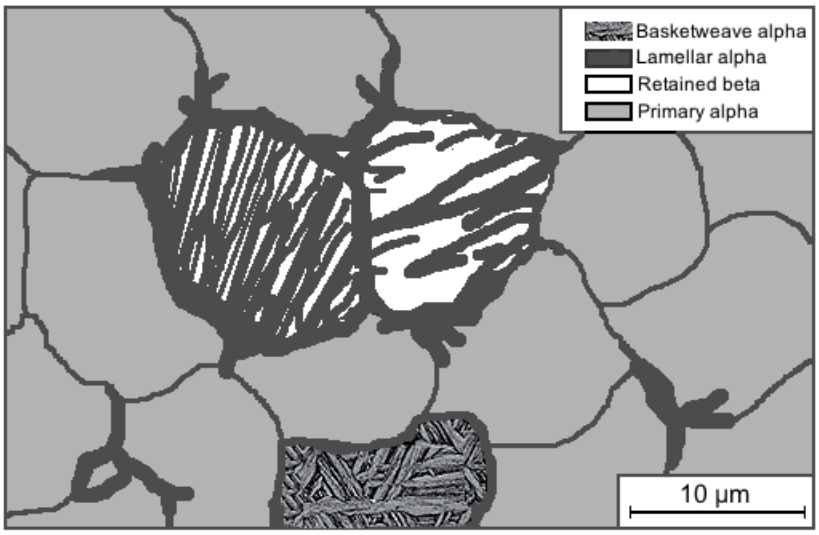

Figure 2.6: Schematic of common titanium alpha morphologies: Primary alpha and secondary alpha of lamellar and basketweave structures.

Dual phase α/β Ti alloys can potentially carry all of the morphologies illustrated in Fig. 2.6 if manufactured with the appropriate thermomechanical process. Fully lamellar, duplex, and fully

equiaxed structures with varying texture evolution have all been shown for titanium alloys as a function of the thermomechanical history [2–4], all of which influence the mechanical properties. Formation of fully lamellar α/β starts with homogenization in the β phase and finishes with aging in the α/β phase field temperature as a stress relieving treatment (or to allow solid phase transformations between any martensitic phases towards the equilibrium α/β phase mixture). Duplex structures are formed by a four step procedure, starting with homogenization in the β phase, followed by intermediate steps of deformation and recrystallization in the α/β phase, and finished with aging in the α/β phase similar to lamellar formation. Finally, fully equiaxed structures are formed in the same four step procedure as duplex formation, with the difference being the relatively lower recrystallization temperature for equiaxed grains to directly form during recyrstallization of deformed grains, and also the slow cooling rate during recrystallization where the volume fraction of primary equiaxed alpha dominates the microstructure at the expense of the lamellar alpha grains [3, 6]. Thermo-mechanical processes that form the fully lamellar, duplex and fully equiaxed structures are presented in Fig. 2.7 by replicating the data presented by Lutjering [6].

For one of the most commonly used two phase titanium alloys Ti-6Al-4V, the grain morphology, grain size, and texture that result from solidification of Ti-6Al-4V are controlled primarily by the thermal conditions that exist locally at the start of solidification, while the fine-scale microstructure is controlled primarily by the post-solidification cooling rate. Higher local temperature (800 °C) at the start of solidification is shown to result in the formation of $\alpha + \alpha'$ (both primary and secondary alpha), as compared to formation of basketweave $\alpha + \beta$ at lower local temperatures (650 °C). The alpha laths that form can share the same crystallographic orientation, also known as the same variants through rapid diffusionless martensitic transformation at high cooling rates (quenching) or through colonized regions at slow cooling rates. If the solidification rate is somewhere between martensitic transformation and colonization, the basketweave structure is observed in a multi-variant α lath form [3, 4, 6]. The fine-scale microstructure evolution for Ti-6Al-4V with is summarized in Fig. 2.8 [37, 38].

The transformation from the bcc β to hcp α phase follows certain relationship between specific crystallographic planes and directions, i.e. orientation relationships. The most commonly found orientation relation in titanium alloys is Burgers orientation relationship (BOR), where the interfaces with the lowest total energy of two phases, i.e. the close packed directions and planes overlap, giving

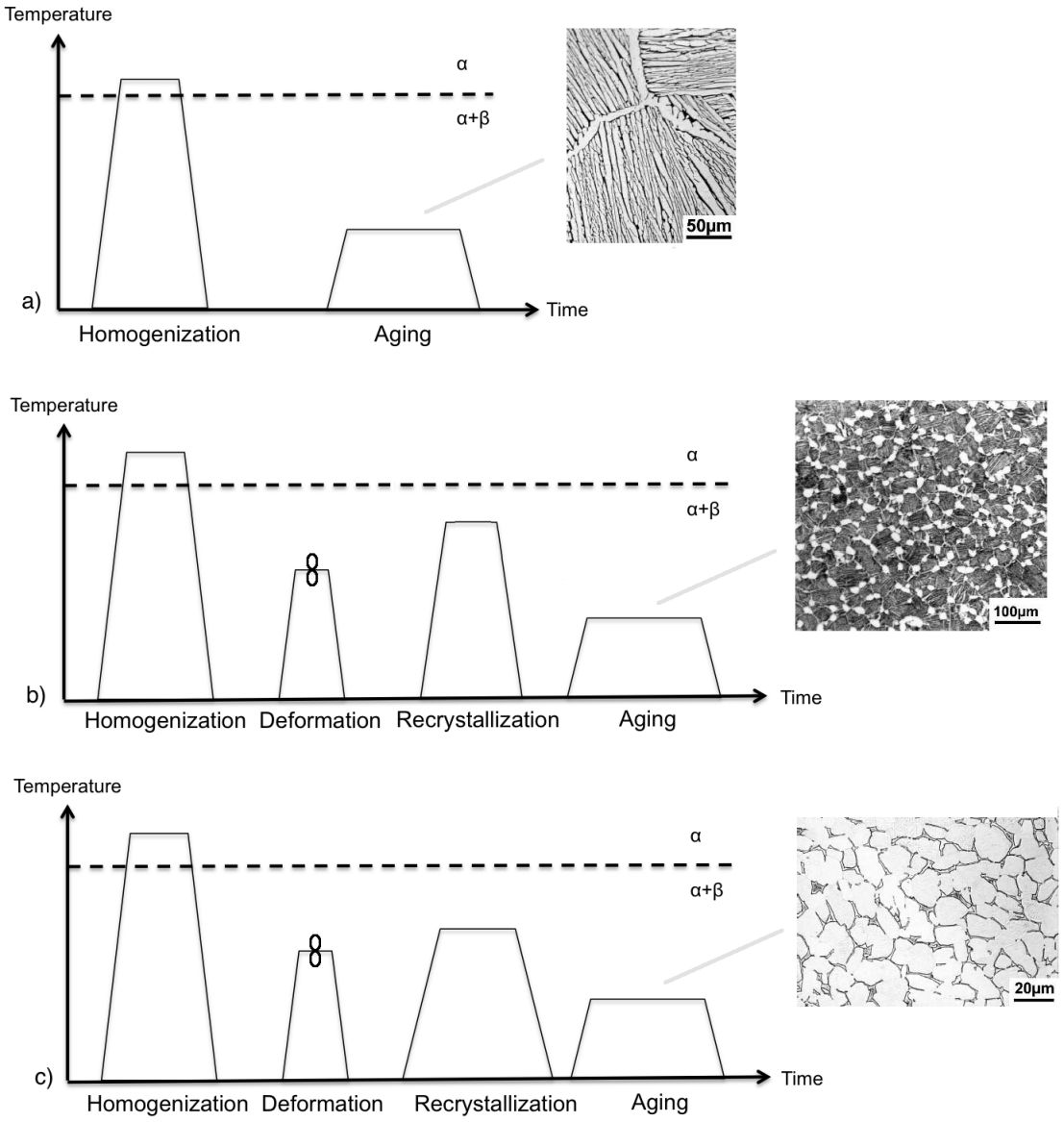

Figure 2.7: Processing routes for a) fully lamellar, b) duplex c) fully equiaxed microstructure formation for dual phase titanium alloys, replicated from [6], with example microstructures of Ti-6242 for fully lamellar and fully equiaxed, and IMI 834 for duplex [6].

the minimum crystal lattice spacing misfit [39]. Hence BOR, where the close-packed $\{011\}$ plane of the bcc lattice is parallel to the close-packed $\{0001\}$ plane of the hcp lattice, and the $< 111 >$ direction in the bcc lattice is parallel to the $< 11\bar{2}0 >$ direction in the hcp lattice, results in 12 possible variants and each habit plane/direction produces a distinct orientation [42, 43]. BOR is geometrically represented in Fig. 2.9, and the set of axis-angle pair misorientations from parent bcc to daughter hcp grains is given in Table 6.1. As a result of preferential α nucleation with specific

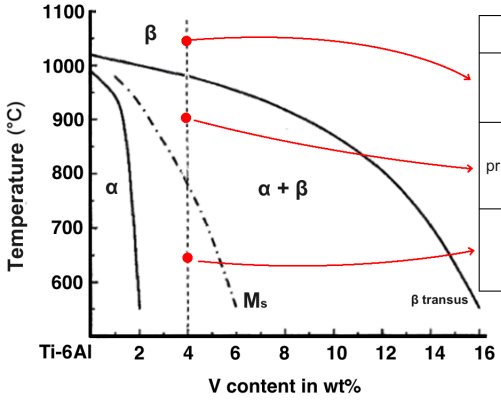

Fast Cooling	Slow Cooling
α' martensite + β	lamellar α/β + grain boundary α
primary α + α' martensite + β + grain boundary α	primary α + lamellar α/β + grain boundary α
primary α + metastable β + grain boundary α	primary α + β + grain boundary α

Figure 2.8: Pseudo-binary Ti-V phase diagram drawn at 6 % Al, illustrating the fine-scale microstructure evolution regions for Ti-6Al-4V [37, 38].

orientations that are parallel to <110 >, titanium alloys have been shown to exhibit variant selection in both martensitic and diffusional phase transformations [40, 41], which plays an important role in mechanical behavior by limiting the number of latent slip systems.

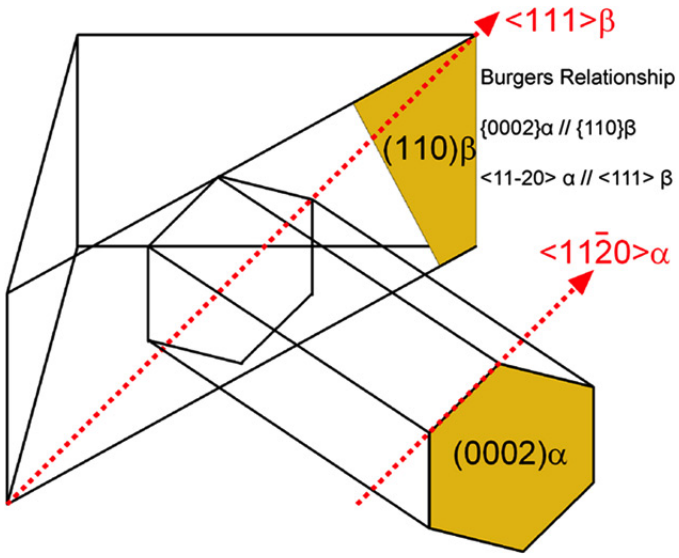

Figure 2.9: Geometric representation of BOR between the hexagonal alpha phase and cubic beta phase. Figure reproduced from Obasi et al. under creative commons license [41].

2.4 Mechanical Behavior of Titanium Alloys

Titanium and its alloys are prime candidates for high performance applications due to their high strength to weight ratio, good weldability and excellent corrosion resistance. There are multiple factors in determining titanium alloys' overall mechanical behavior, such as the alloy composition and processing technique/history, affecting the tensile properties, fatigue and creep resistance and hardness through controlling the defect content, interface characteristics, solid solution strengthening and microstructure characteristics, e.g., grain shapes and sizes. While all of these factors are important in determining a material's mechanical behavior, investigation of the individual agents is an open challenge of fundamental importance [44]. Comparing the three general classes of titanium, α alloys are shown to have medium strength, good notch toughness and good high temperature creep resistance with poor formability, the α/β alloys are shown to have medium to high strength and good formability with poor high temperature creep resistance, and β alloys are shown to have very high strength and very good formability with high density (hence weight) and low ductility [45]. It is important to note that these are the general trends, and they can be further modified with compositional, microstructural and processing manipulations.

Mechanical properties of interest for this dissertation work are tensile properties of yield and ultimate tensile strength, elongation and strain hardening behavior of dual phase α/β alloys, specifically of Ti-6Al-4V. During plastic deformation of α/β alloys, slip occurs both in the α and β phases. There are three main slip modes for the hcp phase: Basal slip with 3 systems of $\{0001\}$ $<11\bar{2}0>$, prismatic slip with 3 systems of $\{10\bar{1}0\}$ $<11\bar{2}0>$, and pyramidal <c+a> slip with 6 systems of $\{10\bar{1}1\}$ $<11\bar{2}0>$. For bcc phase, three main modes of $\{110\} < 111 >$ with 12 systems, $\{112\} < 111 >$ with 12 systems, and $\{123\} < 111 >$ with 24 systems are observed. In the literature, different relative ratios and activation barriers are reported for different modes. For instance, the lack of consensus on the relative critical resolved shear stress (CRSS) values of Ti-6Al-4V is observed by looking at studies of Dunst and Mecking, reporting bcc:basal:prism:pyramidal<c+a> ratio of 0.33:1:0.67:2 [46], of Lebensohn and Canova reporting bcc:basal:prism:pyramidal<c+a> ratio of 0.25:1:1:8 [47], and of Bieler and Semiatin, reporting basal:prism:pyramidal<c+a> ratio of 1:0.7:2 [48]. For dual phase titanium alloys, the majority of the room temperature plastic deformation is accommodated by the α phase as it is found to be the harder phase, seen from the above

CRSS ratios of both bcc:basal of 0.25:1, and 0.33:1. While the texture evolution is not noticeably affected by slip in the β phase [46], the microstructural characteristics of the β phase, such as the crystallographic orientation, can be important factors affecting the deformation behavior.

Being the focus of this dissertation work, understanding the variation of the titanium alloys' mechanical properties in relation to the microstructure has been an ongoing effort for many years. Microstructural factors that are shown to affect the mechanical properties can be summarized as α colony size, prior β grain size, thickness of grain boundary and lamellar α, texture of phases and volume fractions of α, β and martensitic α phases [2, 8, 9, 11, 13]. For dual phase alloys, most important factor in relation to mechanical behavior is found as the colony size as it determines the slip length, hence the onset of plastic deformation through a Hall-Petch type relation [49, 50], where the increase in α colony size decreases the yield strength [2]. Similarly, for fine lath lamellar structures and basketweave structures, decreased slip length has been shown to increase the yield stress while decreasing the ductility [2]. On the other hand, Lutjering reported inverse Hall-Petch type relation for the prior β grain size with a theory that proposes the length of the β size as grain boundary α slip length limiting factor, causing reduced stress concentrations for small β grain sizes, higher ductility and lower tensile strength [2]. Furthermore, texture of the high temperature β phase has been shown to significantly affect the inherited selection of low temperature α texture, which in turn determines the orientation of the hcp basal plane with respect to the loading direction and the yield stress (YS), ultimate tensile stress (UTS) and strain hardening behavior [51]. In addition to all of the intrinsic factors, for titanium is a rate and temperature sensitive material, testing conditions tremendously affect the measured mechanical properties. Gupta et al. investigated the evolution of strain hardening exponent, n, with both heat treatment and cold working conditions and found that n decreases with increased strain rate in the case of heat treatment, and increases with strain rate in the case of cold working due to rearrangement of the generated dislocations [52]. Chen et al. studied the change in work hardening over a wide range of strain rates (10^{-4} - 10^{4} s^{-1}) and temperatures (20-900 °C), discovering that increased temperature decreases work hardening, and more so with high strain rates [53]. Some of the studies showing the effects of strain rate [53], temperature [54] and the basal plane orientation with respect to loading direction [51] on the UTS, YS and strain hardening behavior of Ti-6Al-4V are summarized in Fig. 2.10 by recompiling the figures from the referenced sources.

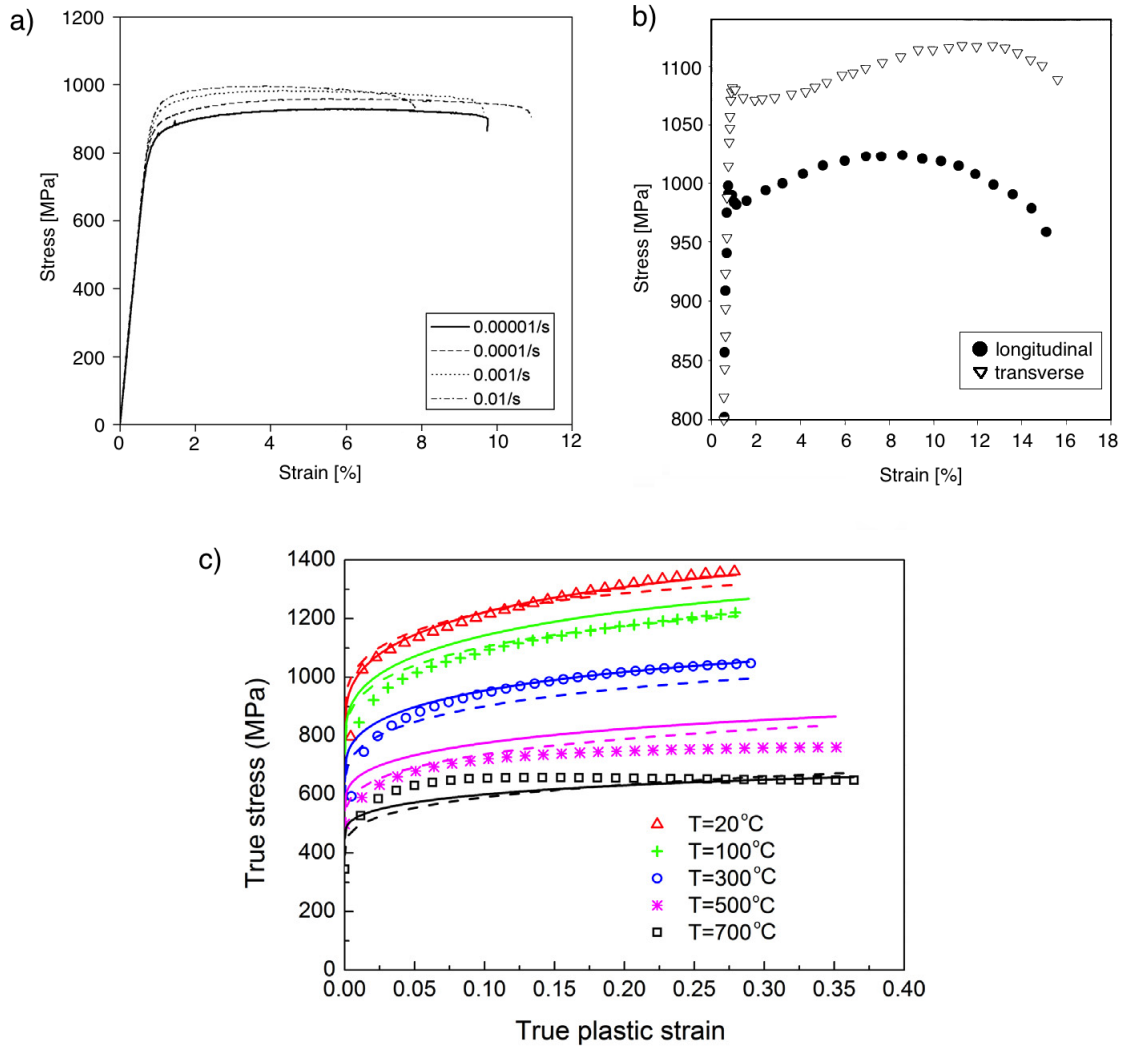

Figure 2.10: Ti-6Al-4V stress-strain behavior in relation to a) Strain-rate dependence [54], b) Basal plane orientation with respect to loading direction dependence [51], c) Temperature dependence, also showing constitutive modeling fits with dashed and full lines on top of experimental data represented with symbols [53].

For hcp phase, low crystal symmetry limits the number of active slip systems at room temperature. Because of this, additional deformation modes of twinning can be activated during deformation, however in this work twinning will not be focused on as it is not a very commonly observed room temperature deformation mode for Ti-6Al-4V alloy [44].

2.4.1 Previous efforts to model the mechanical behavior of Ti-6Al-4V

Because engineering alloys are complex, and they constitute multiple (potentially interdependent or competing) variables that determine the desired properties, it is difficult to characterize every aspect

and quantitatively analyze the relative contribution of each feature. In the last few decades, Integrated Computational Materials Engineering (ICME) approach has been utilized extensively for development of both statistical and microstructure based models that quantitatively and computationally describe the interrelationships between processing, microstructure, properties, and performance of titanium alloys [9, 46, 55–58, 60–63]. Statistical models for predicting the mechanical behavior of Ti-6Al-4V can be summarized in the categories of either top-to-bottom where numerical formulations are developed, constitutive equations are determined and then compared to experimental data for validation and modification, or bottom-to-top where the experimental data is used to inform and train neural network approaches that in turn predict the mechanical behavior statistically. As a top-to-bottom approach, Dunst and Mecking investigated the VPSC model for deformation texture prediction of an equiaxed alpha-beta titanium, and showed that using fit hardening parameters results in good agreement with experiments [46]. Similarly, Lopez et al. used the same VPSC model and integrated it with a new finite element algorithm for computational efficiency in predicting the mechanical behavior and texture development of Ti-6Al-4V, and compared their strain-rate and temperature sensitive model results to experimental data showing excellent agreement [55]. Collins et al. presented a novel constitutive equation for capturing the effects of microstructural features, such as phase fraction, grain size and grain morphology, to predict the yield strength of Ti-6Al-4V, showing the constitutive model prediction and the experimental yield strength data fall within two standard deviations [56]. As a bottom-to-top approach, Tiley used experimental data to train a fuzzy logic neural network model, which in turn could accurately predicted the room temperature elongation, ultimate tensile and yield stress values within 3 % error [9]. Shi et al. used an extensive microstructural characterization data collected from Ti-6Al-4V samples with different lamellar features as input in a back propagation artificial neural network model, and predicted the tensile properties within 6 % error [58]. While statistical models can predict the macroscopic properties, microstructure based models are used to model the local deformation and texture evolutions. Using CPFEM, Barton and Dawson demonstrated the importance of including local neighborhood in the simulation of dual phase titanium alloys by showing that the beta phase is the shear strain carrier, which further increases in magnitude with increased alpha volume fraction. They also showed increased intra-granular heterogeneity of the deformation with increase in alpha fraction [59]. However they had to limit the size of simulation aggregate, hence the number of grain interactions due

to computational expense of meshing and CPFEM. The problem of computational expense limiting the simulation domain size is observed in other studies of dual-phase titanium alloys as well, e.g., a beta processed titanium where the lamellar structure is homogenized for simulation efficiency [60]; a case in which the alpha/beta structure is assumed to be a colony grain structure with random orientation assignment [61]; a microstructure in which grains are assumed to be cubes, and the lamellar duplex structure is homogenized for meshing efficiency [62]; and, a case in which the bimodal primary alpha+lamellar colony characteristics are represented through size distributions [63]. Although these studies are shown to be statistically representative in various ways, they sidestepped the purpose of performing microstructure based micromechanical modeling by not including the lamellar morphology, individual α laths, or Widmanstätten characteristics in exchange for computational expense because a two-phase lamellar structure requires a large element count and correspondingly large number of degrees of freedom. The micromechanical modeling work presented in this dissertation overcomes this issue by using a meshless, FFT-based full field micromechanical model, which can compute full field solutions directly on image of microstructures with $>$ 100 prior β grains and $>$ 50000 α laths.

2.5 Process - Structure - Property of Additively Manufactured Titanium

2.5.1 Process - Additive manufacturing

Additive manufacturing (AM), or 3D printing, is a layer by layer fabrication technique where fully dense 3D parts can be built into complex shapes based on their computer aided design (CAD) models [64]. Owing to the advantages it provides, in the last few decades 3D printing has been adopted by biomedical, automotive, electronics and aerospace industries for a wide variety of materials, such as plastics, metals, ceramics and composites. Amongst the AM advantages are the flexibility in design, reduced material waste, reduced tool cost, and fewer post-process steps due to the ability of printing near-net shape geometries [1,64]. Continuing development of the green initiatives and control systems is widening the interest in AM technology. For instance, flexibility in design is shown to reduce the weight of airplanes significantly if the non-critical aircraft components such as buckles, brackets, hinges and cabin furnishings were to be additively manufactured in lighter-weight complex shapes, predictibally resulting in a 6.4 % reduction of fuel consumption for aircrafts if the

AM design flexibility is used to its full potential [65]. There are various different types of metal AM, which can be categorized in terms of the energy source, material feedstock, process type, build volume etc. One of the most common ways of AM categorization is based on the material feedstock as powder-bed, powder-feed and wire-feed systems [1]. Within these three categories, the metal stock can be locally melted via an electron beam, a laser beam, or arc based welding.

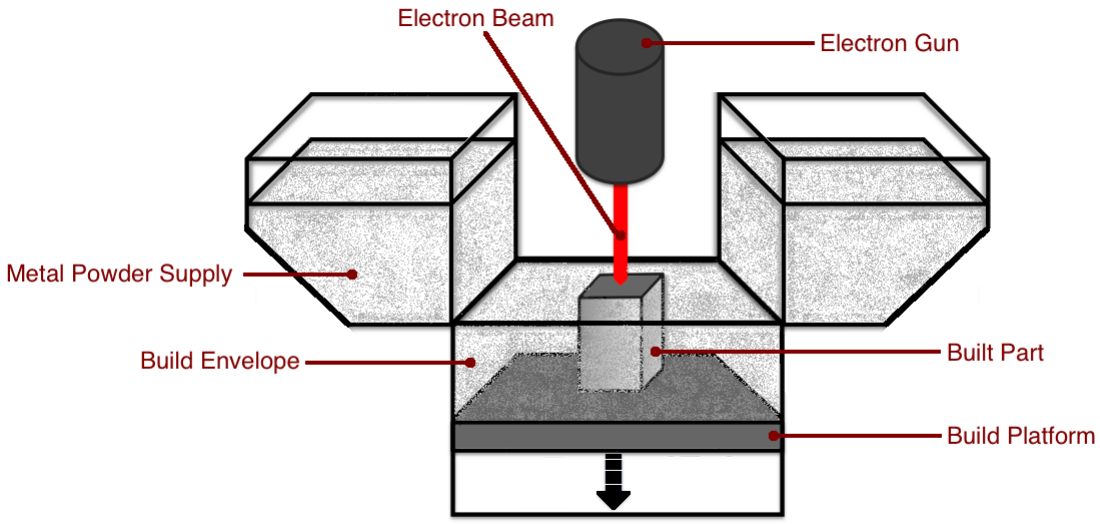

Figure 2.11: Schematic of a powder bed EBM process.

This thesis work focuses on powder-bed based EBM AM of metallic components, in which successive layers of material powder are deposited onto a substrate plate and a powder reservoir via electron power source, Fig. 2.11. Currently the Sweden based company ARCAM (recently acquired by General Electric) is the sole commercial provider of the powder-bed based EBM machines [66]. Similar to other AM processes, EBM builds components layer by layer, starting from the CAD data. Different than selective laser melting which is applicable to a wide range of materials such as ceramics, polymers and metals, EBM can only work with metallic material systems as electrical conductivity is required for the electron beam to function. On the other hand, some advantages of the EBM process are the vacuum condition of the build chamber, high environment temperature and the pre-heated substrate plate, which allow to operate the beam at high speeds and high power, making EBM preferable for high performance structural alloys [66]. While there are advantages to powder bed based EBM AM, choosing the appropriate processing parameters (beam power, beam velocity,

pre-heating temperature, build geometry, scanning length and how the build is laid out on the plate) requires operator expertise and delicate consideration of the final product requirements as processing conditions directly determine the part density, composition, microstructure and properties. Some of the processing effects on the AM titanium microstructure and mechanical behavior is discussed in the following section.

2.5.2 Structure and property - Mechanical behavior and microstructure of AM Ti-6Al-4V

Mechanical behavior

Depending on the processing history, titanium alloys can have a highly heterogeneous and complex microstructure, some of which are exampled in section 2.3. Unfortunately, for additively manufactured Ti-6Al-4V the complexity is far from being solely the microstructural characteristics. One of the process dependent features of AM is the porosity defects, which is intrinsic to the technique. It is an important phenomenon that needs attention as the pores transferred to the end part can act as failure initiation sites and be detrimental for fatigue life [1, 67]. Three different types of porosity that are reported from AM parts are lack of fusion, keyhole and trapped gas porosity. While the trapped gas porosity is hypothesized to transfer from the powder itself [68], lack of fusion is caused by incomplete melting, and it is seen if the beam energy is insufficient or beam speed is to high to melt all the powder [69], and keyhole porosity is caused by rapid solidification at high power or low beam speed conditions [70]. Therefore, both the density of the unmelted powder and the processing parameters play a key role in the determining the volumetric porosity content of the AM part, hence the dynamic range mechanical properties. Despite the existence of pores causing a shorter fatigue life and lower fracture toughness, tensile properties of additively fabricated Ti-6Al-4V are shown to compete, and sometimes exceed the conventionally manufactured materials [71]. However, AM being a pseudo-stable and individualistic process where each machine has the potential to produce different results, the literature on the tensile properties can be deceiving if not surveyed cautiously. For instance, Faccini et al. documented the yield strength of Arcam as-built Ti-6Al-4V as 830 ± 5 MPa [72], almost 30 % different than McLouth et al's 1135 ± 12 MPa [73]. Neither of these studies mentioned the tensile direction in relation to build height, process parameters or the build geometry, which are all hypothesized to affect the end part microstructure, hence the mechanical behavior.

Table 2.2: Reported tensile properties of wrought and various Arcam machine processed Ti-6Al-4V

Process	Specimen Orientation	Yield Strength [MPa]	Ultimate Tensile Strength [MPa]	Elongation [%]	Reference
Arcam A1	Vertical	812 ± 12	851 ± 19	3.6 ± 0.9	[74]
Machine	Horizontal	783 ± 15	833 ± 22	2.7 ± 0.4	
Arcam	Vertical	879 ± 12.5	953 ± 8.8	13.8 ± 0.9	[75]
Machine	Horizontal	870 ± 8.1	959 ± 8.3	12.1 ± 0.9	
Arcam S12	Vertical	984 ± 8.5	1032 ± 12.9	9 ± 2.9	[76]
Machine	Horizontal	982 ± 5.7	1029 ± 227	12.2 ± 0.8	
Arcam S400	Vertical	782 ± 5.1	842 ± 13.84	9.9 ± 1.02	[77]
Machine	Horizontal	844 ± 21.6	917 ± 30.53	8.8 ± 1.42	
Wrought	Vertical	948	994	21	[78]
	Horizontal	962	1008	19	

For powder bed based EBM, machine type (different releases of Arcam machines) and specimen orientation (vertical or longitudinal being parallel to build direction and horizontal or transverse being perpendicular to build direction) appears to affect the tensile properties, Table 2.2. Of the studies summarized in Seifi and Lewandowski's AM review, 3/4 reports horizontal builds to have slightly higher yield and tensile strengths and lower elongation [79]. Although properties are sensitive to machine, variations have also been reported on samples fabricated within the same type of machine. As a reference, a subset of the reported tensile properties is presented in Table 2.2, along with an example wrought Ti-6Al-4V measurement. Granting the tensile properties are extensively being studied for different machines, post-process conditions and specimen orientations, one aspect that is found to be lacking in the AM Ti-6Al-4V mechanical behavior literature is the strain hardening behavior, e.g., lack of reports on full stress-strain curves. The results are generally reduced to yield, ultimate tensile and elongation values, or a representative stress-strain curve is reported for all of the samples, which does not tell much about the hardening behavior. For mechanical modeling, using material appropriate hardening parameters are essential in capturing the behavior, and for this reason as a new addition to the literature this thesis work demonstrates the full stress-strain curves of all the performed tests and the individually extracted Voce hardening parameters.

Microstructure

When a thermally gradient manufacturing process such as AM is utilized to build parts, the resulting part unavoidably exhibits spatial heterogeneity in microstructural characteristics. For the EBM

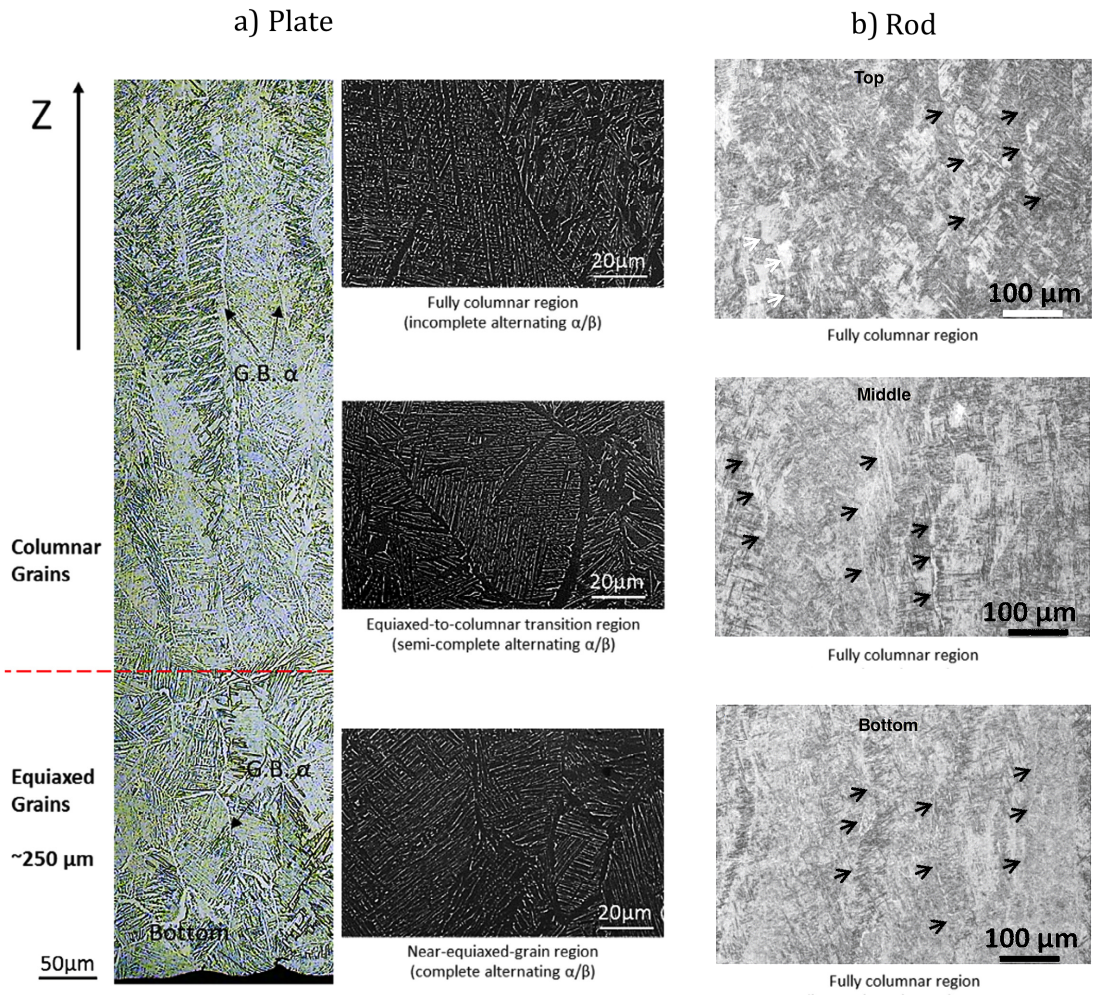

Figure 2.12: Comparison of long rod vs. tall plate microstructures of EBM AM Ti-6Al-4V, a) OM micrographs showing equiaxed prior beta morphology at the bottom of the build with coarsening beta width and rod interspacing with build height [84], b) OM micrographs showing fully columnar microstructure throughout the build, without the existence of an equiaxed beta region [83].

process, using a preheated powder bed is claimed to reduce this heterogeneity by lowering the cooling rate during and after the AM process, and by forming an equilibrium $\alpha+\beta$ structure through decomposing the martensitic phase [80] to different extents depending on the subsequent thermal cycling history [81]. In general, AM Ti-6Al-4V microstructures are shown to be to either beta-quenched, or quenched and tempered like. Typically a fine lamellar α structure is observed in basketweave morphology, separated by low fraction of retained β that enhances ductility. The component size and the location of the parts on the build plate in relation to bulkier components is shown to affect the observed characteristics as well due temperature rises through thermal radiation, e.g., smaller parts exhibiting higher martensitic alpha fraction when built isolated as opposed to

built near a larger part [76, 80, 82]. Apart from the thermal radiation, the thermal cycling of long term annealing due preheated build plate and elevated build temperature, rapid solidification, and high cooling rate of the solidified region repeats layer by layer during the entire EBM process. Heat sink throughout the build and the temperature spikes of the precursor layers beyond the in-process one is hypothesized to cause a graded microstructure, of which the degree of gradient would change as a function of the process history and the build geometry. For instance, Murr at al. reported significant transitions along the height, with average thickness of 3.2 μm acicular alpha platelet at the top 1 cm vs. average thickness of 1.6 μm shorter, more lamellar like alpha platelet at the bottom 1 cm observed within two 40 mm tall EBM-built cylindrical Ti-6Al-4V samples [111]. The combined build geometry+temperature gradient along the build height influence on microstructure can be seen from the images replicated from Lu et al.'s work on the graded microstructure along the build height of long Ti-6Al-4V rods [83] vs. Tan et al.'s work on tall Ti-6Al-4V plates [84] in Figure 2.12, where Tan et al. reports equiaxed beta morphology at the bottom of the build with observed beta width and beta rod interspacing coarsening with build height, whereas Lu et al. shows fully columnar beta throughout the build height.

One of the reasons of the varied cooling rate and peak temperature is the repeated laying down of weld tracks along the build height as the part is being printed layer by layer. The repeated melting/remelting and laid down melt pools lead to dendritic growth down the temperature gradient, which turns out to be the build direction for AM, causing columnar shaped prior beta structure [80, 82]. Furthermore, for Ti-6Al-4V this high temperature columnar cubic beta phase solidifies crystallographically in <100> direction, developing a <100> fiber texture [82]. The columnar and crystallographic orientation nature of a typical AM Ti-6Al-4V is shown in Fig. 2.13, by reconstructing the prior beta phase (Fig. 2.13.a) from the alpha orientation map (Fig. 2.13.b) using a back construction algorithm. This EBSD map of bulk AM Ti-6Al-4V was collected by Ross Cunningham, and Lionel Germain from Metz reconstructed the beta map using software Merengue 2 [85]. Burger's orientation relationship is assumed between two phases, which is qualitatively seen by comparing the <0001> pole figure of the alpha phase with the <011> pole figure of the beta phase. A slight deviation from the expected <100> beta texture is observed.

In summary, depending on the location, build geometry, process history and even the model of EBM machine, a Ti-6Al-4V microstructure can change from martensitic or fine acicular alpha'

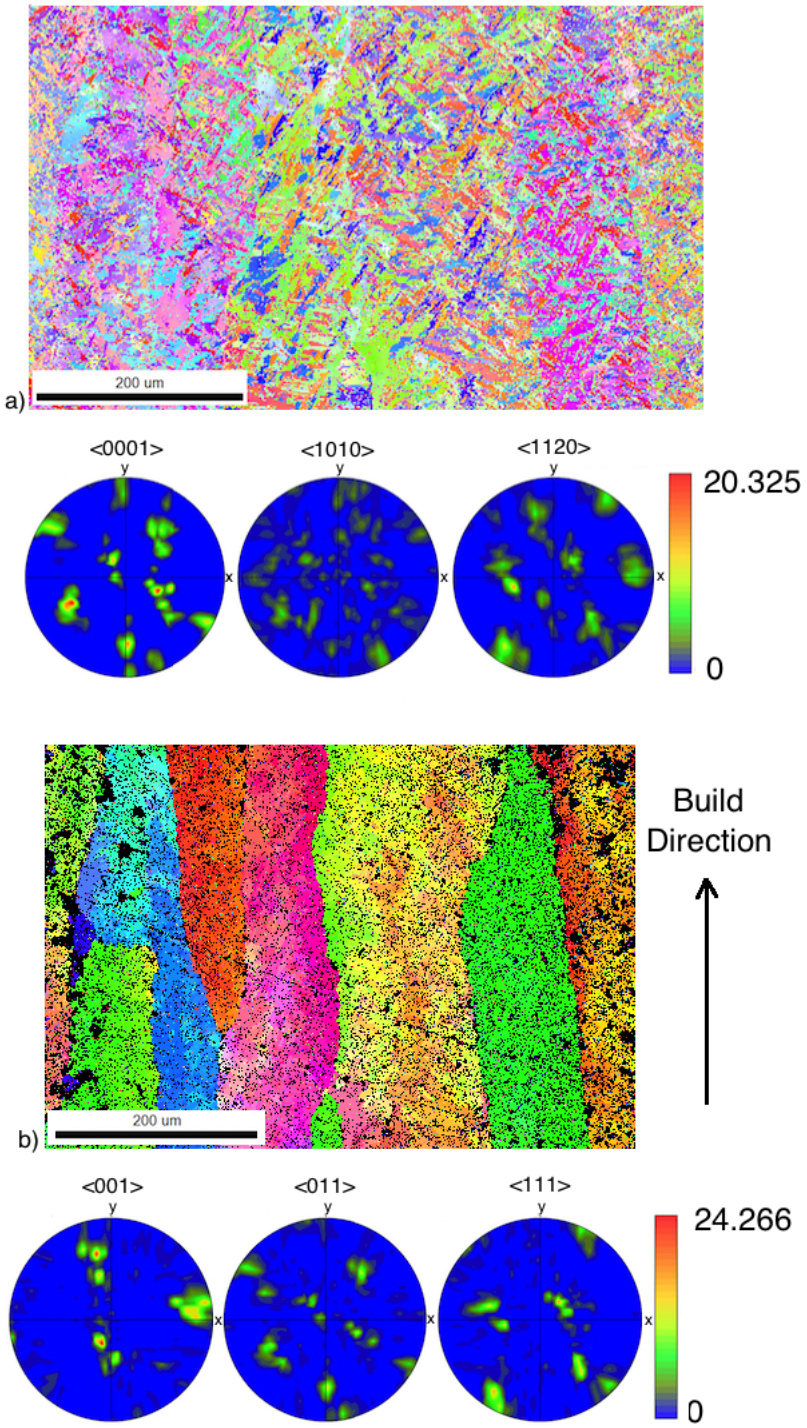

Figure 2.13: A typical EBM Ti-6Al-4V bulk microstructure a) EBSD map of alpha phase and corresponding hcp pole figures, b) Reconstructed beta phase and corresponding bcc pole figures. Coloring of the orientation maps is based on IPF colors

structure at the high cooling rate into fine alpha+beta lamellae, basketweave, or a mixture of colonized lamellar alpha and coarse acicular alpha' phases at the slower cooling rates, and any possibility

of microstructural arrangement effects the resulting mechanical behavior. Furthermore, the processing conditions can be changed to find power-velocity combinations that can manipulate the prior β shape, size and orientation [86, 87], and because the experimental measurement of every combination is not possible, incorporating computational methods into AM research becomes an urgent necessity for investigating structure-property relationships.

CHAPTER III

Experimental and Computational Methods

This chapter presents detailed discussion on two of the extensively utilized techniques for this dissertation work: Micromechanical modeling - the Fast Fourier Transform (FFT) based method, and microstructure characterization - the High Energy X-Ray Diffraction Microscopy (HEDM) method.

3.1 FFT-based Spectral Micromechanical Modeling

Starting with the works of Sachs and Taylor [31,32], mechanical behavior models evolved over time. The Sachs model (or the lower-bound model) assumes a homogeneous stress field in which all grains experience same stress tensor, and compatibility is violated at grain boundaries, whereas Taylor (or the upper-bound model) assumes uniform strain in the microstructure in which all grains undergo same strain tensor, and stress equilibrium is failed at grain boundaries. Neither of these methods takes account of the interactions inside the microstructure, so a more accurate method called self-consistent (SC) modeling was developed. Based on the analysis of Eshelby [88], the SC approach treats each ellipsoidal shaped grain as an inclusion that is embedded inside a homogeneous reference medium (the microstructure domain), and then strain is calculated as an average field within each grain [89,90]. Molinari showed that the deformed texture prediction is in good agreement with known experimental results [89]. Since self-consistent formulation is a mean field method, conventionally, small-scale finite element techniques are used to simulate the local mechanical response of complex microstructures. Clearly, the finite element method requires meshing, which results in a system with a large number of degrees of freedom. One alternative to the finite element method (FEM) is the Fast Fourier Transform (FFT) based formulation, introduced by Moulinec and Suquet as a tool for full-field simulation of mechanical response of polycrystalline materials. In general,

the FFT algorithm computes the stress and strain fields at each point on a grid based on the crystallographic orientation (and associated anisotropy) of the point when the microstructure is subjected to macroscopic loading [91]. It uses a microstructural image with orientation information as direct input, and requires periodic unit cells and boundary conditions. Since the method does not require meshing, the calculation is computationally efficient and is able to manage a large number of degrees of freedom typically involved in the description of complex microstructures [33, 91]. Prakash and Lebensohn compared FFT with FEM and demonstrated that the FFT computations scale as NlogN (N is the number of grid points), whereas FEM typically scales as N^2, which means it is computationally more expensive for large problems [33]. Lebensohn showed that for linear systems, FFT results provide similar accuracy as the SC approximation, with the additional advantage of giving local field values [92] i.e., it can resolve intragranular gradients. Multi-phase behavior is captured through defining the model properties for each phase individually, and calculating the n-site grain interactions both within one phase and between all phases. Elastic, viscoplastic and elasto-viscoplastic deformation regimes are all formulated in the algorithm [34,93], and are detailed in the following sections.

Elastic formulation

Assuming periodic boundary conditions across the elastically heterogeneous representative volume element (RVE), which is subjected to an average strain **E**, a reference medium is prepared by defining an initial homogeneous reference stiffness tensor $C^0_{ijkl} = \frac{1}{N}\sum C_{ijkl}(x)$. Taking ε(x) as the local strain, σ(x) as the local stress and C(x) as the local stiffness, the local problem can be written in terms of the constitutive equation (Hooke's law) and the equilibrium condition across the boundary of two adjacent grains.

$$\begin{aligned} \sigma_{ij}(x) = C_{ijkl}(x) : \varepsilon_{kl}(x) \ in\ RVE \\ \sigma_{ij,j}(x) = 0 \ in\ RVE \end{aligned} \tag{3.1}$$

For small strain compatibility condition $\varepsilon_{kl}(x) = \frac{(u_{k,l}(x)+u_{l,k}(x))}{2}$, where u is the displacement gradient, and the local fluctuations in stress $\tau_{ij} = (C_{ijkl} - C^0_{ijkl}) : \varepsilon(x)$, the problem becomes

$$\sigma_{ij}(x) = C^0_{ijkl}\, u_{k,l}(x) + \tau_{ij}(x) \tag{3.2}$$

where τ_{ij} is the local deviation from the average stress field that can be calculated iteratively using the fluctuation in stiffness and local strain. Combining equation (3.2), and the equilibrium condition $\sigma_{ij,j} = 0$ gives

$$\tau_{ij,j}(x) + C^0_{ijkl}\, u_{k,lj}(x) = 0. \tag{3.3}$$

In real space, $\tau_{ij,j}(x)$ can be thought as a fictitious body force. In order to solve equation (3.3) by Green's method, defining G as

$$\hat{G}_{ik} = [C^0_{ijkl}\, \omega_l\, \omega_j]^{-1} = \hat{A}^{-1}_{ik} \tag{3.4}$$

where ω is frequency in Fourier space and $\hat{A}^{-1}\hat{A} = I$. Taking the Fourier transform of equation (3.3) results in

$$F\left[\sum_{lj} C^0_{ijkl}\, \frac{\partial u_k}{\partial x_l\, \partial x_j}\right] = -F(\tau_{ij,j}(x)). \tag{3.5}$$

The polarization field $\tau_{ij,j}$, and the strain field $\varepsilon_{ij}(x)$ in Fourier space [94] can be written as

$$\begin{aligned} F(\tau_{ij,j}(x)) = \sum_j i\,\omega_j\,\hat{\phi}_{ij} = i\sum_j \hat{\phi}_{ij}\,(\omega)\,\omega_j \\ F(\varepsilon_{ij}(x)) = i\,u_i(\omega)\,\omega_j. \end{aligned} \tag{3.6}$$

For $\hat{\Gamma}^0_{ijkl} = -\hat{G}_{ik}\,\omega_l\,\omega_j$ (symmetrization), equations (3.4), (3.5) and (3.6) give

$$\hat{\bar{\varepsilon}}_{ij}(\omega) = \hat{\Gamma}^0_{ijkl}\,\hat{\tau}_{ij}(\omega). \tag{3.7}$$

Inverse Fourier transformation converts the perturbation field τ_{ij} into real space, which is replaced in equation (3.2) to calculate the stress field.

Algorithm for elastic FFT

The algorithm is initialized with $\hat{\bar{\varepsilon}}(x) = 0$ and $\sigma^0(x) = C^0 : \mathbf{E}$, and then the local stress-strain fluctuations are calculated iteratively [34].

a. Macroscopic average strain, determined from the boundary conditions is initialized as the elastic strain at each grid point.

b. Local stress at each grid point is calculated from the strain using Hooke's law.

c. Polarization field is calculated through Green's method and Fourier transform.

d. Stress equilibrium and convergence is tested.

e. New stress-strain fields are updated.

f. Steps b-e are repeated until convergence.

Viscoplastic Formulation

Following Molinari [89], the stress tensor is decomposed into deviatoric stress and hydrostatic pressure components as

$$\sigma_{ij} = \sigma'_{ij} - p\delta_{ij} \tag{3.8}$$

where σ' is the deviatoric and p is the hydrostatic pressure components. Thus, equilibrium and incompressibility conditions become

$$\begin{aligned} \sigma_{ij,j} = \tilde{\sigma}_{ij,j} = \sigma^{'}_{ij,j} + p_{,i} = 0 \\ v_{k,k} = 0 \end{aligned} \tag{3.9}$$

where v is velocity.

In the plastic regime, either the secant or tangent approach can be used to calculate the stiffness. In this formulation, tangent approach is chosen where $E_{tan} = \frac{d\sigma}{d\varepsilon}$.

The local constitutive equation then becomes

$$\sigma'(x) = M^{tg^{-1}}(x) : d(x) + S^o(x) \tag{3.10}$$

where M^{tg}(x) is the local tangent compliance (thus $M^{tg^{-1}}$ is tangent stiffness, and will be denoted as L^{tg}), d(x) is local strain rate, and S^o is the back-extrapolated stress term coming from Taylor expansion at a fixed point.

Since the relationship between stress and strain is not linear in plastic region, stiffness cannot be simply averaged as in the elastic solution to find the reference medium value. The homogenous reference medium is described in terms of a tangent behavior as

$$\Sigma'(x) = L^{tg}_o D + S^{oo} \tag{3.11}$$

where L_o^{tg} *and* S^{oo} are respectively the stiffness and back-extrapolated stress of the medium.

In the viscoplastic FFT algorithm, the Taylor model is used at each point. For $\vec{n}$ is the slip plane normal, $\vec{b}$ is the slip direction, $R = \begin{pmatrix} b_1 & n_1 & x_1 \\ b_2 & n_2 & x_2 \\ b_3 & n_3 & x_3 \end{pmatrix}$ is the transformation matrix from slip system axes to crystal axes, $m_{ij} = \frac{1}{2}(b_i n_j + b_j n_i)$ is the Schmid tensor, and $\varepsilon_{ij}^{slip} = \begin{pmatrix} 0 & \frac{\gamma}{2} & 0 \\ \frac{\gamma}{2} & 0 & 0 \\ 0 & 0 & 0 \end{pmatrix}$ is the strain tensor in slip level, transformation of a shear γ from slip system to crystal axes can be written as

$$\begin{aligned} \varepsilon_{ij}^{crystal} &= R_{1i} R_{2j} \varepsilon_{12}^{slip} + R_{2i} R_{1j} \varepsilon_{21}^{slip} \\ \varepsilon_{ij}^{crystal} &= \frac{1}{2}(b_i n_j + b_j n_i)\gamma = m_{ij}\gamma \end{aligned} \tag{3.12}$$

and the resolved shear stress on slip plane and slip direction is given by

$$\begin{aligned} \tau = \sigma_{12}^{slip} &= R_{1i} R_{2j} \sigma_{ij}^{crystal} \\ \tau = b_i n_j \sigma_{ij}^{crystal} &= m_{ij} \sigma_{ij}^{crystal} . \end{aligned} \tag{3.13}$$

Because slip plane normal and slip direction are perpendicular to each other, $\vec{n} \perp \vec{b}$, trace of the Schmid tensor is zero, tr(m) = $b_k n_k$ = 0. Thus, trace of crystal system strain tensor is also zero as tr(ε) = tr(m)=0, i.e. the crystal system strain tensor should be traceless as a result of incompressibility. Superimposition of shear over the slip systems gives total strain rate of the grid point as

$$\dot{\varepsilon}_{ij} = \sum_{s}^{N} m_{ij}^{s} \dot{\gamma}^{s} . \tag{3.14}$$

Both Lebensohn [34] and Tomé [26] describe the local incompressible viscoplastic constitutive behavior by means of the rate-sensitive approach,

$$\dot{\gamma}^{s} = \dot{\gamma}_o \left(\frac{\tau^s}{\tau_o^s} \right)^n = \dot{\gamma}_o \left(\frac{m_{kl}^s \sigma_{kl}}{\tau_o^s} \right)^n . \tag{3.15}$$

Substituting $\dot{\gamma}^s$ into equation (3.15) gives the non-linear constitutive equation as

$$\dot{\varepsilon_{ij}} = \dot{\gamma_o} \sum_s m^s_{ij} \left(\frac{m^s_{kl}\, \sigma_{kl}}{\tau^s_o} \right)^n . \tag{3.16}$$

Note that the tangent stiffness is the derivative of stress with respect to strain. Thus, local compliance $M^{tg}(x)$ denoted in the constitutive equation (3.10), summed over all potentially active slip systems becomes

$$M^{tg}(x) = n\dot{\gamma}_0 \sum_s \frac{m^s(x) \bigotimes m^s(x)}{\tau^s_0(x)} \left(\frac{m^s(x) : \sigma'(x)}{\tau^s_0(x)} \right)^{(n-1)} \tag{3.17}$$

where $\tau^s_0(x)$ is the critical resolved shear stress, $\dot{\gamma}_0$ is the normalization factor and n is the reciprocal of the rate sensitivity. $\tau^s_0(x)$ and $m^s(x)$ are related to the crystal deformation by slip. For the local non-linear constitutive equation $\sigma'(x) = M^{tg^{-1}}(x) : d(x) + S^o(x)$, the stress equation, including both the deviatoric and the hydrostatic pressure parts becomes

$$\sigma_{ij} = L^{tg_{ijkl}} : d_{kl} + S^o_{kl} - p\, \delta_{ij} \tag{3.18}$$

where $L^{tg} = M^{tg^{-1}}$ and δ_{ij} is Kronecker delta. For $\tilde{L^{tg}} = L^{tg} - L^{tg}_o$ and $\tilde{S^o} = S^o - S_{oo}$, taking the derivative of the stress constitutive equation and equating to zero to satisfy the equilibrium condition results in

$$\sigma_{ij,j} = 0 = S^{oo}_{ij,j} - p_{,i} + (L^{t\tilde{g}_{ijkl}}\, d_{kl} + \tilde{S^o_{ij}})_j + L^{tg}_{o_{ijkl}}\, d_{kl,j} \tag{3.19}$$

where $L^{tg}_{o_{ijkl}}\, d_{kl,j} = \frac{1}{2}(L^{tg}_{o_{ijkl}}\, v_{k,lj} + L^{tg}_{o_{ijkl}}\, v_{l,kj})$ because of the strain rate part of compatibility condition. Here, it is assumed that $L^{tg}_{o_{ijkl}}$ has minor symmetry. Thus, $L^{tg}_{o_{ijkl}} = L^{tg}_{o_{ijlk}}$, and $L^{tg}_{o_{ijkl}}\, d_{kl,j} = \frac{1}{2}(L^{tg}_{o_{ijkl}}\, v_{k,lj} + L^{tg}_{o_{ijlk}}\, v_{l,kj})$ As repeated indices are dummy indices, for *l=k and* k=l, compatibility condition is

$$L^{tg}_{o_{ijkl}}\, d_{kl,j} = \frac{1}{2}(L^{tg}_{o_{ijkl}}\, v_{k,lj} + L^{tg}_{o_{ijkl}}\, v_{k,lj}) = L^{tg}_{o_{ijkl}}\, v_{k,lj}\,. \tag{3.20}$$

Calling $(L^{t\tilde{g}_{ijkl}}\, d_{kl} + \tilde{S^o_{ij}})$ = τ_{ij}, the final system of differential equations to be solved becomes

$$\begin{aligned} L^{tg}_{o_{ijkl}} v_{k,lj}(x) + \tau_{ij,j}(x) - p_{,i}(x) = 0 \ in\ RVE \\ v_{k,k}(x) = 0 \ in\ RVE \\ Periodic\ BCs\ across\ RVE\ . \end{aligned} \tag{3.21}$$

Similar to the elastic case that is explained in section 3.1, the polarization field is calculated using the Green's method and FFT formalism.

Algorithm for viscoplastic FFT

The algorithm is initialized with strain rate $\tilde{d}^{\circ}$=0, and then the local stress-strain fluctuations are calculated iteratively [34].

a. Reference medium stiffness L^0 is initialized as a Voigt average.

b. Local stress at each grid point is calculated by solving the constitutive relation numerically via Newton-Raphson method.

c. Deviatoric stress, perturbation field and pressure field is calculated in Fourier space.

d. Stress and strain-rate fields are calculated from the constitutive equation.

e. Polarization field is calculated through Green's method and Fourier transform.

d. Stress equilibrium and convergence is tested.

e. New stress-strain fields are updated.

f. Steps b-e are repeated until convergence.

k. If the convergence is satisfied, the orientation and hardening parameters for each slip system are updated.

Elasto-viscoplastic formulation

An infinitesimal strain version of the FFT formulation in the elasto-viscoplastic regime was presented recently [93]. The solution in the elasto-viscoplastic regime involves the combined Hooke's law for the elastic part and Euler implicit time discretization for the plastic part. Briefly, the constitutive equation of giving the strain field is defined as

$$\varepsilon^{total}(x) = \varepsilon^{e}(x) + \varepsilon^{p}(x). \tag{3.22}$$

Equation 3.22 can also be written as

$$\varepsilon^{total}(x) = C^{-1}(x) : \sigma(x) + \varepsilon^{p,t}(x) + \dot{\varepsilon}^{p}(x,\sigma)\Delta t \tag{3.23}$$

where

$$\dot{\varepsilon}^{p}(x) = \dot{\gamma}_o \sum_s m^s_{ij} \left(\frac{m^s_{kl}\,\sigma_{kl}}{\tau^s_o} \right)^n . \tag{3.24}$$

Similar to the elastic and viscoplastic cases, the field fluctuations are defined, and then the the polarization field, which is the divergence of the perturbation field, is calculated iteratively using the Green's method and FFT formalism as explained in section 3.1.

Algorithm for elasto-viscoplastic FFT

The algorithm is initialized with the total strain $\varepsilon^{total}(x) = \varepsilon^{e}(x)$ as the total plastic strain is zero, and then the local stress-strain fluctuations are calculated iteratively [93].

a. Local fluctuation is established via $\tau_{ij}(x) = \sigma_{ij}(x) - C^0_{ijkl}\,u_{k,l}(x)$, and combined with equilibrium condition.

b. Local stress at each grid point is calculated by solving the constitutive equations.

c. Polarization field is calculated through Green's method and Fourier transform.

d. Stress equilibrium and convergence is tested iteratively.

e. New stress-strain fields are updated.

f. If the convergence is satisfied and if $\varepsilon^{p,t}(x) \neq 0$, the orientation and hardening parameters for each slip system are updated.

3.1.1 Orientation and hardening updates

Once the local stress fields converge to the boundary conditions, the microstructure needs to be updated for the deformation induced changes in viscoplastic and elasto-viscoplastic regimes. The first update is for the local orientation, which is simply the difference between the local rigid body rotation rate and the local plastic rotation rate. Mathematically, local reorientation w(x) is defined as

$$w_{ij}(x) = \left[\dot{w}_{ij}(x) - \dot{w}^{p}_{ij}(x) \right] \tag{3.25}$$

for local rigid body rotation rate $\dot{w}_{ij} = \frac{1}{2}(v_{i,j}(x) - v_{j,i}(x))$ and plastic rotation rate $\dot{w}^p_{ij}(x) = \sum_{s=1}^{N_s} \alpha^s(x)\dot{\gamma}^s(x)$ with $\gamma^s(x)$ local shear rate and $\alpha^s(x)$ local skewsymmetric Schmid tensor [34].

The second update is for work and latent hardening, which denotes the rate of change in critical resolved shear stress (CRSS) of a primary slip system for the former or the change in CRSS of a secondary slip system for the latter. The CRSS update should be performed according to a hardening law. For this work, a modified version of the Voce [95] hardening model is used with the assumption of only self-hardening (no latent hardening). Modified Voce hardening is characterized by an evolution of the threshold stress with accumulated shear strain in the form of

$$\hat{\tau}^S = \tau_0^S + (\tau_1^S + \theta_1^S \Gamma)(1 - exp(-\Gamma|\frac{\theta_0^S}{\tau_1^S}|)) \tag{3.26}$$

giving 4 parameters for each slip system in each individual phase, where τ_0^S is the initial critical resolved shear stress (CRSS), τ_1^S is the initial hardening rate, θ_0^S is the asymptotic hardening rate and θ_1^S is the back-extrapolated CRSS. Voce hardening is an empirical model, and since it does not have any temperature or strain rate sensitive terms it is intended to extract parameters from a single stress-strain dataset.

3.2 High Energy X-Ray Diffraction Microscopy

Generating or collecting accurate and volumetrically representative 3D microstructures is an essential part of the microstructure based mechanical modeling efforts. While the measurement of EBSD maps combined with serial sectioning is the most commonly used technique for obtaining 3D grain orientation maps [96], the improvements on third generation synchrotron radiation sources have attracted attention to non-destructive measurement techniques, making particle accelerator experiments an integral part of the image based modeling studies like the FFT based algorithm and CPFEM [97–100]. With their high energy, high brilliance, and micro-focused X-ray capabilities, synchrotrons are unique facilities for performing non-destructive grain and sub-grain scale microstructure mapping experiments in reasonable measurement times [101]. Amongst multiple diffraction based techniques, e.g., diffraction contrast tomography (DCT) [102], 3D X-ray diffraction microscopy (3DXRD) [104] and differential-aperture X-ray microscopy (DAXM) [103], we use the high energy X-ray diffraction microscopy (HEDM) in this work for its good spatial and angular

resolution, owing to the high-resolution area detectors and the X-ray focusing optics capabilities of Advanced Photon Source (APS) [105, 106].

HEDM is a non-destructive 3D microstructure mapping method, in which monochromatic high energy x-rays from a synchrotron source, in this case the APS at Argonne National Laboratory, are used to probe and non-destructively characterize bulk samples [105, 106]. When x-ray photons interact with the sample, they are either absorbed, transmitted or scattered [104]. The HEDM technique is based on the elastic scattering of X-rays, which assumes weak interactions between the X-rays and the atoms of the sample for X-rays to diffract off of electrons when they satisfy the Bragg's condition. The spatially resolved HEDM experiment involves collection of diffractograms by a near-field detector, which means that the detector is only about a few milimeters away from the specimen in order to extract spatial grain orientations and shapes; hence it is referred to as near-field HEDM, Fig. 3.1. The distance of the detector from the rotation center changes the modality of data collection, e.g., when the detector distance L seen in Fig. 3.1 is a few mm, the diffraction peaks carry information on grain and subgrain level morphology and spatial orientations, whereas when the detector sits far away, a few hundreds mm from the rotation axis, collected data carries average information, such as the average grain orientation and grain center of mass, however an additional lattice strain information can be extracted from this far-field HEDM modality.

The sample, sitting on a rotation stage, is probed by a monochromatic X-ray beam, with ideally $\sim$1.3 mm width and 1-2 μm height, depending on the performance of the upstream optics [107]. When sample is illuminated, the grains satisfying the Bragg's condition, $n\lambda = 2d_{hkl}\sin\theta$, where n is an integer and d_{hkl} is the spacing between atomic planes, or defined in the reciprocal space through Laue condition when scattering vector Q is equal to reciprocal lattice vector G, as $|Q| = 2|k|\sin\theta$, scatter the beam, and the diffraction data is collected on the CCD detector. A scintillator material is placed in front of the detector to convert X-rays into visible, and a tungsten beam block is used to attenuate the direct beam in order to prevent detector saturation, seen in Fig. 3.1.b. With the current setup, only upper hemisphere diffraction data is collected. The position of the diffraction spot on the detector depends on its point of origin in the specimen, and also the diffraction vector Q=$k_i - k_f$ where k_i is the incident wavevector and k_f is the scattered wavevector. For each material, the cross sectional sample size is limited by the penetration depth of the X-rays for that material, which is a function of the photon energy. Typical HEDM measurements are performed at 50-90 keV. Being

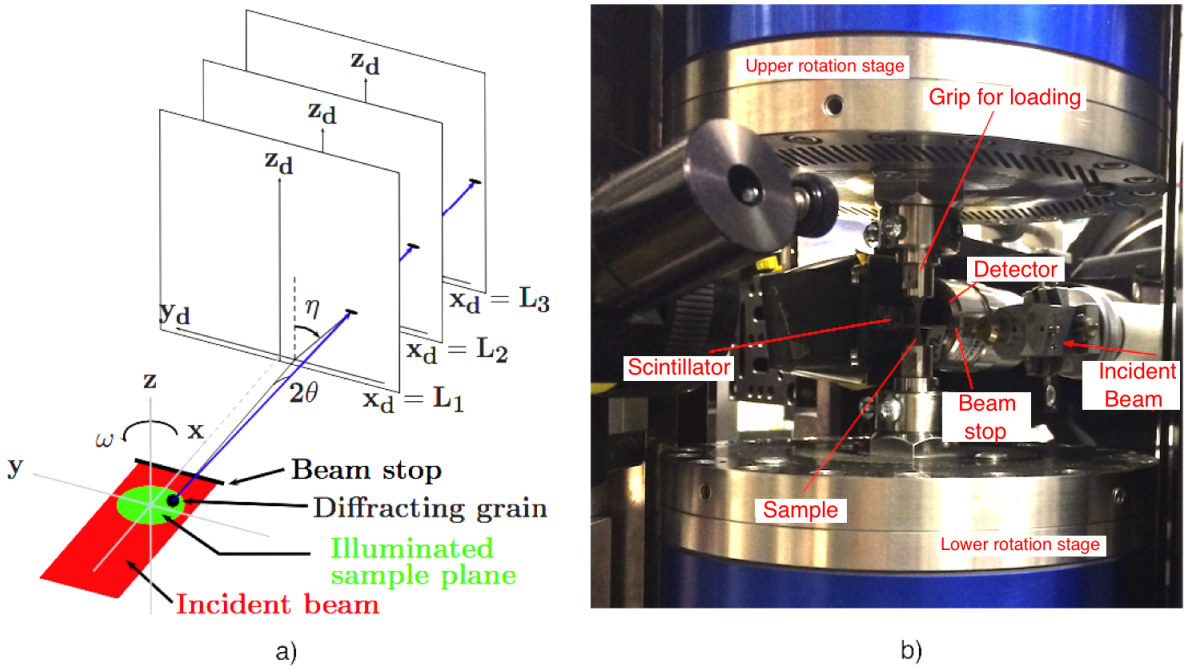

Figure 3.1: a) Schematic of the nf-HEDM experimental setup [105], b) Actual setup in the hutch, where sample is gripped in the loading stage for an in-situ experiment.

efficient for the monochromator and being in the range of 1mm extinction length for titanium, the data for this thesis work was collected at 51.996 keV by calibrating the beam by the Tb K-shell absorption edge.

After the beam is tuned, the detectors, slits and lenses are calibrated, and beam is centered on the detector, a calibration specimen (usually an ordered, undeformed, well characterized gold sample) is characterized in order to extract the geometrical setup parameters, which are then used in the virtual replication of the experiment for the forward modeling reconstruction [106, 107]. The geometrical parameters are specimen-to-detector distance L, and the point of intersection of the focused X-ray beam and the rotation axis, (j, k) with j horizontal and k vertical positions on the detector. A comparative diffraction illustration of an undeformed Au with well defined grains vs. an additively manufactured aluminum alloy in high residual stress state with very small grains is depicted in Fig. 3.2, in order to emphasize the importance of collecting a calibration dataset. The current implementation of the forward modeling reconstruction requires binarized images of the raw data through peak segmentation. As seen in the multiple intensity projected images of Au and Al (so each image carries information full rotation range) in Fig. 3.2, binarization of small and deformed grain

diffraction peaks of Al is not an easy task, and if not done properly it would introduce uncertainty in geometrical parameter optimization. Hence, for the reconstruction is sensitive to the experiment parameter [108], a calibration data acquisition is a precursor for successful post-processing.

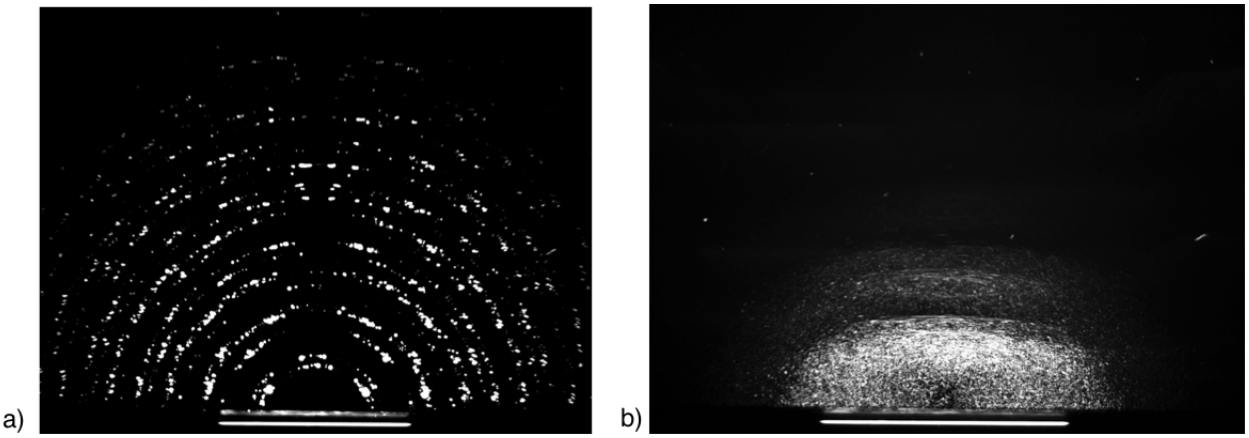

Figure 3.2: Maximum intensity projected (from full rotation range of 180°C) raw detector images of a) Undeformed Au with large, well defined grains, b) A high residual stress state aluminum, with small, segmented grains.

To acquire 3D maps non-destructively, the sample is simply moved in z (or y in APS coordinate system) direction the desired step size, and diffractograms are repeatedly collected from the next layer as the sample is rotated about the vertical axis in typically half or one degree increments through 180°C of rotation, with two or three different stand-off distances for the detector at each rotation position. Using multiple detector distances is essential in determining the grains' position of origin within the sample. With the detector pixel pitch of 1.48 μm, tracking the same diffraction peak through different L distances gives a pixel size in-plane resolution when the experiment parameters are calibrated properly.

Reconstruction of the 3D orientation map relies on a forward modeling algorithm [105, 107]. After the detector parameters are optimized from the calibration sample through a Monte Carlo simulation, the reconstruction software IceNine [109] virtually generates the experiment by including the beam, sample and the detector, and for the given experiment geometry simulates the Bragg scattering at each voxel for the orientation list that spans the fundamental zone of the material's crystal structure. The voxel in this context is a triangular mesh element that is obtained by discretizing the sample cross section. The simulated diffraction is compared to the binarized experimental peak, and a best fit is selected. The quality of the fit is quantified by confidence as C=$\frac{N_{overlap}}{N_{simulated}}$, with $N_{overlap}$ denotes the number of simulated peaks that overlap with the peak from the segmented image, and

$N_{simulated}$ denotes the total number of usable peaks for that orientation which intersect more than one detector distance [108]. Confidence is not an absolute measure of fit wellness as it is a function of the maximum scattering vector used in the simulation (higher Q_{max} means more simulated peaks intersect detectors along the vertical detector position, hence confidence of the same experimental peak may drop at a higher Q_{max} fit), however it can be a good measure of comparison between different voxels, layers, and material states. The simulated orientation that gives the highest confidence is assigned to an individual voxel, and the same process is repeated for each voxels of each rotation angle of each detector distance. Once the reconstruction of a individual layers are completed, they are stitched together to generate the 3D grain and orientation map [97].

In summary, nf-HEDM is a very capable and robust non-destructive technique for volumetric grain structures and orientation mapping. Owing to be developed in the high brilliance and high energy X-ray facility APS, it is possible to collect large dataset in reasonable measurement times. The technique provides unique in-situ capabilities to track microstructural evolution with loading, or temperature change. While the nf-HEDM reconstruction algorithm is not yet adept to extract strain information, far-field HEDM (ff-HEDM) technique can be used for lattice/residual strain measurements and phase segmentations [110]. Combining the ff-HEDM strain and phase measurements, x-ray computed tomography density measurements and the nf-HEDM grain structure and orientation measurements ensures the full microstructure characterization, and provides the in demand input and calibration datasets for mechanical deformation models.

CHAPTER IV

Advanced Microstructure Characterization and Tensile Property Measurement of Electron Beam Melted Ti-6Al-4V

Powder bed based EBM, a layer by layer processing technique, is shown to induce microstructural heterogeneity and property anisotropy on the built parts due to thermal gradient left behind the melt pool and along the build height, which has been discussed in detail in Chapter 2.5.2. The layer by layer nature of the process is hypothesized to result in a graded microstucture along the build height. While many studies investigated this expected microstructural variation, the published works are inconsistent in the reported mechanical properties, grain morphologies and grain sizes in relation to the build height. For instance, while Murr et al. reported average thickness of 3.2 μm acicular alpha platelet at the top 1 cm vs. average thickness of 1.6 μm lamellar like alpha platelet at the bottom 1cm for a 40 mm build, [16], Hrabe et al. did not observe significant change on the microstructure and mechanical properties with varying build height for a 27 mm tall build [76]. Lu et al.'s fully columnar prior beta throughout the build height [83] is challenged by Tan et al.'s findings of equiaxed prior beta at the bottom layers that coarsens with build height [84], which in turn affects the transformed α colony size, a significant determinant of mechanical properties [2]. Tan et al. and Wang et al. report decreased tensile properties with build height, whereas Machry et al. reports a slight increase in the strength along the build height when the component is a thick wall block (specimens that of > 18 mm diameter) [112], and Hrabe et al. reports a statistically insignificant relationship between distance from the build plate and the tensile properties as the tensile and yield strength values are within natural scatter expectations [76]. In addition to insufficient conclusions on the influence of build height on the microstructure and mechanical properties in the view of industrial applications and academic interest, large area crystallographic orientation scans are found to

be limited in the literature [67, 82], which is potentially a scattering factor for the properties (e.g., if the similarly oriented colonized alpha regions at certain build heights are larger or smaller in certain build heights). The nf-HEDM technique, explained in detail in Chapter 3.2, can be utilized to fill the need of large area texture evolution characterization as it allows one to non-destructively characterize large scale spatially resolved grain structure and crystallographic orientation in reasonable measurement times. In this chapter we present the application of the nf-HEDM technique to powder bed EBM processed, 3D printed Ti-6Al-4V parts, coupled with build height sensitive ex-situ tensile property measurements. The novelty of the presented advanced characterization work is justified by being the first study that used high-energy X-Ray diffraction for high throughput 3D mapping to non-destructively capture the effects of build height, process parameters and heat treatment on the resulting microstructure (grain structure, porosity via CT and full-field orientation distribution) of the spatially heterogeneous additively manufactured Ti-6Al-4V. The novelty of the presented tensile measurement study is that the full stress-strain curves are reported which are then used to systematically extract location specific Voce hardening parameters to be utilized in computational efforts of micromechanical modeling.

4.1 Advanced Microstructure Characterization via High Energy X-Ray Diffraction Microscopy

4.1.1 Introduction

Additive manufacturing is increasingly being evaluated and implemented to produce structural metallic components. While the benefits of such a manufacturing process are often discussed (e.g., near-net shape, reduced machining costs, more complex shapes), the nature of the parts' thermo-mechanical history and its influence on the microstructure and mechanical properties is not well established, which has been extensively discussed in Chapter 2.5. Compounding the problem are the challenges of most non-destructive evaluation techniques on materials that are either textured or exhibiting spatially varying residual stress or microstructural scale, attributes that are often associated with structural metallic materials produced using various additive manufacturing approaches. The purpose of the presented synchrotron characterization work is to advance the understanding of process dependent grain structure characteristics of additively manufactured Ti-6Al-4V by pushing the spectral limits of the nf-HEDM experiment and computational limits of the reconstruction algo-

rithm due mentioned small grains, residual stress and textured nature of AM titanium. As the first, or among the first studies that utilized the nf-HEDM technique for high throughput 3D mapping of additively manufactured titanium alloys, the effects of build height, process parameters and heat treatment on the resulting microstructure were successfully captured. Furthermore, using the collected sets of 3D microstructure images as input for FFT based micromechanical model, detailed in Chapter 3.1, integrated the experimental and computational efforts, which is discussed at the end of this section.

4.1.2 Material and methods: Electron beam melted Ti-6Al-4V and high energy X-ray diffraction microscopy

Material: EBM Ti-6Al-4V

The EBM Ti-6Al-4V materials of this study were built on an Arcam A2 machine at North Carolina State University for a preceding high energy X-ray computed tomography experiment [68], using standard pre-alloyed recycled Arcam AB Ti-6Al-4V (Grade 5) powder, with supplier reported typical chemical composition of 6 % Al, 4 % V, 0.03 % C, 0.1 % Fe, 0.15 % O, 0.01 % N, 0.003 % H and Ti to balance, and with nominal powder size distribution of 45 - 100 microns. It should be noted that for this study no chemical composition measurements were performed on the feedstock, and the chemical composition of the Ti-6Al-4V powder and the manufactured parts can be outside of the supplier reporter values as recycled powder is utilized in printing the samples. Beuth et al.'s process mapping approach demonstrating that the beam power and velocity can be correlated with the melt pool geometry [113], and Narra et al.'s findings on how to obtain constant melt pool cross sectional area [114] was practiced in the Cunningham et al. study, by systematically varying the Arcam proprietary beam speed function, to produce 1/4, 1/2, 1, 2 and 4 times the nominal value melt pool cross-sectional area. Arcam beam speed function is a standard build theme for Ti-6Al-4V, for which the beam parameters of power and velocity are controlled according to a manufacturer developed algorithm in order to fabricate fully dense parts with microstructural consistency. While it is roughly related to energy input and beam speed as an inverse relationship with power and direct relationship with velocity, e.g., speed function 36 for nominal melt pool area is a low power high velocity setting and speed function 10 for 4X melt pool area is a high power low velocity setting, the specific values of beam speed and beam current are not known as the build theme varies them con-

Table 4.1: Calculated average α lath width size and β phase fractions for the 1X and 4X melt pool area samples

	4X	2X	4X
Average α width [μm]	1.5 ± 0.52	2.8 ± 0.51	3.6 ± 1.0
β fraction (%)	5.7 ± 1.5	9.7 ± 0.30	11.1 ± 0.07

stantly throughout the printing. For all of the different parameter builds, the build layout consisted 3 cm diameter x 9 cm tall cylinder blocks, for which the hatch spacing, layer thickness, build plate temperature and beam spot size were kept at the nominal values of 200 μm, 70 μm, 750 °C, and machine calibrated spot size respectively. The hatching was rotated by 90 ° to form a criss-cross, after each layer was deposited [68].

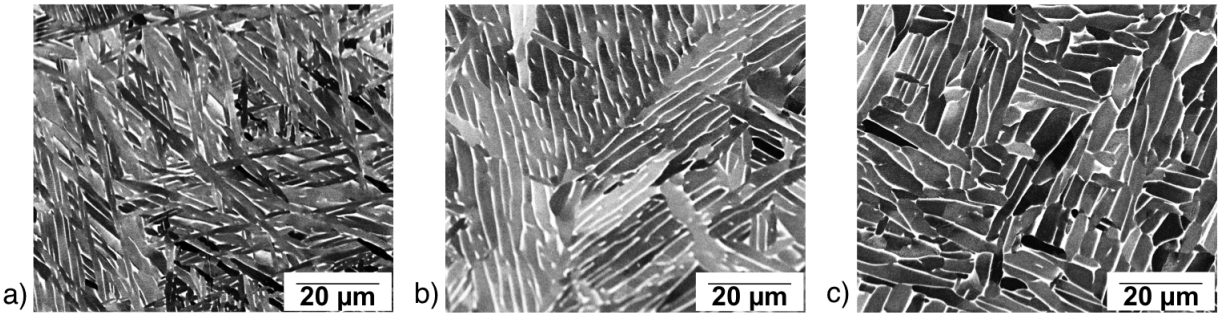

Figure 4.1: SEM-BSE micrographs of EBM Ti-6Al-4V with with bright phase bcc structure and dark phase hcp structure a) 1X melt pool area sample, b) 2X melt pool area sample, c) 4X melt pool area sample. Higher power - lower velocity settings result in an increased alpha lath width and beta phase fraction.

A preliminary microstructure characterization is an important precursor of any HEDM experiment to ensure the grain size and texture of the material is suitable for the nf-HEDM experiment, and the experiment is reconstructable, e.g., there are enough diffraction spots, and the material does not give powder patterns. For that purpose, Ross Cunningham's EBSD maps, one of which is presented in Fig. 2.13 for the nominal 1X melt pool area, and his Quanta 200F Secondary Electron Microscope (SEM)/Back Scattered Electron (BSE) 1500x magnification images of the 1X, 2X and 4X meltpool area samples, presented in Fig. 4.1, are utilized. Seen in Fig. 4.1 and Table 4.1, the average α lath sizes are 1.5, 2.8 and 3.6 μm respectively for the three settings, on top of the highly textured nature of the material. Based on these factors the decision was made to machine out six HEDM samples from the 1X and 4X melt pool area AM blocks with a low speed abrasive saw, from near the center of each sample with dimensions of 1 mm x 1 mm x 8 mm. One of each different process setting of the machined samples are kept at the as-built stage, one of each are stress relieved

at 650 ° for 3 hours, and the remaining two are annealed at 800 ° for 4 hours for nf-HEDM, pictorially shown in Fig. 4.2. This chapter discusses the reconstructed maps from the 1X and 4X as-built and annealed samples, labeled in red in Fig. 4.2.

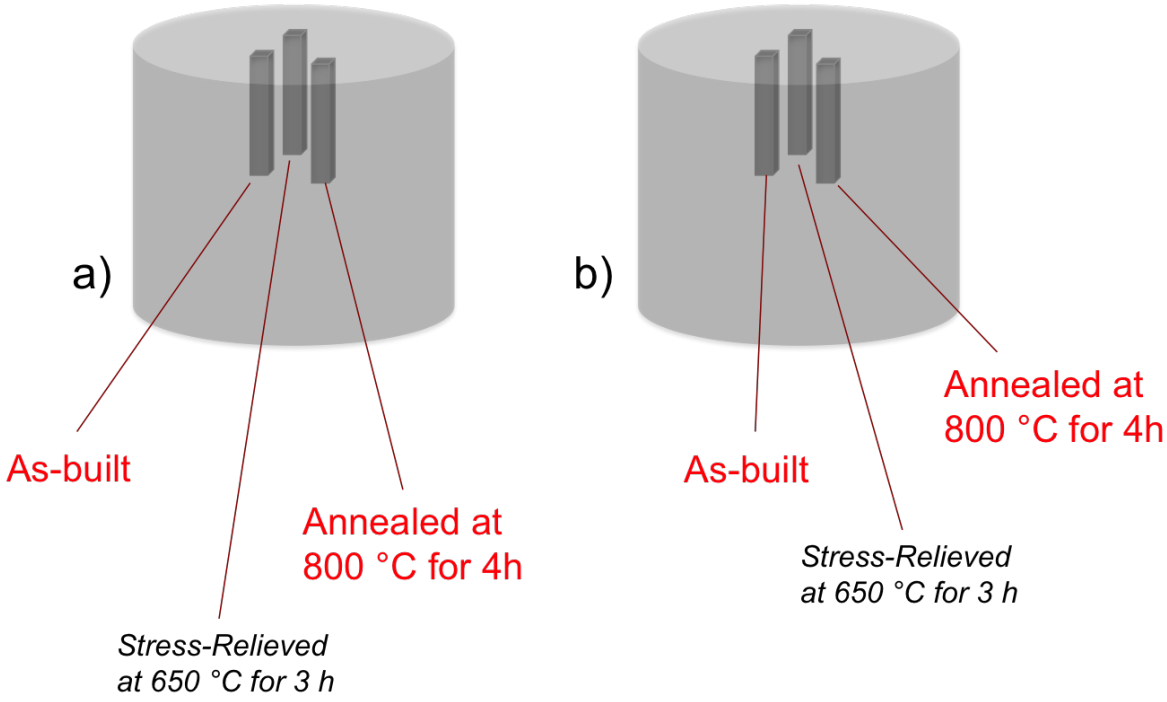

Figure 4.2: Illustration of prepared HEDM samples with as-built, stress relieved and annealed states, a) 1X melt pool area sample, b) 4X melt pool area sample. This chapter presents results on the as-built and annealed states, labeled in red in the figure.

High energy X-ray computed tomography measurements

X-ray computed tomography (XCT) is a non-destructive absorption based technique that is used to map the internal and external structure of a material by using the projected still images (two-dimensional radiographs) of a rotating sample in extracting the 3D structure. It is widely used in industry as a non-destructive evaluation tool to inspect the density of the materials. As mentioned previously, the parent specimen from which the HEDM samples are machined out from were additively fabricated for a preceding synchrotron based tomographic evaluation study. With this prior high-energy X-ray microtomography (μXCT) measurements at APS 2-BM beamline, size, shape and spatial distribution of internal defects (pores) were successfully quantified and reported by Cunningham et al. [68]. The HEDM samples were also characterized at 2-BM, in order to measure the tomographic density of the parts. Using white beam at 60 keV to ensure full penetration through the

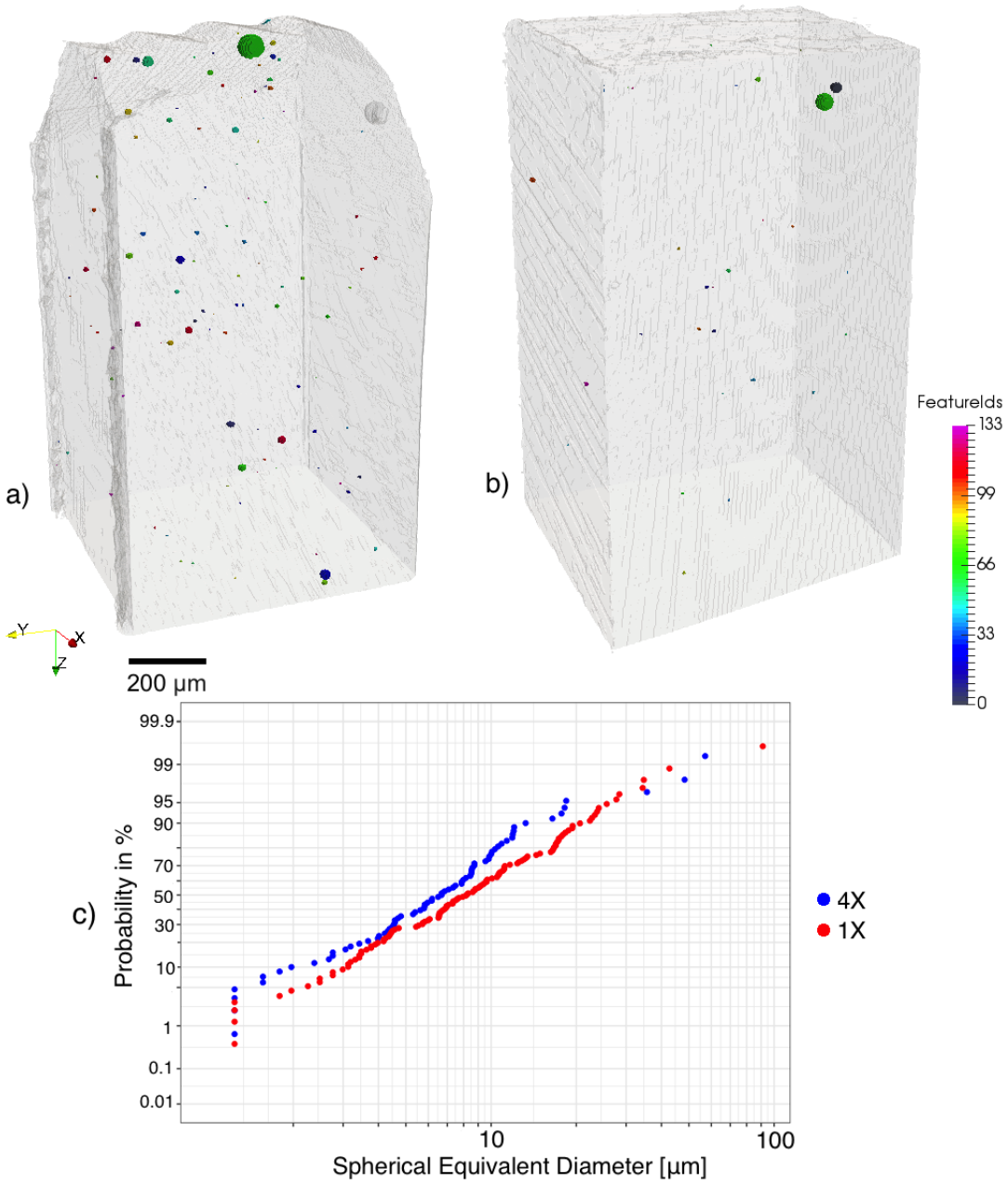

Figure 4.3: Synchrotron XCT results of a) 1X melt pool area sample, b) 4X melt pool area, c) Cumulative probability plots

thickest 1.5 mm dimension of the rectangular samples, 1500 sinograms, collected over a rotation range of 180°, were reconstructed into 3D data using gridrec reconstruction algorithm implemented to the tomographic data reconstruction software tomopy, which is an open source package developed by 2-BM beamline scientists. Spatial resolution limit of 0.65 μm at 2-BM beamline led to imaging the pores that are below the HEDM resolution capabilities (1.48 μm pixel pitch). Tomo-

graphic density measurement gave a density of 0.9653 % for the top 1.5 mm of the 1X sample, and it gave a density of 0.99101 % for the top 1.5 mm of the 4X sample. The difference of porosity distribution within these two samples is depicted in Fig. 4.3.a-b. Usually a licensed program such as Avizo is utilized for the XCT analysis. For this study, a new DREAM.3D pipeline consisting of thresholding, segmentation, neighbor analysis, equivalent diameter calculation and visualization is developed. XCT observations of the HEDM samples were similar to the previous XCT study [68], with log-normal size distribution of the pores for both 1X and 4X cases, Fig. 4.3.c, with larger melt pool area 4X sample having a smaller size distribution than the nominal 1X case.

High Energy X-Ray diffraction microscopy measurements

Non-destructive nf-HEDM experiment, which is detailed in Chapter 3.2, was performed at 1-ID beamline of APS using a monochromatic line focused 51.996 keV X-ray beam. This energy was specifically tuned, as the X-ray optics are efficient at this range, and it is high enough energy for illuminating the 1.3 mm cross sectional dimension of our titanium samples. Normally multi-modal measurements of combined tomography and nf-ff HEDM can be performed at 1-ID, however in our case tomography was performed at 2-BM. With the current setup of the experiment, it is possible to obtain 1.48 μm spatial resolution (pixel pitch of the nf-HEDM detector Retiga 4000DC) and 0.1 $^\circ$ angular resolution when components are stable, well aligned, focused, and centered. As our samples are challenging in nature for the nf-HEDM experiments, which is detailed later in this section, the detector-optics-beam calibration and focusing steps were executed with careful attention so that we could obtain the optimum angular and spatial resolution. Installment of a superconducting undulator (SCU) device at Sector 1 prior to our experiment allowed faster data collection due higher number of photons, ergo decreased integration time per frame. Despite some data acquisition challenges such as cropped images due hardware-software synchronizing issues and beam losses, a total of 6 samples were characterized on different degrees of volumes, with varying AM processing parameters (a set of three built at high velocity-low power, a set of three built at low velocity-high power) and varying heat treatments (for both processes one as-build, one stress relieved and one annealed sample).

For our samples, average alpha lath width of 1X and 4X bulk samples were known as 1.5 $\pm$ 0.5 and 3.6 $\pm$ 1 μm from the precursor microstructure characterizations, which is near the spatial resolution limit of the technique if each alpha lath grain were to carry different crystallographic

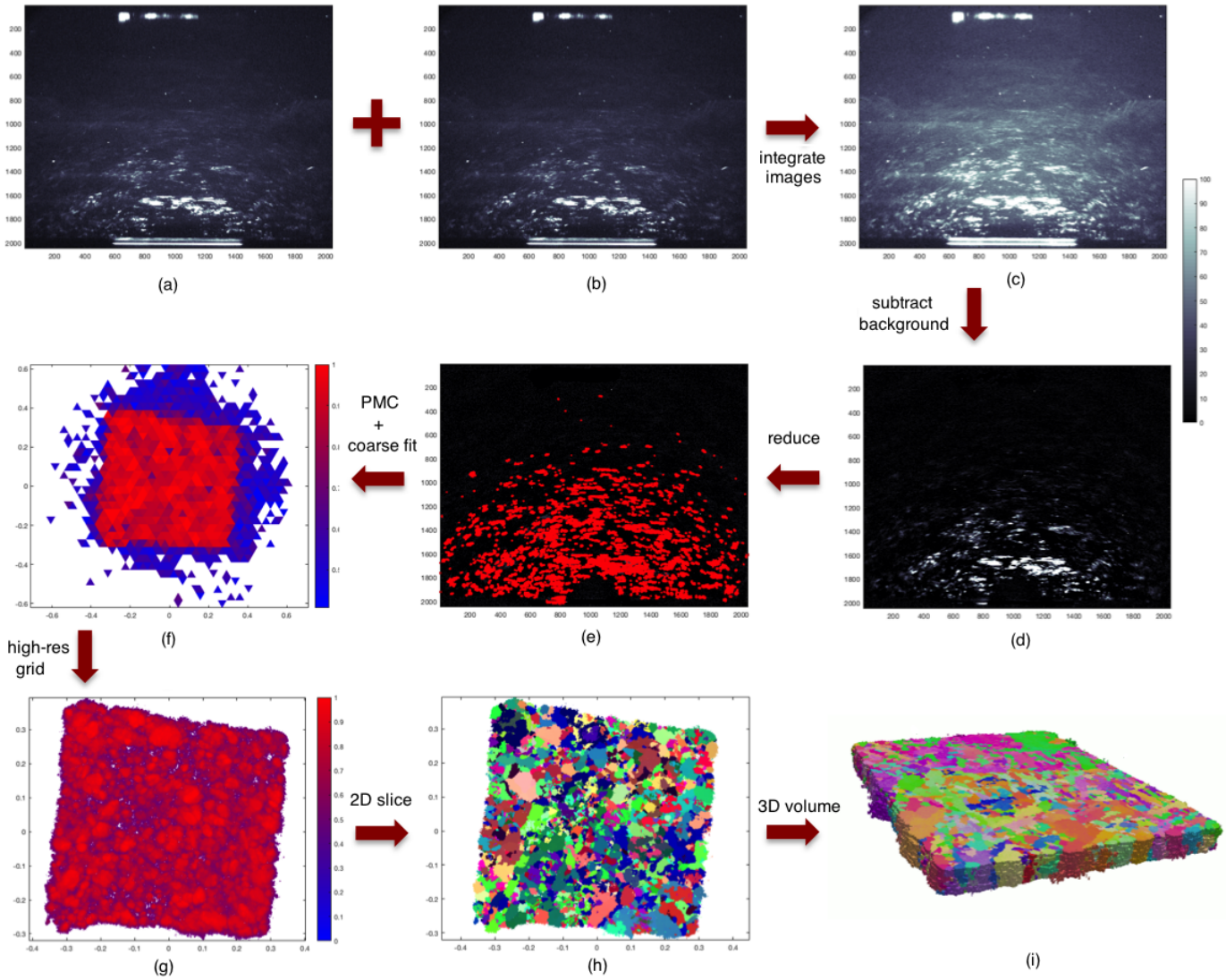

Figure 4.4: Workflow for reconstructing nf-HEDM data at the at the experimental and computational limits: a-b) Raw diffraction images of consecutive frames, c) Integrated image, d) Background subtracted image, e) Reduced binary image overlapped with background subtracted image, f) Coarse grid fit confidence map, g-h) Confidence and Rodrigues vector colored orientation map of reconstructed 2D slices, i) IPF colored Orientation map of 3D volume. Workflow consists of integrating consecutive raw images to reduce the binary image size and the number of diffraction spots, background image generation using a subinterval of the rotation range for reducing texture affected systematic errors, data reduction, parameter Monte Carlo optimization for each layer when the beam is shifting or the detector stage is thermally settling, a coarse grid fit for extracting the sample geometry, which is then used for creating a mask grid that limits the search space, fine scale 2D fit of layers, and finally stitching 2D slices into a 3D volume.

orientations. In addition to the small features, the textured nature of AM materials and the existence of residual stress imposed more complexity for the experiment by creating systematic errors in diffraction peak intensities due to texture and smearing the diffractions spots due to residual deformation, which raised the question of whether or not the far from ideal diffraction data, shown in Fig. 4.4, was reconstructable. With the advancements in the reconstruction algorithm [107], the

background subtraction method [145], error analysis study [108], knowledge built from the previous experiments [97], and the fact that alpha laths, although being small in size colonize in similar crystallographic orientations, we could reconstruct up to maximum scatter vector Q = 6 A $^{-1}$, corresponding to the (222) family of planes for the bcc crystal structure. Because there are a few hundred thousand diffraction spots per half a degree rotation interval over a rotation range of 180°, and we wanted good spatial resolution in the reconstructed maps by reconstructing the data on a uniform triangular grid of side width 1.405 μm, the data reduction and reconstruction steps were expected to be computationally very expensive. For this reason, a series of accelerating steps were implemented in the reconstruction process, illustrated in Fig. 4.4.

4.1.3 Results and discussion

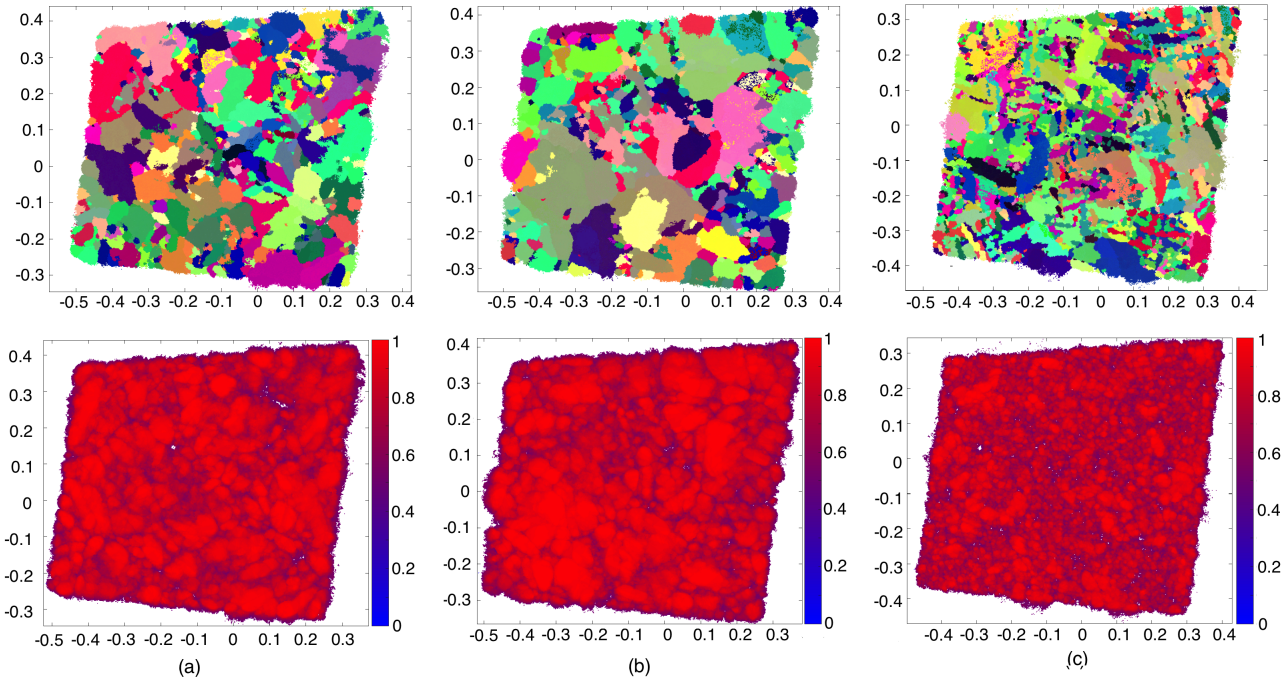

Figure 4.5: HEDM reconstructed orientation and confidence maps of the 0.1 mm, 0.85 mm and 3 mm from the top regions of the 4X meltpool area sample. x and y values represent the location of the sample [mm] in relation to (0, 0) rotation axis.

As one of the first teams that utilized synchrotron high-energy X-Ray diffraction technique for high throughput 3D mapping of additively manufactured titanium alloys, we were able to non-destructively capture the effects of build height, process parameters and heat treatment on the resulting microstructure of the spatially heterogeneous AM Ti. Measured dataset is summarized in

Table 4.2: Summary of measured sample conditions, volumes and locations

Sample	Condition	Volume and Location of Measurement
4X Melt Pool Area	As-Built	1 layer at 0.1 mm from top
		1 layer at 0.85 mm from top
		8 layers at 3 mm from top
		1 layer at 4 mm from top
		1 layer at 4.75 mm from top
	Annealed at 800° C	1 layer at 0.25 mm from top
		1 layer at 1.25 mm from top
		20 layers at 5.5 mm from top
1X Melt Pool Area	As-Built	1 layer at 0.25 mm from top
		1 layer at 1.25 mm from top
		8 layers at 3.75 mm from top
	Annealed at 800° C	1 layer at 0.25 mm from top
		15 layers at 4.5 mm from top

Table 4.2, with the reconstructed subset that is discussed in this thesis work highlighted in red amongst the full list of collected volume. Before setting volume scans, an incremental fast sweep was performed to check the diffraction spots along the build height. Inspecting raw detector images revealed smeared low Q scattering peaks near the top of the build, seemingly diffracting from larger than expected grains, whereas towards the bottom the grains got marginally smaller and the peaks shifted to higher Q scattering. Because the shift of behavior for each sample was observed in different regions, the scanning location in relation to the build height is inconsistent in between samples, as we wanted to make sure the collected data was reconstructable.

High power low velocity 4X melt pool area sample was reconstructed for the full volume in the as-built state for grain size and texture comparison. By limiting the detector area to maximum Q = 6 range, a good fit confidence was obtained for all 12 layers of the samples. Orientation and confidence maps of the first, second and third measured layers, which are 0.1 mm, 0.85 mm and 3 mm below the top of the build respectively are presented in Fig. 4.6. The grain size and orientation distribution change between these layers is clearly seen qualitatively from the images.

In order to quantitatively investigate the differences in microstructural features, Kernel Average

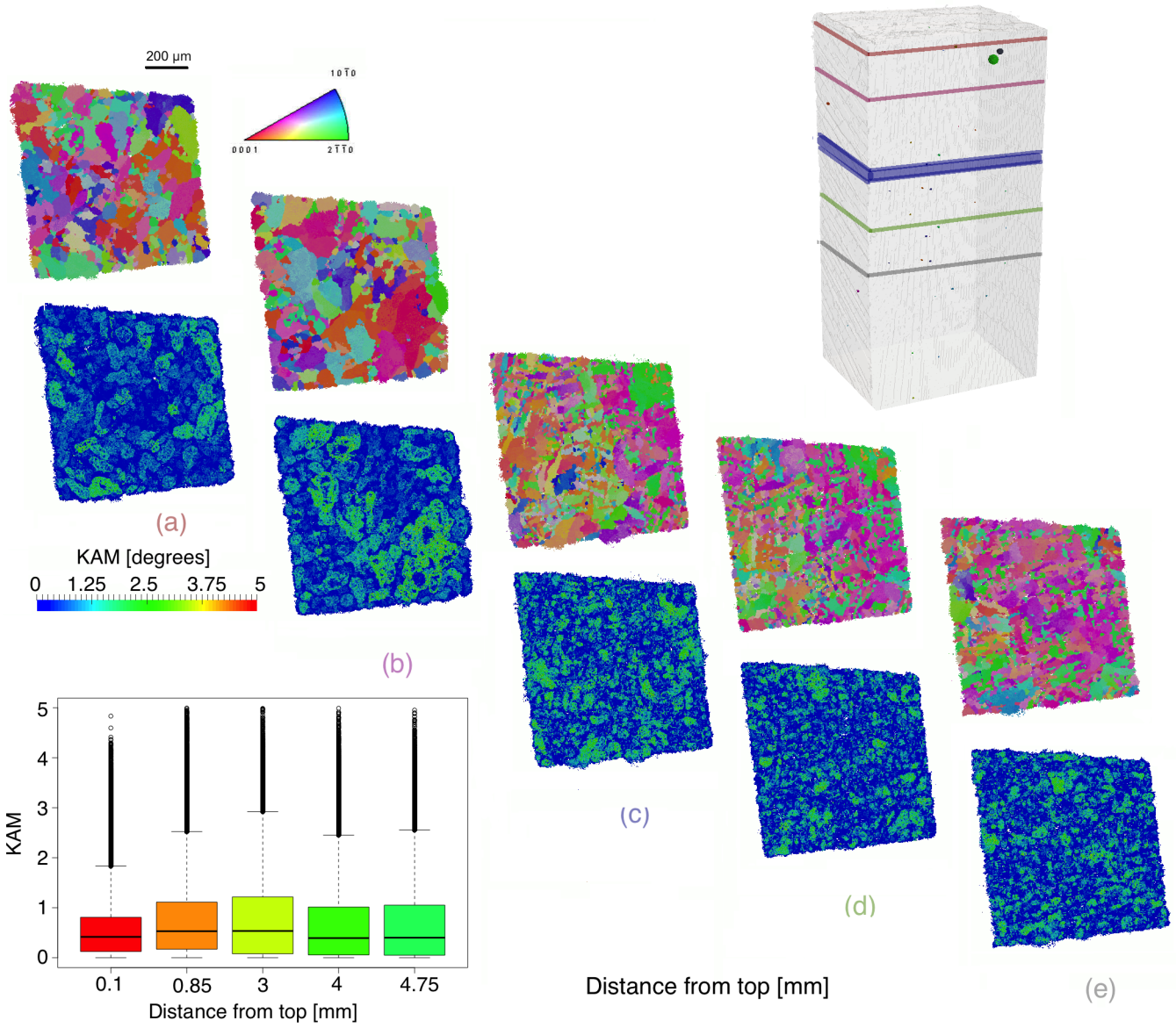

Figure 4.6: Orientation and KAM distribution maps of reconstructed layers of a) 0.1 mm from the top, b) 0.85 mm from the top, c) 3 mm from the top, d) 4 mm from the top and e) 4.75 mm from the top. The approximate positions of the layers are illustrated on the tomography image of the same sample. The KAM values are also represented with box plots in order to quantitatively compare the calculated values.

Misorientation (KAM), logarithmic cumulative probability plot of the normalized grain size diameter and pole figure matrices are constructed. KAM is defined as the average misorientation angle between each voxel and its 8 nearest on-plane neighbors. For our calculations, misorientation angles greater than 5 degrees are excluded from the computation to separate grain boundaries from KAM values, as the grain segmentation threshold is chosen as 5 degrees as well. In Fig. 4.6, KAM distributions of the 0.1 mm, 0.85 mm, 3 mm, 4 mm and 4.75 mm layers from the top are presented

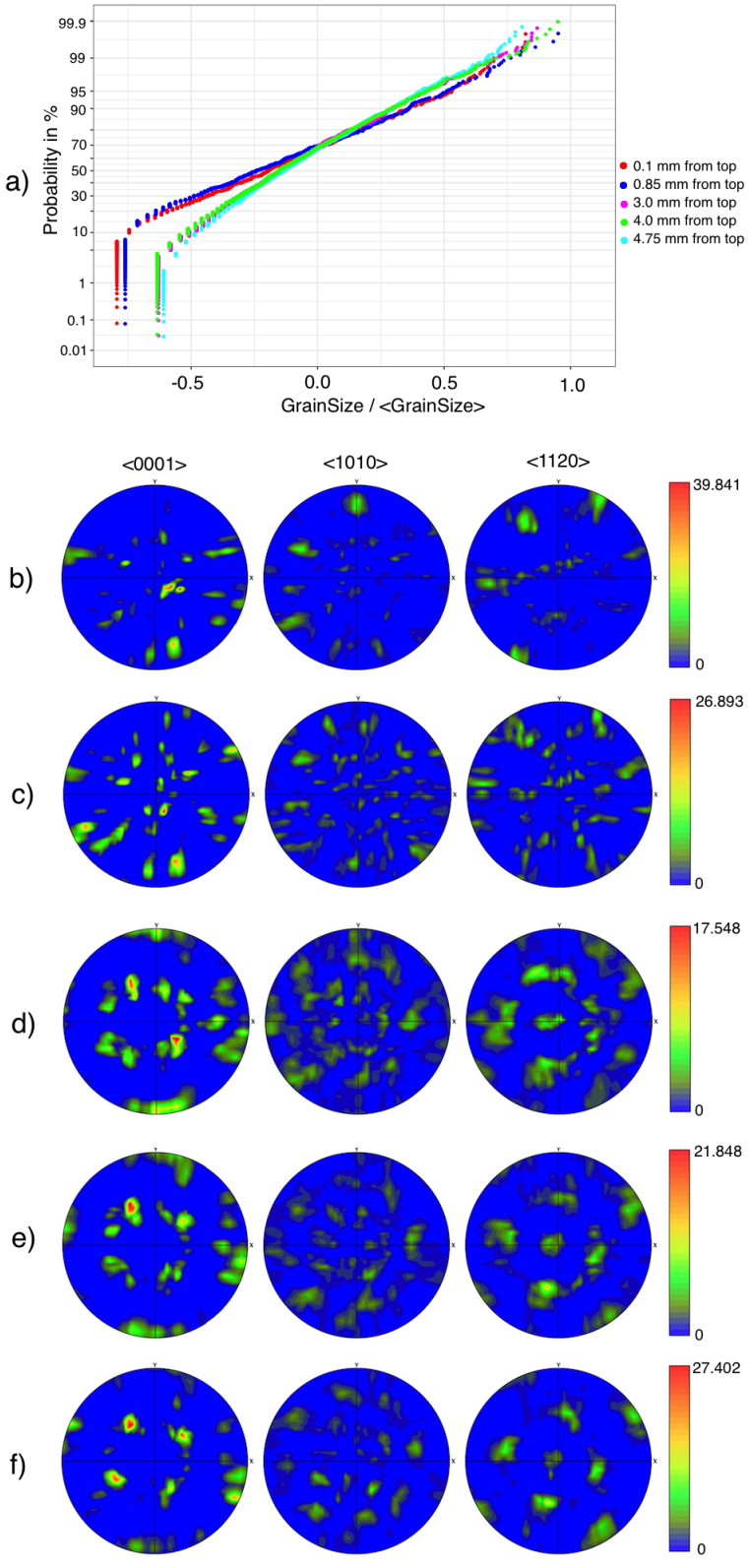

Figure 4.7: a) Normalized alpha grain size distributions and b-f) Texture data of the reconstructed alpha phase for the 0.1 mm, 0.85 mm, 3 mm, 4 mm and 4.75 mm from the top respectively. For all locations a strong texture was calculated, and a shift towards expected AM texture was observed after the top 1 mm of the sample.

with their corresponding orientation maps in IPF color, and box plots in order to quantitatively compare the calculated values. 0.75 and 3 mm layers from the top are concluded to have the highest residual strain, as KAM values within these layers is found the largest. It is important to note that in this study KAM was chosen to focus on local small rotations (smaller than the grain segmentation threshold), however using KAM carries the risk of amplifying the noise, and to overcome this problem the grain average misorientation metric can be utilized when the interest is in measuring the deviation from an average orientation. The normalized grain size distributions presented in 4.7.a showed a shift in distribution from large, clustered grains at the top 1 mm of the sample to smaller grains at the lower layers, as the comparison of the upper tail of the distributions which is the area of large grains has a higher probability value for the topmost layers. Texture data of the reconstructed alpha phase was also extracted from the orientation maps and presented in standard hcp pole figures in Fig. 4.7.b-f. For all locations a strong texture was observed, indicated by the multiples of random (MRD) values of < 17. MRD refers is a measure of how strong the texture is in relation to a random distribution, i.e. 39 MRD of the top layer means that the texture is 39 times stronger than if they were to be random. It is also important to note the formation of expected texture after the top 1 mm of the sample as one of the expected alpha pole directions of [1120] is observed after the third layer, depicted in Fig. 4.7.d-f.

Investigation of the effect of process parameters and heat treatment was possible through comparing 1X and 4X samples after different post-processing treatments. Top layers of the reconstructed 1X as-built, 1X annealed, 4X as-built and 4X annealed samples were compared in Fig. 4.8. Average alpha sizes (combination of colonized alpha and resolved laths) are calculated as 8.59, 9.58, 14.01 and 14.53 μm respectively, for when grain boundary threshold is defined as 5 degrees. Calculated grain sizes are illustrated with violin plots, which are similar to box plots with the exception of showing both the distribution of the data and its probability density, revealing the long upper tail for the 4X annealed sample, which is shown in Fig. 4.8.c. This plotting convention is convenient for qualitative comparison as it can easily capture trends in distributions. While the high power processing settings and post-process heat treatment is found to systematically coarsen the grain size as expected, the texture evolution results were inconclusive. In terms of process effects on texture, lower solidification rates of the high power setting may have caused the slightly sharper texture of the 4X sample in comparison to the 1X. In terms of post-process effects on texture, as annealing the

samples at 800 ° for 4 hours was below the beta transus temperature, the initial conditions of the prior beta texture was preserved after annealing.

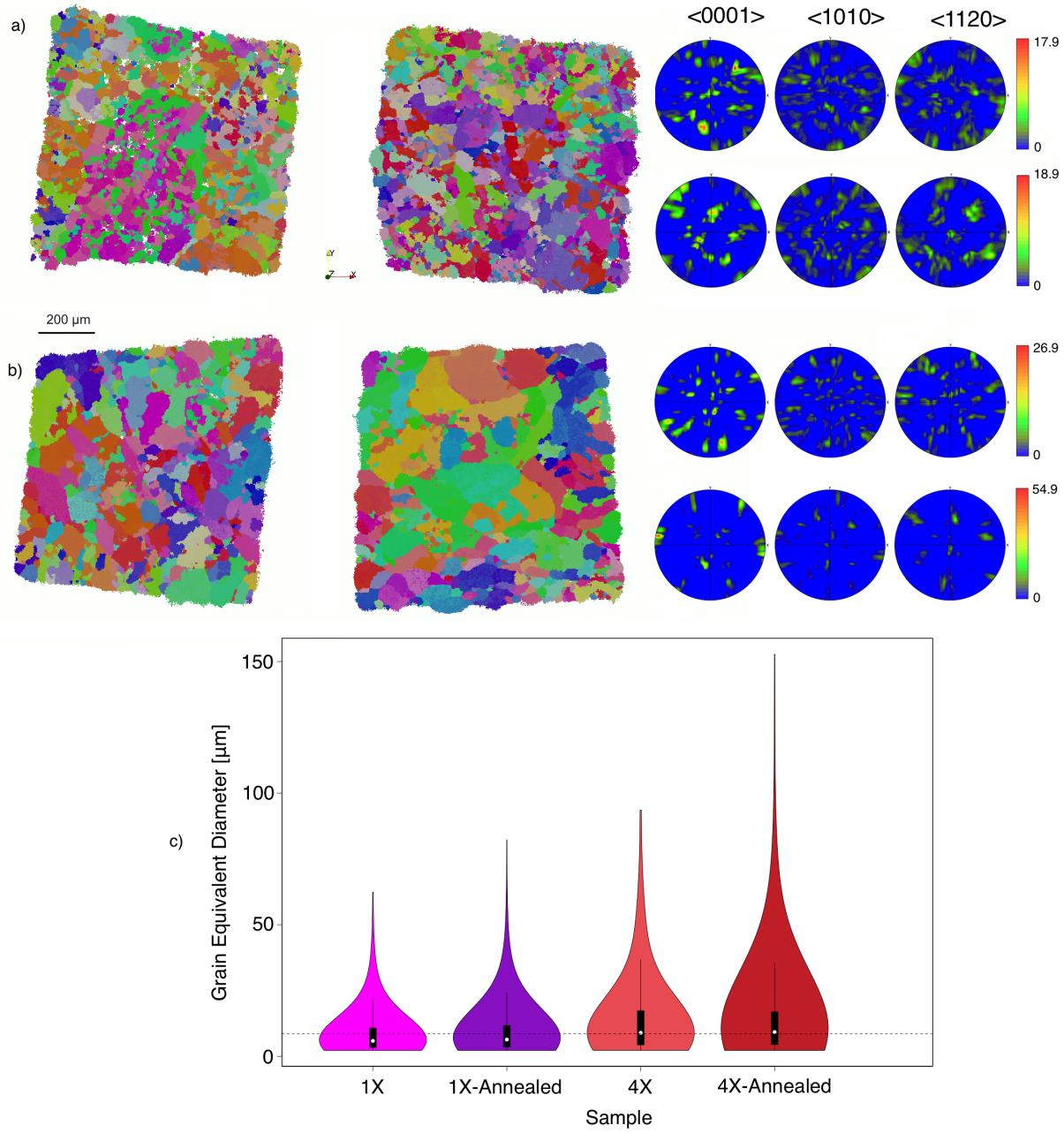

Figure 4.8: Comparison of different processing and post-processing states. a) 1X sample IPF colored orientation maps and pole figures, b) 4X sample IPF colored orientation maps and pole figures, c) Grain size distributions for all 4 states. For both a. and b. the as-built state orientation map is on the left and annealed map is on the right, and the pole figure on the top belongs to the as-built state and the one on the bottom belongs to the annealed state.

Another significant result of the nf-HEDM measurements is the ability to extract prior beta grains through the shared diffraction peaks between alpha and beta phases, as if to reconstruct the

high temperature beta phase from the diffraction of the alpha phase grains, hence "pseudo-data" instead of using a flood-fill-based technique to reconstruct the prior beta grains shown by Wielewski et al. [115]. When the two crystal phases are related by the BOR, explained in detail in Chapter 2.3, the diffraction peaks overlap which is visually seen by comparing the <110> pole figure of the bcc phase with the <0001> pole figure of the hcp phase, Fig. 2.13. If the projected intensity distribution of these two poles are similar, it indicates that variant selection does not occur during transformation, which has been shown as the case for AM Ti-6Al-4V by multiple studies [80, 82]. As one of the results of the preliminary SEM characterization was that the high power low velocity 4X setting increased the amount of retained beta fraction up to 10 % in the solidified part, we performed the forward modeling reconstruction by searching the orientations in the cubic fundamental zone and fitting the voxels for the bcc structure with the experimental data in order to see if the 10 % beta phase was reconstructable. In fitting the prior beta structure, the first step was identifying if the raw data (which is primarily the diffraction peaks of the hcp phase as at least 90 % of the material is constituted by alpha) contained shared peaks between the two phases, i.e. if there existed an orientation relationship between the transformed alpha and the prior beta phases that would result in shared diffraction patterns because of aligned crystallographic planes. This can be checked by either simulating the diffraction pattern of two phases, or using far-field HEDM diffraction data and checking the existence of overlapped Debye-Scherrer rings. After the Burgers orientation relationship, hence the presence of shared peaks was shown, the fundamental orientation space (from which the experiment is simulated) was changed from hexagonal fundamental zone to the cubic fundamental zone. Lastly, the lattice parameters and the unit cell atomic locations of the titanium alpha phase were changed into the beta phase, and the full raw data was used to fit the bcc phase. The results were surprising as the overlapped diffraction peaks of the bcc and hcp provided good enough confidence in fitting the prior beta phase with Q_{max}=6, resulting in well defined beta grain shapes and orientation distributions, shown in Fig. 4.9. Furthermore, texture investigation of the reconstructed prior beta phase revealed the existence of strong texture as expected from AM materials, with the difference of being slightly tilted off the expected <100> fiber at the top of the built, similar to the results of Antonysamy et al. [82]. In order to make sure the reconstructed prior beta grains were realistic and not a result of a systematic error, one prior beta map is back reconstructed by Chasen Ranger using his flood-fill based clustering back reconstruction algorithm [116], and a

significant agreement is observed between the back reconstructed and HEDM reconstructed maps for both the grain shapes and crystallographic orientations, Fig. 4.9. The lack of variant selection is hypothesized to provide statistically enough overlapped peaks, which in return results in a good fit confidence as there are is a larger number of possible orientations in the beta to alpha transformation, however a detailed study on the phase peak separation through phase diffraction simulations is suggested as future work for a detailed investigation.

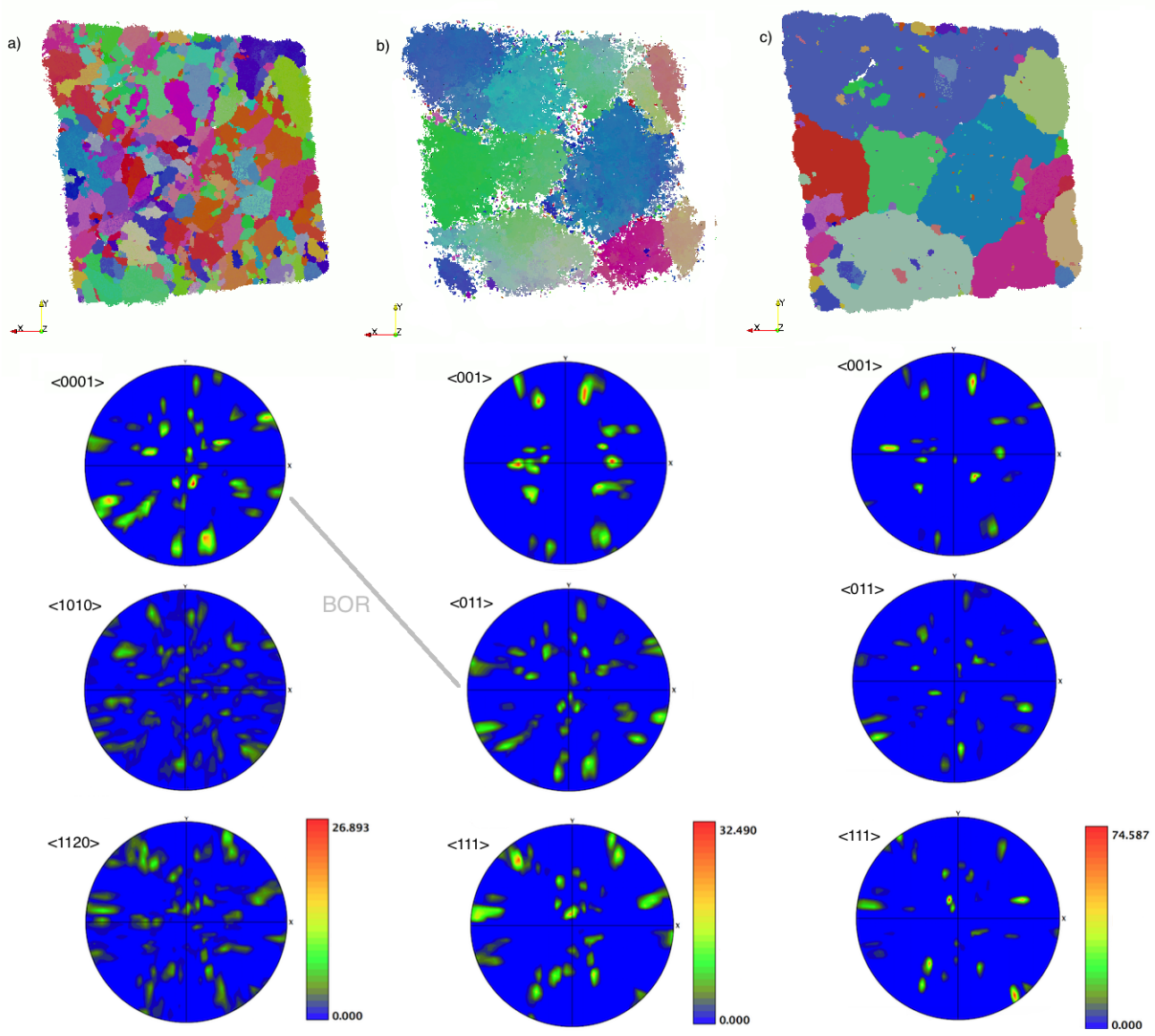

Figure 4.9: 4X sample top layer orientation maps and corresponding pole figures of a) Alpha phase nf-HEDM reconstruction, b) Prior beta phase nf-HEDM reconstruction, c) Prior beta phase flood-fill clustering back reconstruction. BOR relationship is seen by the overlapped poles in the <110> bcc and <0001> hcp pole figures. A significant agreement is observed between the back reconstructed and HEDM reconstructed maps for both the grain shapes and crystallographic orientations.

4.2 Tensile Property Measurement

4.2.1 Introduction

Ti-6Al-4V, one of the most popular titanium alloys used in direct metal AM, has been shown to hold highly heterogeneous characteristics when produced by EBM. As mentioned in Chapter 2.5.2, the thermal gradient accompanying this manufacturing process directly affects the cooling rate of the melted powder, hence the resulting microstructure and the mechanical properties. This section presents an extensive set of tensile property measurements as to bridge the spatial microstructural heterogeneity with the macroscopic properties. Tensile samples are extracted from different build height locations as both the literature and our HEDM characterization results showed microstructural heterogeneity in relation to the build height. Mechanical property measurements are coupled with optical microscopy micrographs in an attempt to link mechanical behavior with the microstructure. In addition to tensile tests, material hardening parameters are extracted from the full stress-strain curves to be utilized in constitutive and micromechanical modeling.

4.2.2 Material and methods: Electron beam melted Ti-6Al-4V and parameter optimization routine

The EBM Ti-6Al-4V materials of this study were built on an Arcam S12 machine at Carnegie Mellon University, using a virgin batch of standard pre-alloyed Arcam AB Ti-6Al-4V (Grade 5) powder, with supplier reported typical chemical composition of 6 % Al, 4 % V, 0.03 % C, 0.1 % Fe, 0.15 % O, 0.01 % N, 0.003 % H and Ti to balance, and with nominal powder size distribution of 45 - 100 microns. It should be noted that these feedstock specifications are given by the supplier, and no additional chemical composition measurements are performed on the powder or the printed parts. In order to keep the process parameter space consistent with the advanced characterization study samples, Arcam beam speed function of 36 is chosen, which should result in a nominal melt pool area of 0.04-0.06 mm^2 [114]. As discussed previously, speed function is a standard build theme for Arcam, for which the beam parameters of power and velocity are controlled according to a manufacturer developed algorithm in order to fabricate fully dense parts with microstructural consistency, which makes the specific values of beam speed and beam current unknown throughout the build as the build theme varies them constantly. The built parts consisted 2 big blocks of size 150 mm x 65 mm x 60 mm for 60 mm is the build height, and two small blocks of 80 mm x 15

mm x 100 mm for 100 mm is the build height, which are fabricated with the nominal hatch spacing, layer thickness and build plate temperature of 200 μm, 70 μm, and 750 °C respectively. Only one of the big blocks was used for this thesis work, while rest of the built samples are planned for future studies. The layout, which is shown in the experimental workflow in Fig. 4.10, took total of 38 hours to build.

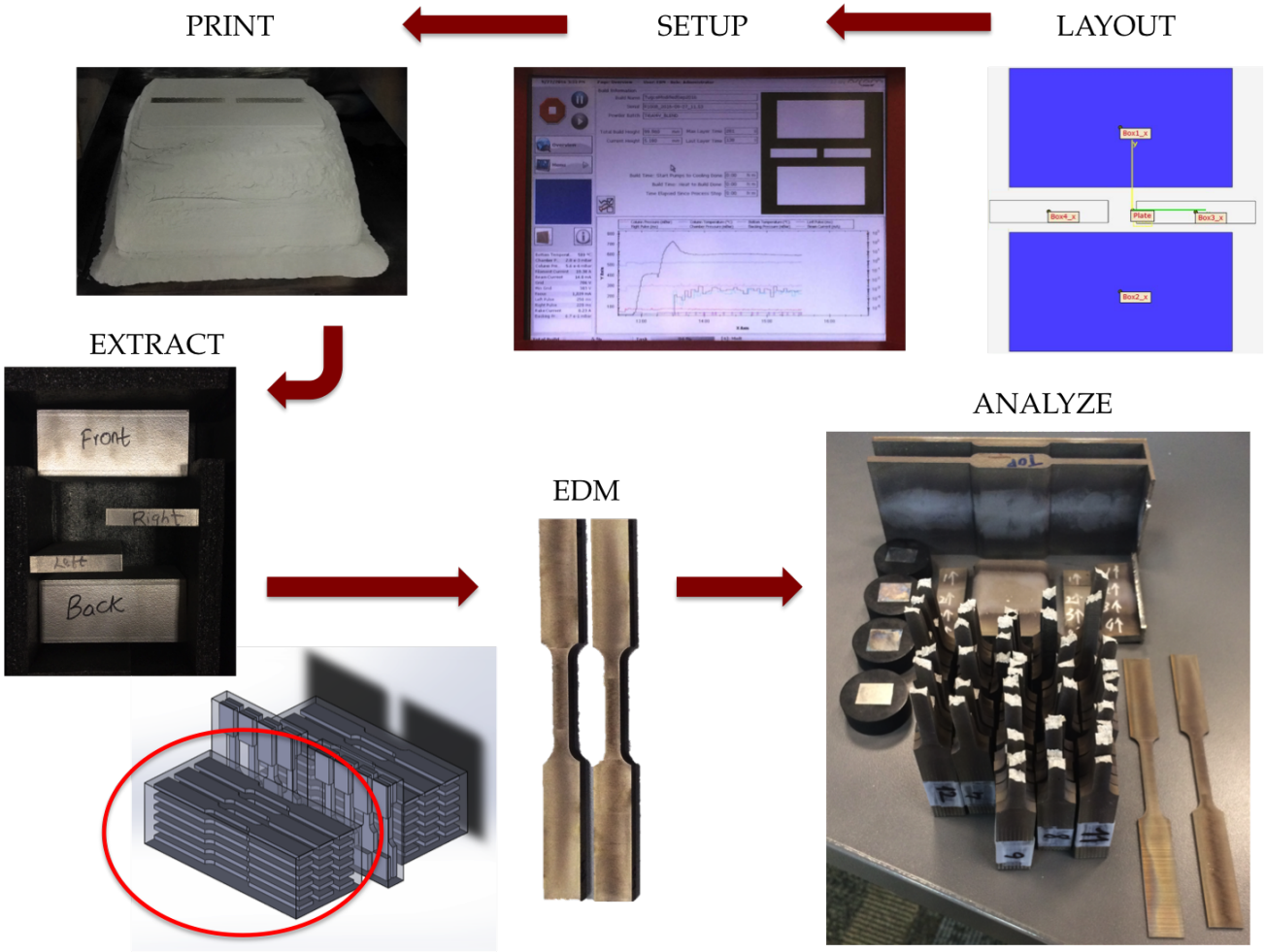

Figure 4.10: Summary of the experimental workflow

After the layout design, machine setup, building and part extraction steps, the front block was cut with electrical discharge machine (EDM) to extract horizontal tensile specimens of ASTM E8/E8M subsize specimen standard, which is described in Table 4.3 and illustrated in Fig. 4.11. EDM was chosen to eliminate the surface effects on properties. To verify repeatability, 3 samples are extracted from each different build height location. As the thickness of the tensile specimens is 4 mm, in theory we should have been able to cut total of 15 horizontal samples stacked along the

Table 4.3: ASTM E8 standards for sheet type subsize specimen

Dimensions	Subsize Specimen, mm [in.]
Gauge length	25 mm [1.00 in.]
Width	6 mm [0.25 in.]
Radius of fillet	6 mm [0.25 in.]
Overall length	139.5 mm [5.5 in.]
Length of reduced section	32 mm [1.25 in.]
Length of grip section	50 mm [2 in.]
Width of grip section	18 mm [0.75 in.]
Thickness	2.54 mm [0.1 in.]

60 mm tall build. However, as the first few milimeters of the build are not yet leveled with proper powder spreading, the end part was only 56 mm tall, from which we could machine out a total of 13x3=39 samples. An MTS 880 machine was used to perform the room temperature uniaxial tensile tests, and the elongation was measured with an MTS dynamic extensometer of 1 inch length. The displacement speed was chosen as 0.004 mm/s, so that the strain rate at the reduced section of the tensile specimen would roughly be 0.0001 s^{-1}.

Parameter optimization routine

In investigating the microstructure-property relationship of titanium alloys, computational methods of constitutive and/or microstructure based micromechanical modeling is an important step. For either of these cases, the models need to be calibrated with experimental data for material specific parameters such as elastic constants to model the elastic regime, or hardening parameters to model the plastic regime. As one of the purposes of this thesis work is to create a computational framework for microstructure/property investigation of additively fabricated titanium alloys, the collected tensile data is used to extract sets of location specific Voce hardening parameters with the intention of creating a parameter database that would inform micromechanical studies in the future, such as the one presented in Chapter VI.

When materials go under plastic deformation, they usually experience work and/or latent hardening, which denotes the rate of change in the critical resolved shear stress (CRSS) of a primary slip system for the former, or the change in CRSS of a secondary slip system for the latter. The CRSS evolution is described by hardening laws, such as the empirical Voce hardening model [95] which is considered in this work. Titanium, being a rate and temperature sensitive material, exhibits

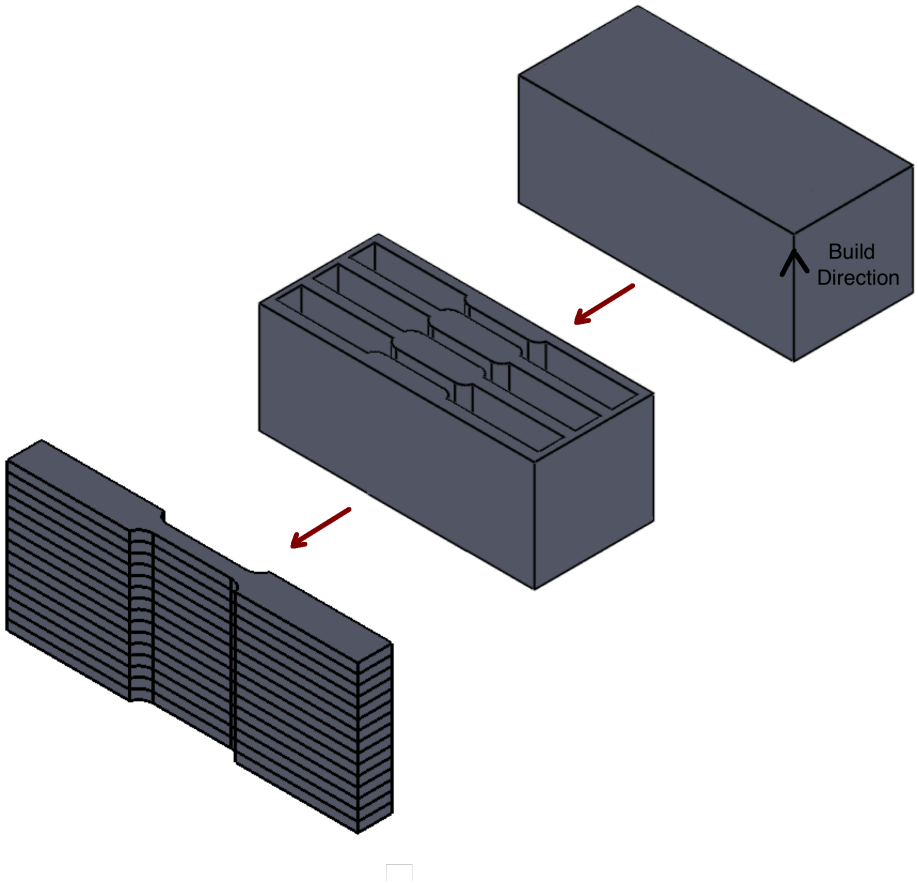

Figure 4.11: Illustration of tensile specimen preparation. Three sets of tensile specimen stacks are contoured out of the solid block for ensuring repeatibility, and each stack is machined into total of 13, 4 mm thick horizontal tensile specimens while the remnant of the block is used for microstructure characterization.

different strain and latent hardening behavior at different testing conditions and microstructural configurations, which is discussed in Chapter 2.4, so using an empirical model without any temperature or strain rate sensitive terms can only represent parameters from a single stress-strain dataset. For this work, a modified version of the Voce [95] hardening model with only self-hardening (no latent hardening) is chosen for its simplicity and ease of calibration. Modified Voce hardening is characterized by an evolution of the threshold stress with accumulated shear strain in the form of

$$\hat{\tau}^S = \tau_0^S + (\tau_1^S + \theta_1^S \Gamma)(1 - exp(-\Gamma|\frac{\theta_0^S}{\tau_1^S}|)) \tag{4.1}$$

giving 4 parameters for each slip system in each individual phase, where τ_0^S is the initial critical resolved shear stress (CRSS), τ_1^S is the initial hardening rate, θ_0^S is the asymptotic hardening rate and θ_1^S is the back-extrapolated CRSS.

For calibrating the mechanical behavior simulations, specifically the viscoplastic self-consistent (VPSC) model, a multi-parameter optimization algorithm was implemented in Matlab by Gockel [14] and Mandal [117] in order to match the simulated response with the experimental measurements. The optimization is based on a non-linear least-squares formulation, to iteratively fit the experimental data by minimizing the summed square of the difference between the measured value and the fitted value for each strain increment. The degree of the fit is quantified by a mean error percentage and mean root mean square error (RMSE). Because the optimization requires iterative comparison of the fit parameter and the measured stress until a convergence criteria is satisfied and the change in parameter no longer improves the fit, and we have total of 39 individual experiments to fit to find a set of optimized Voce hardening parameters of a two phase material, the mean field modeling technique VPSC, which is described in Chapter 3.1, was chosen for its inherent computation speed. An important consideration in extracting hardening parameters is the extent of experimental data to use, i.e. true stress-strain vs. engineering stress-strain. For this study (room temperature uniaxial tensile tests of 0.0001/s strain rate), as a first order approximation additively manufactured Ti-6Al-4V is assumed have little difference between engineering and true stress, and full engineering stress-strain is utilized in extracting the parameters. However, it is acknowledged that a future work is necessary on using true stress-strain part (up to ultimate tensile stress) of the experimental data in extracting the hardening behavior.

4.2.3 Results and discussion

Similar to the HEDM measurement results, the mechanical properties are predicted to vary along the build height of powder bed based electron beam melting Ti-6Al-4V parts. Before analyzing the tensile data, finding decreased yield and tensile strength and increased elongation was hypothesized in relation to build direction due to demonstrated larger width alpha platelets at the top of the build [16, 17]. However, both the first order comparative analysis of the averaged UTS and YS values in relation to build height, Fig. 4.12 and the second order statistical analysis of all the measured data through analysis of variance (ANOVA) method presented in Appendix B revealed an unexpected outcome.

To the first order approximation of the tensile data analysis, the scattering of the behavior between the 3 samples from the same build height was assumed to be within the natural scatter ex-

Table 4.4: Average tensile properties of different build locations

Distance from Top [mm]	Sample # From Bottom	Average UTS [MPa]	Average Yield [MPa]	Average Elongation [%]	Average Modulus [GPa]
50	1	883.79	780	12.1	111.4
46	2	894.90	786	15.05	114.05
42	3	881.79	771	14.33	114.27
38	4	943.52	829	14.19	115.38
34	5	892.67	779	14.38	116.65
30	6	909.36	794	14.62	114.93
26	7	898.65	796	14.38	114.85
22	8	899.25	801	13.54	113.35
18	9	939.71	837	14.9	113.1
14	10	951.93	851	13.89	113.75
10	11	929.33	826	13.2	113.79
6	12	939.50	836	14.2	111.94
2	13	991.00	884	12.68	119.06
Average		919.65 ± 72	813 ± 71	13.96 ± 2	114.37 ± 4

pectations of tensile tests, so that the averaged measured values could be compared and reported as in Table 4.4. In doing so, a weak trend of increased yield and tensile strengths with increased build height was observed, Fig. 4.12, with a trendline, i.e. linear regression fit with gradual slopes for the YS and UTS averages respectively. The linear regression is chosen to statistically test the significance to the first order approximation, in this case testing if the change in the build height has a significant effect on the measured tensile properties, and slight incline in the regression line is interpreted as a weak trend of increased YS and UTS along the build height. In comparing the mean values of 3 samples per location, the modulus and elongation values are found to be insensitive to the build height.

The unexpected results of slightly increased YS and UTS with build height is investigated further by OM micrographs taken from the bottom, middle and top of the build, depicted in Fig. 4.13. Similar to Antonysamy's [82] and Tan's [84] observations, an equiaxed prior beta morphology region was found at the bottom of the build with coarser columnar beta at the top. The prior beta size can be a factor in slightly increased strength with build height, as the beta grain size dependence is explained by a direct relationship of decreased tensile properties with decreased beta grain size with a theory that proposes short grain boundary slip length due to small beta grain sizes, causing reduced stress concentrations, higher ductility and lower tensile strength [2]. While the relative effect of change in prior beta morphology remains inexplorable with the tensile property measurements as the total equiaxed+transition region covers only a small part of the build, which falls outside of the tensile specimen locations, it is a great opportunity to combine computational mechanical deformation modeling efforts with experimental tensile measurements. The effect of prior beta morphology on the mechanical response, which was not captured with the tensile tests, is investigated with the

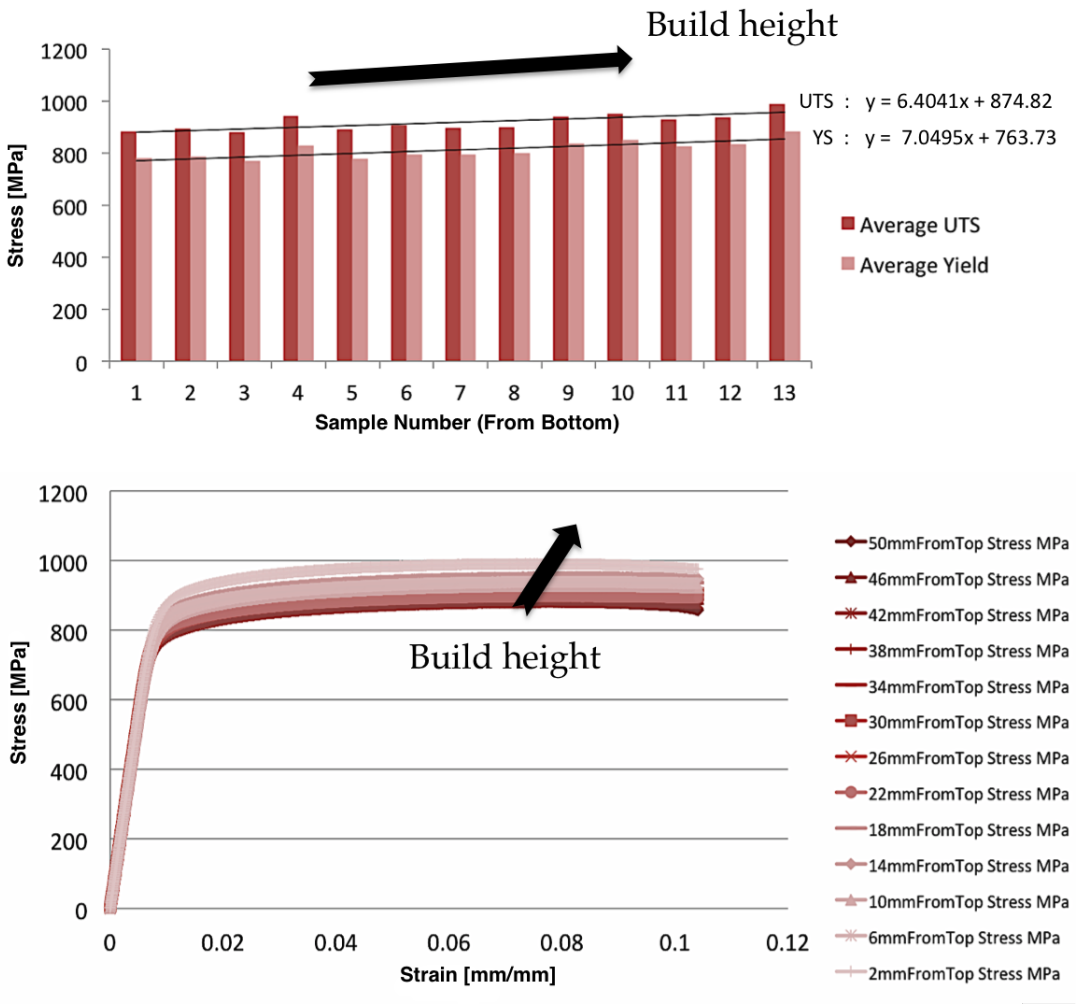

Figure 4.12: Average YS and UTS values in relation to build height at the top, and average stress-strain curves for all 13 height locations on the bottom. A weak correlation is observed between build height and increased strength.

FFT based modeling study in Chapter VI.

In addition to the low magnification (20x) OM micrographs that were collected for prior beta analysis, high magnification (50x) OM images were also taken for extracting alpha lath width statistics from locations of roughly 6 mm, 19 mm, 32 mm and 45 mm from the top, Fig. 4.13. The alpha lath widths were calculated manually by measuring 30 random laths per image, and a trend of coarsening was observed from top to bottom. As shown in Fig. 4.13, the average alpha lath sizes were measured as 1.198, 1.420, 1.498 and 1.614 μm from top to the bottom, with corresponding standard deviations of 0.13, 0.16, 0.19 and 0.14 respectively. It is important to note that the manual quantification method depends on subjective judgement, and while the absolute measured values may vary between operators, the trend should persist as the measured variation in lath spacings is shown to

dominate the standard deviation. Opposite of the discussed possibility of the prior beta grain size dependence of the yield stress, alpha lath width is shown to have an inverse grain size dependence, where decreased alpha lath size should increase the yield stress [2]. Observed finer grains at the top of the build can then be another factor in slightly increased strength with build height.

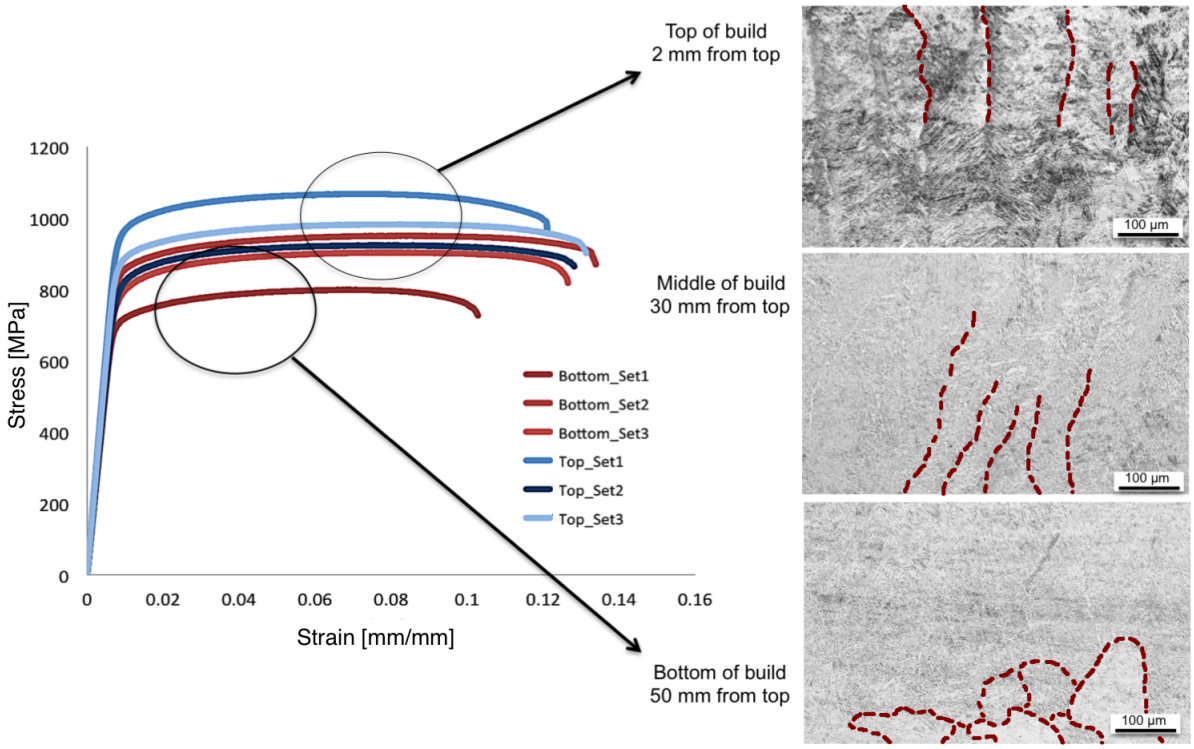

Figure 4.13: Stress-strain curves for all three samples from the bottommost and topmost regions, coupled with low magnification OM micrographs showing equiaxed prior beta morphology at the bottom of the build with coarser columnar beta at the top.

In the first order approximation analysis, average of the repeated tensile test values were taken as the properties that represent the corresponding build height. Using the average of three samples in linear regression is good to first approximation, however it homogenizes the variation in differences of means of repeated measurements, which in turn can result in unrepresentative conclusions if the repeated measurements are highly scattered. In partitioning the variation into parts due to variation within and among repeated measurements, the analysis of variance (ANOVA) method, a form of statistical hypothesis testing, is a commonly used technique [131]. The basic idea behind ANOVA is to test whether or not the means of the individual observations are the same for different groups; in our case if means of repeated 3 measurements per build height are the same for different location. For our 13 groups of 3 observation per group, a one-way between subjects ANOVA

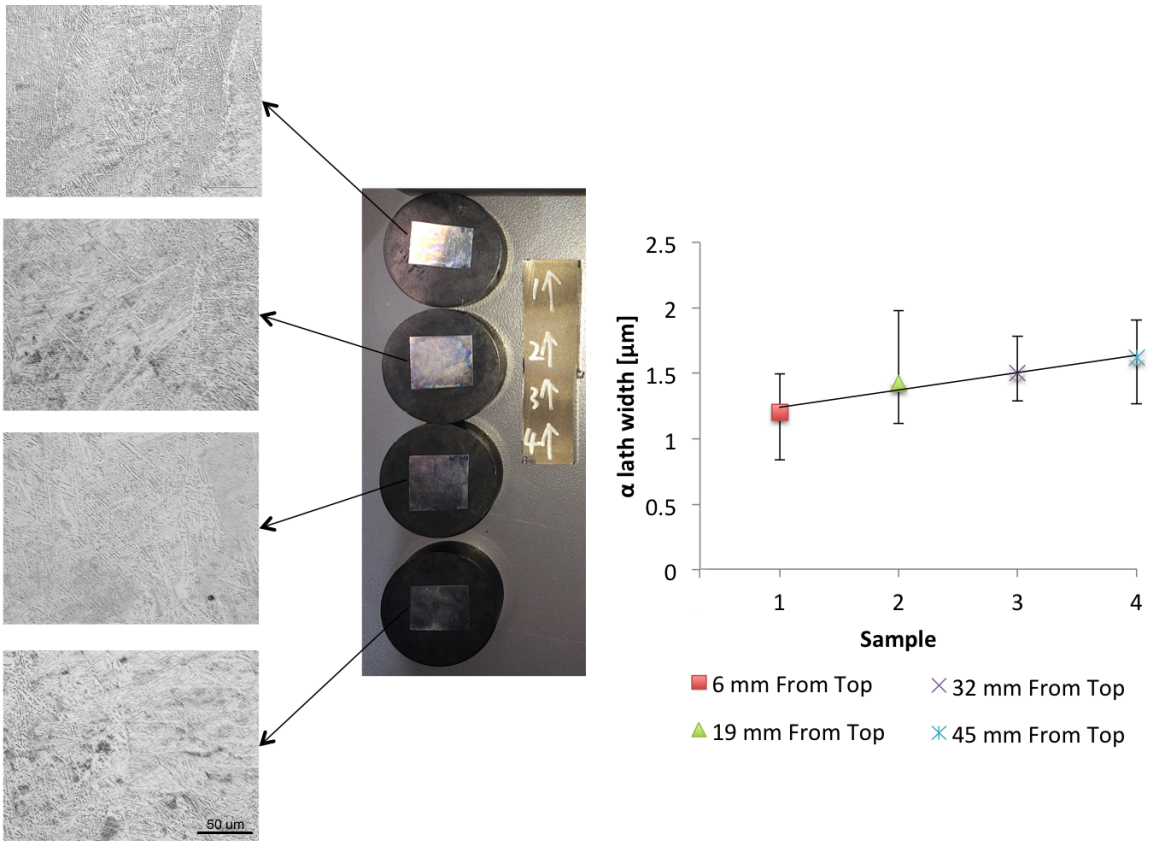

Figure 4.14: High magnification OM micrographs taken from roughly 6 mm, 19 mm, 32 mm and 45 mm from the top of the build, indicated on the bulk sample by locations 1, 2, 3 and 4 respectively, and measured average alpha lath widths.

was conducted to compare the effect of build height on yield stress, ultimate tensile stress, elastic modulus and elongation, using the statistical analysis software SPSS. For among-group degrees of freedom (DOF) of 12, within group DOF of 26, and significance criterion $p < 0.05$, meaning that if the calculated p value is less than 0.05, there is significant effect of build height on a property; elastic modulus [$F(12,26) = 1.235$, $p = 0.313$], elongation [$F(12,26) = 1.239$, $p = 0.310$] and yield stress [$F(12,26) = 1.810$, $p = 0.100$] do not appear to be significantly affected by build height, whereas the ultimate tensile stress [$F(12,26) = 2.127$, $p = 0.052$] approaches prognostic significance. Since the build height is found to affect the UTS but not the YS, the microstructure-property coupling conclusion of smaller alpha size-higher strength due grain size dependence cannot be the sole factor affecting mechanical behavior, which is investigated in the micromechanical modeling study in Chapter VI. The SPSS report with full ANOVA results are presented in Appendix B. Conducted the ANOVA test revealed that similar to work by Hrabe [76], there is no significant change in mechanical properties along the build height, with the exception of ultimate tensile stress being at the brink

of statistical significance.

Experimental and VPSC simulated Ti-6Al-4V stress-strain curve comparison

As previously mentioned, one of the purposes of this thesis work is to create a computational framework for microstructure/property investigation of additively fabricated titanium alloys. For this reason, the collected tensile data was used to calibrate the dual phase VPSC simulations, by iteratively fitting the measured stress-strain curve to simulated data in order to extract hardening parameters. The hardening model of choice, modified Voce hardening requires the optimization of only four parameters as discussed in Chapter 4.2.2. However, as the success of the least-square algorithm highly depends on the initial parameter guess, and the algorithm does not guarantee a unique solution, it is crucial to start with a close-enough set of initial parameters, and check the simulation results of the new parameter set against the real data [14]. For titanium is a dual phase material, parameter optimization is performed on both phases simultaneously by assigning the phase fractions and initial parameter guesses. The slip induced plastic deformation of alpha and beta phases, and the individual slip systems with their relative CRSS ratios are discussed in depth in Chapter 2.4. For this experimental and VPSC simulated Ti-6Al-4V stress-strain curve comparison study, a ratio parameter ratio of 1:0.7:3 is used for all four parameters of the hcp slip basal:prism:pyramidal<c+a> systems, while the ratio of bcc system phase is kept constant. For 96 % alpha and 4 % beta phase, total of 500 grains with random orientation was used to model the plastic deformation. The onset of

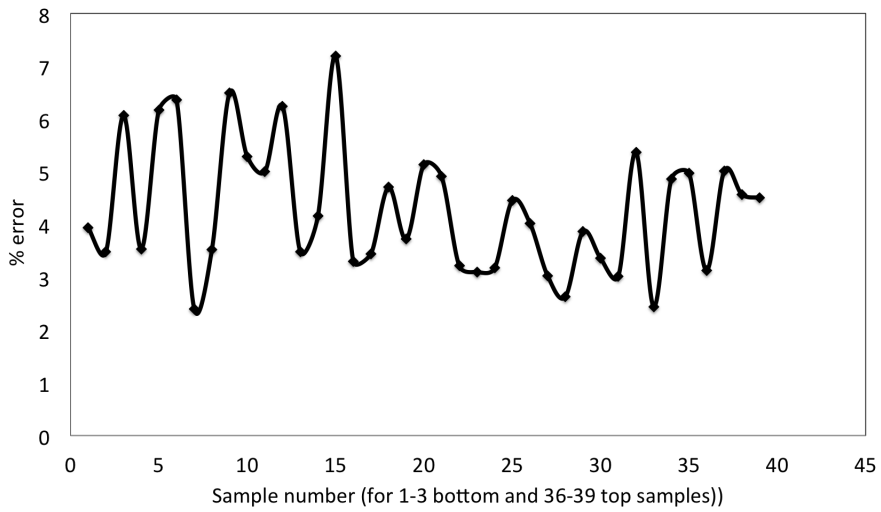

Figure 4.15: % error between the VPSC predicted stress response and the experimental data after successful completion of Voce parameter optimization.

plastic deformation is identified using a 0.2 % offset line, illustrated in Fig. 6.3. As previously mentioned, for this study additively manufactured Ti-6Al-4V is assumed have little difference between engineering and true stress; hence full engineering stress-strain curves (up-to fracture) are used in extracting the hardening parameters. Because we have a location specific data that shows a large scatter in properties, and because we could accelerate the optimization process by using the previously fit parameters as initial guess in the next step, the tensile data was used to extract optimized Voce hardening parameters. All of the experimental and VPSC simulated two phase AM Ti-6Al-4V stress-strain curves are presented in Fig. 4.16, 4.17, 4.18, in order to both show the extent of data variability, and to provide full plastic regime stress-strain curves of additively manufactured Ti, which is rarely found in literature as most of the reported data is in the form of tensile property values. Mechanical deformation modelers who seek to find raw data or fit parameters to calibrate their plasticity models such as the CPFFT or CPFEM can directly use the Voce parameters if CRSS hardening update is implemented with Voce model. The results of the VPSC parameter calibration study is provided in Table B.1. As all 39 cases were optimized with % error < 10 %, illustrated in Fig. 4.15, we could support the initial hypothesis we had formed based on the work by Gockel [14] that in extracting the location specific material hardening parameters from the tensile stress-strain curves, the Voce hardening model is can predict the behavior with less than 10 % error.

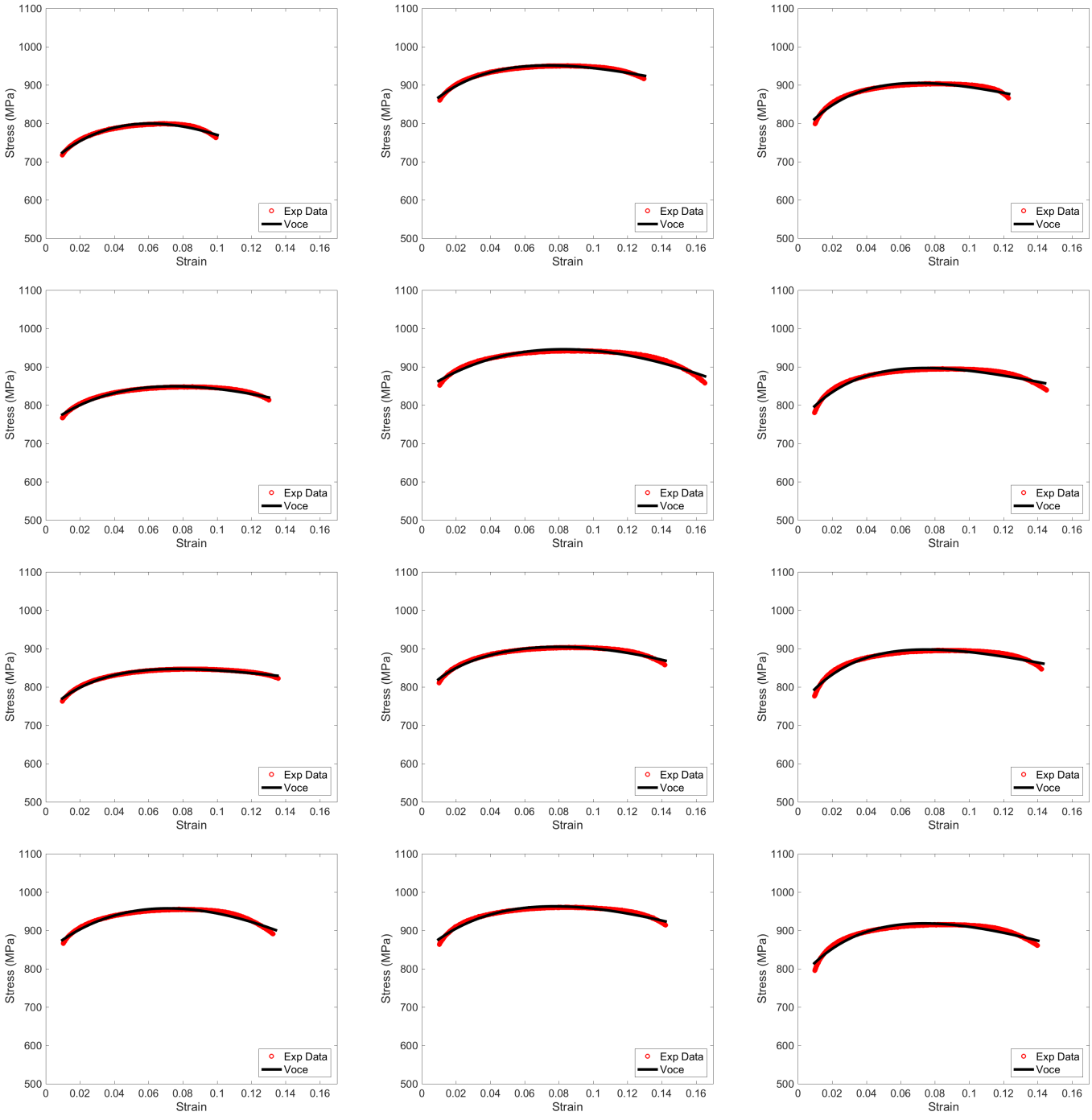

Figure 4.16: Experimental and VPSC simulated two phase AM Ti-6Al-4V stress-strain curves with strain rate $\dot{\varepsilon}$ = 0.0001/s for tensile samples cut from 50 - 38 mm below the top of the build.

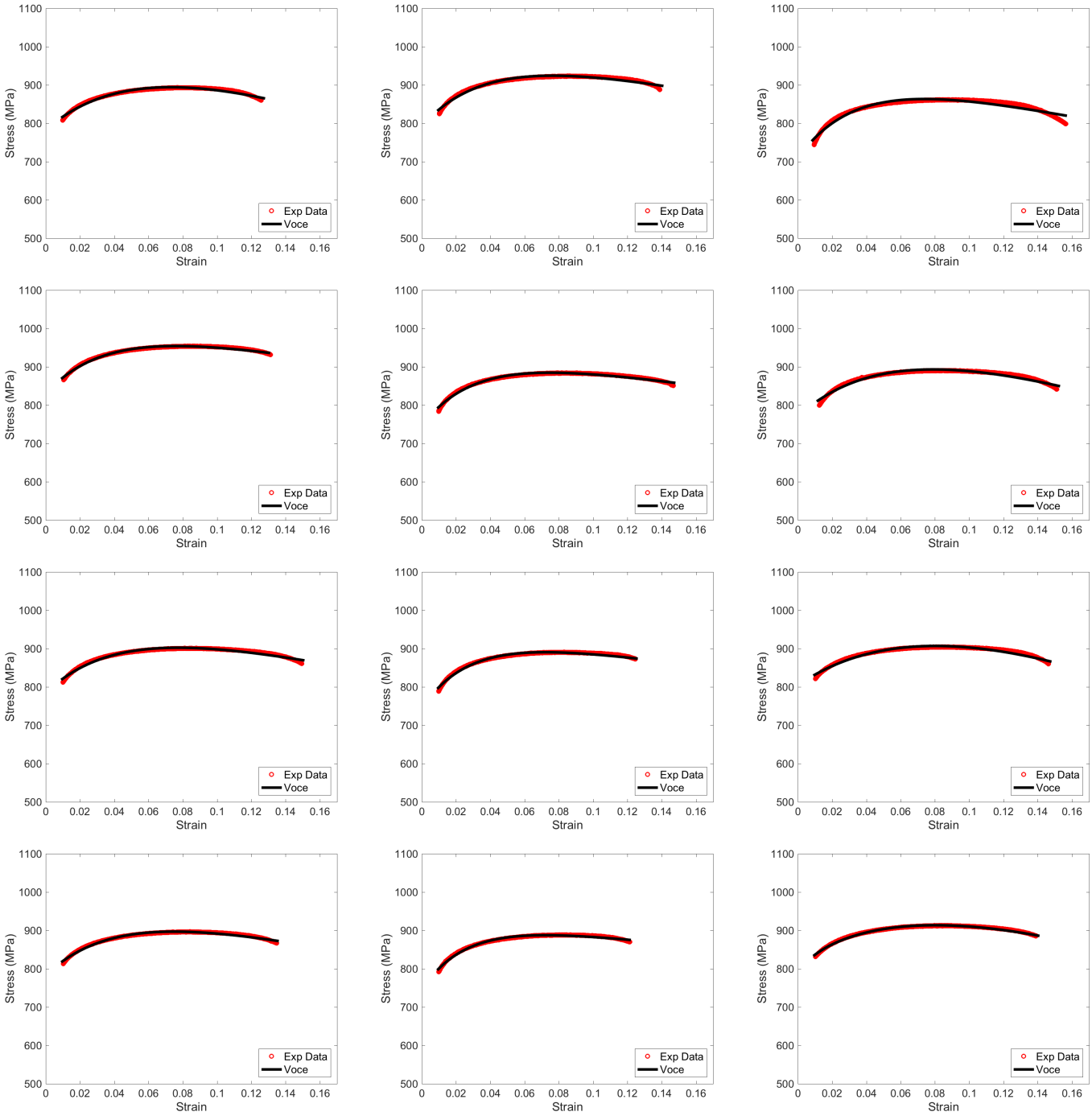

Figure 4.17: Experimental and VPSC simulated two phase AM Ti-6Al-4V stress-strain curves with strain rate $\dot{\varepsilon}$ = 0.0001/s for tensile samples cut from 38 - 22 mm below the top of the build.

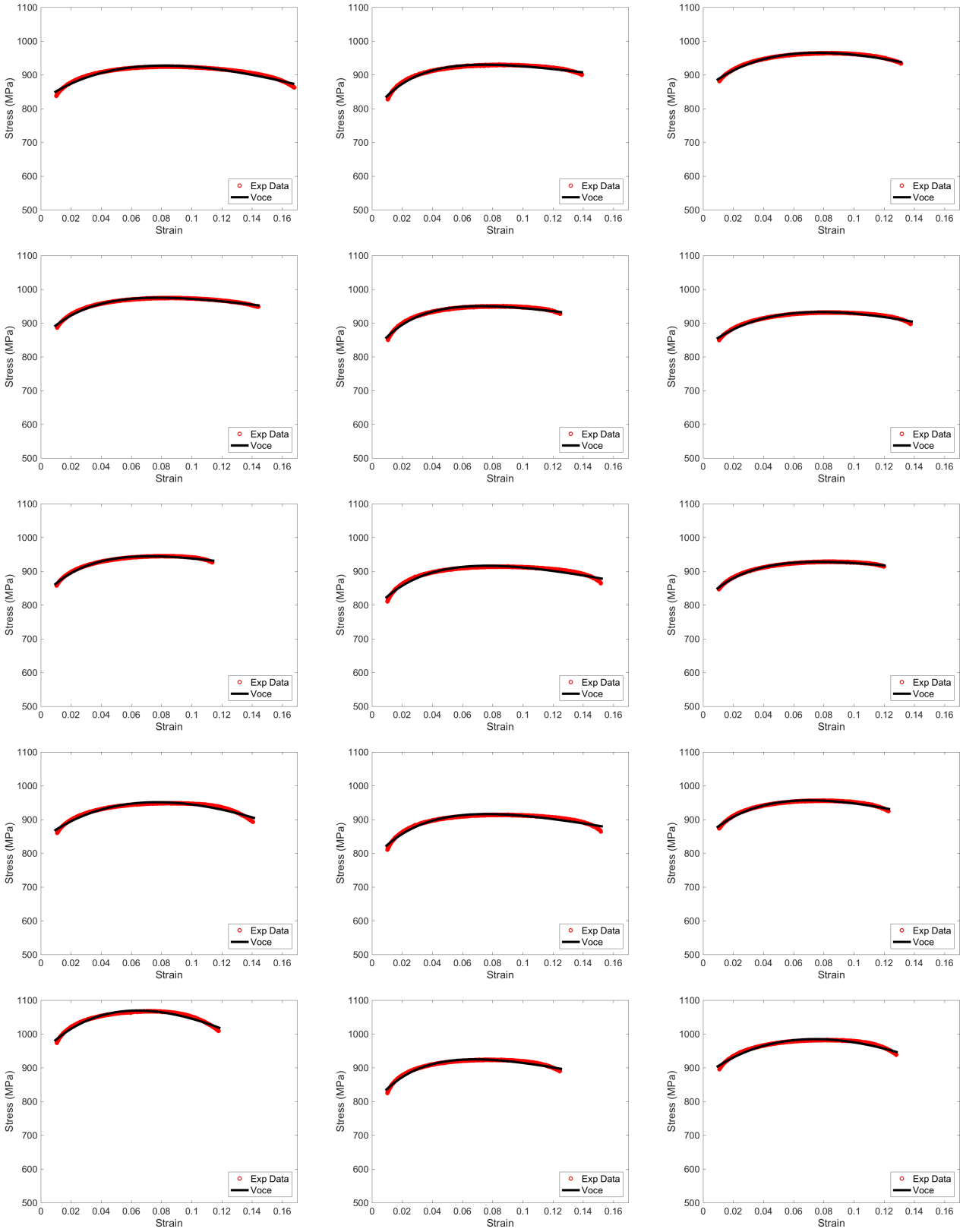

Figure 4.18: Experimental and VPSC simulated two phase AM Ti-6Al-4V stress-strain curves with strain rate $\dot{\epsilon}$ = 0.0001/s for tensile samples cut from 22 - 2 mm below the top of the build.

CHAPTER V

Domain Size Dependence of the FFT Method

This chapter presents multiple sensitivity studies for determining a minimum simulation domain size for the FFT based micro-mechanical modeling. Computational efficiency is of crucial importance in investigating the microstructure-mechanical property relationship of complex polycrystalline materials via computational tools. Simulation domain size, deformation regime, material of interest and the contrast of properties (e.g., textured vs. randomly oriented microstructure) are all hypothesized to be critical factors in determining the total computation time of both the synthetic SRVE generation and modeling steps, hence with the sensitivity analysis we present an extensive application of the FFT method as a microstructure based modeling technique on different polycrystalline material systems that are processed and generated with different techniques outside of additively fabricated titanium. The results presented in this chapter are used to determine the FFT based mechanical deformation modeling simulation size of the synthetically generated dual phase titanium structures, Chapter VI.

5.1 Sensitivity Analysis - Elastic Regime

5.1.1 Introduction

For small deformations of most polycrystalline materials, an anisotropic linear relation between the stress and strain tensors can describe the elastic response, and for larger irreversible deformations an anisotropic non-linear relation describes the plastic response. Modeling techniques such as the fast Fourier transform (FFT) based algorithm or finite element modeling (FEM) can be used to compute these relationships and predict the overall and local mechanical behavior [118]. However, especially as a result of advanced characterization techniques, the size of the data sets used in

these simulations have been growing rapidly, which makes calculations computationally expensive, which motivates an effort to define how large a volume is required in order to obtain accurate predictions of, e.g., micromechanical response. There are studies to define three dimensional representative volume elements (RVEs) and statistical volume elements (SVEs) to estimate the overall elastic material properties [119, 120], texture evolutions [121], phase transformation dynamics [122], and plastic behavior [123] of polycrystalline aggregates through smallest possible simulation domains, yet the analyses do not extend to examine the effect of grain interactions on the local level field distributions, which is especially crucial in the investigation of critical events such as fatigue crack initiation/growth studies. For instance, Stein et al. [124, 125] used the elastic FFT method to investigate the stress state in the vicinity of the microstructurally small fatigue cracks by simulating the full field anisotropic elastic response using the EBSD maps (in 2D) to instantiate the simulations. They reported that the observed cracks are located along coherent $\Sigma 3$ boundaries that are oriented favorably for slip. To further support this finding, the region around one of the identified cracks was characterized using High Energy X-ray Diffraction Microscopy (HEDM) in Argonne National Laboratory. With this characterization technique, the specimen cross sectional diameter is limited to about 1 mm, as detailed in 3.2, which meant that only a certain number of grains could be mapped. Thus, it is uncertain whether or not the characterized volume was sufficient to provide enough information for simulations, and if it was, is it possible to divide the volume into smaller simulation domains without losing stress/strain resolution for computational efficiency. This uncertainty can be concretized by posing the question, "based on the anisotropic response of the polycrystal, how many neighbor grains are required for stress-strain fields to converge in a chosen grain?", which is a variant of the question "how large of an SVE is required in order to study the behavior of a specific location in a polycrystal?". This is tested by selecting smaller and smaller volumes from the whole specimen, each of which contains the same identified crack adjacent grains. The degree of linear correlation between the compared simulations is quantified by the Pearson correlation coefficient. By taking the largest down-sampled SVE as the reference state, both voxel by voxel and mean field comparisons are performed to determine how well-converged each subset domain is to the reference volume. After the simulation size requirement is found for the specific experimental LSHR data in the elastic, viscoeplastic and elasto-viscoplastic regimes, the scope of the elastic analysis is extended to synthetically created statistically representative structures in order to study the effect of

anisotropy, deformation boundary condition, loading direction and texture on the local level elastic behavior.

5.1.2 Experimental and synthetic microstructures

Ni-based superalloy, LSHR

Superalloys have superior mechanical performance such as high strength, high oxidation, and high creep and fatigue resistance, even at elevated temperatures. LSHR, a Ni based advanced disk superalloy that has been developed by NASA researchers [126], was processed and tested at the Air Force Research Laboratory of Wright-Patterson Air Force Research Laboratory for the fatigue crack initiation study [124, 125, 127]. They were manufactured via powder metallurgy, with powder particle diameters being no larger than about 55 μm. The microstructure in the middle of the gauge section was coarsened at AFRL [128] via localized heat treatment to produce a grain size of approximately 23 μm, whereas the grain size in fine region was approximately 4 μm. The specimen was cyclically loaded in tension-tension, and the test was interrupted at 37,500 cycles when small cracks were detected on the surface of the specimen. Stein et al. [124, 125] used scanning electron microscopy (SEM) to characterize the surface of the fatigued specimens, which revealed microcracks on the electropolished surface, and the region around one of the identified cracks was mapped at Argonne National Laboratory; this microstructure is used in the sensitivity analysis, Fig. 5.1.

Microstructure characterization using HEDM

The fatigued LSHR sample was characterized with nf-HEDM, and the reconstruction provided an image with 0.1 $^\circ$ orientation resolution. A total of 61 layers were scanned using a typical 4 μm increment in the z direction between layers; the reconstruction was performed using IceNine with a mesh resolution of 0.923 μm in the x and y directions Fig. 5.1. The full volume contains of order 39 million independent orientation measurements and 37,481 grains. As suggested by the variegated orientation color, the texture is random. After Stein et al. [124] performed EBSD on the same LSHR sample, the 2D surface orientation map was aligned with the HEDM reconstruction in order to label the crack neighboring grains in the 3D map, as shown in Fig. 5.2. Previously Marrow et al. [129] studied short fatigue crack nucleation via high resolution X-ray tomography and investigated the shape of the MSFC without having the crystallographic information. In another study Ludwig et

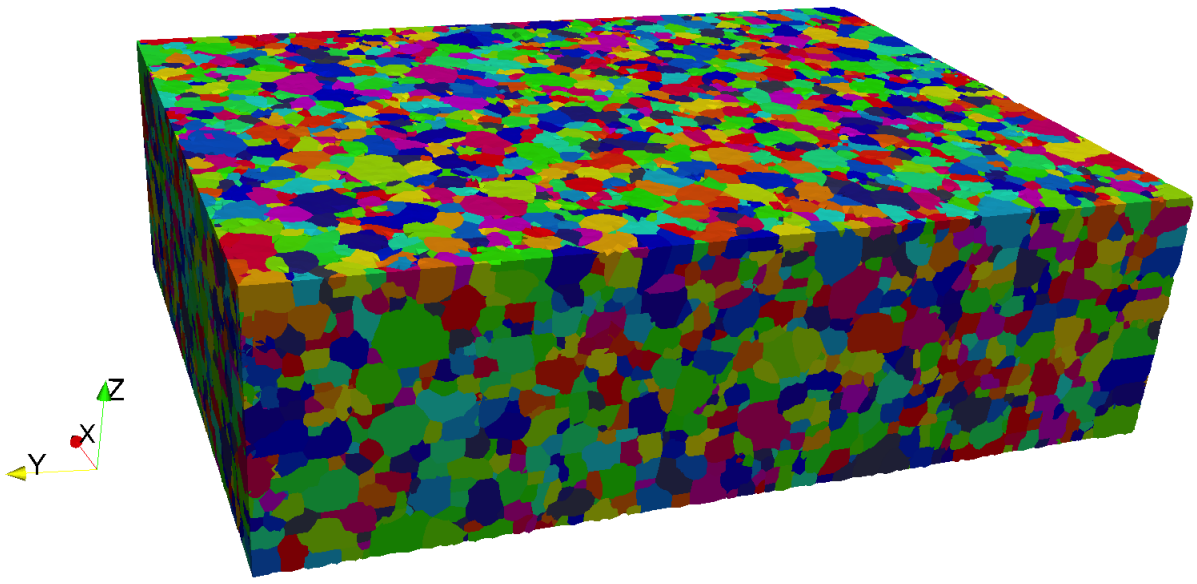

Figure 5.1: Full reconstructed volume of LSHR from nf-HEDM, with approximate dimensions 600x800x240 μm. False colors are mapped from the Rodrigues vector components specifying the orientation at each point.

al. [130] simultaneously 3D imaged a short crack and its surrounding crystallographic grains in order to investigate crack propagation. Our LSHR sample and reconstruction differs from these studies in that the existing crack is microstructurally small, i.e. on the order of the grain size, making local neighborhood sensitivity analysis a precursor for investigation of crack initiation.

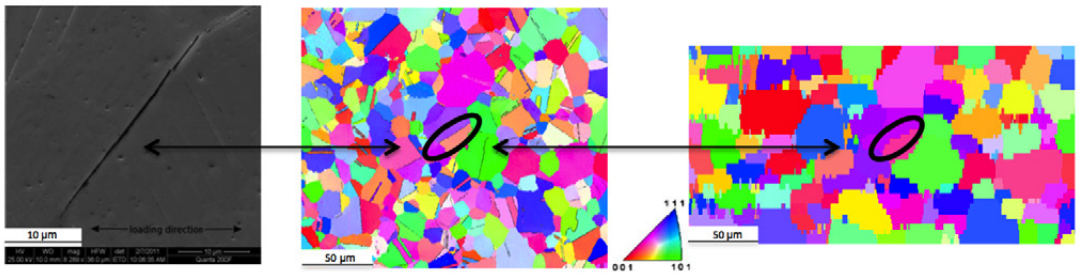

Figure 5.2: SEM image of the microcrack (rotated to match the reference frame of HEDM) on the left, EBSD map of the same region in the middle, HEDM map of the same region on the right (Coloring is based on the crystallographic plane exposed at the surface, aka inverse pole figure coloration. Spatial resolution and color scaling is different).

The near field HEDM reconstruction of the LSHR sample is used as direct input for the sensitivity study. The research question is “How many neighbor grains are required for stress-strain fields to converge in a chosen grain?". Positioning the identified crack neighbor surface grains at the center of the images, six SVEs are subdivided out of the full volume, and the largest one with the domain size of 512x512x64 is used as reference in the comparisons. Since the resolution of

HEDM is lower at the surfaces, an optimized cut plane is applied to discard poorly indexed surface voxels. To preserve the periodicity that is required in the FFT calculations, the unit cell surfaces are covered with four voxels of buffer layers in x and y directions, and the original 61 z-layers of the HEDM scan is completed to 64 layers by mirroring the bottom three layers to top in loading (z) direction in order to have 2^n z-dimension for parallel decomposition of the problem. Fig. 5.3 shows the structures used in simulations, where the identified cracked region is circled for each case, as well as the magnified crack neighbor grains.

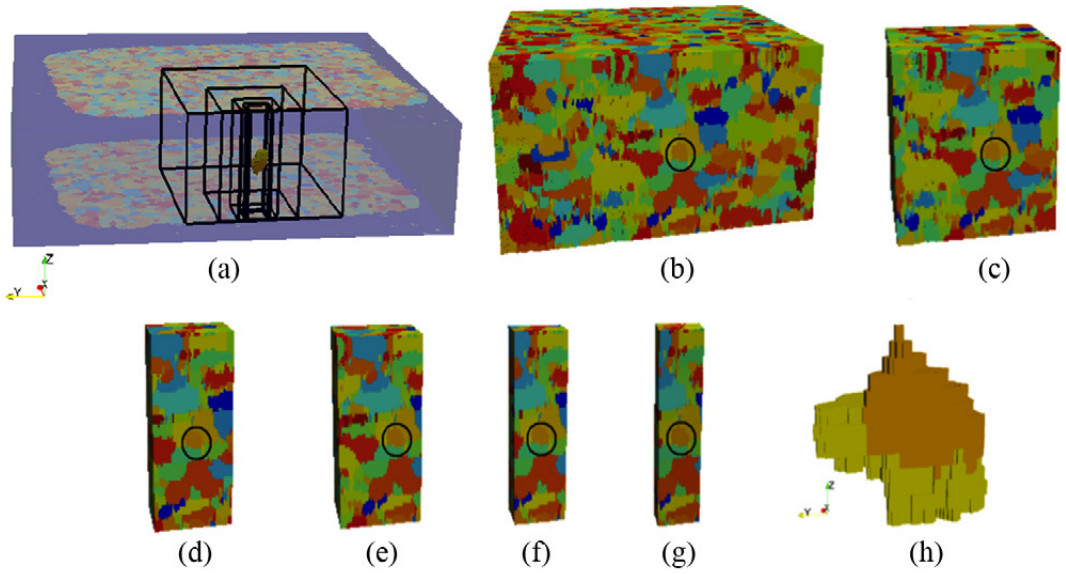

Figure 5.3: a) Full image, crack neighbor surface grains and the outline of the sub domains. SVEs with domain sizes of b) 512x512x64 c) 256x256x64 d) 128x128x64 e) 121x121x64 f) 81x81x64 g) 64x64x64 h) Crack neighbor grains. The color is based on the orientation via the Rodrigues parameters.

Synthetic structures for elastic analysis

To further investigate the convergence, statistically representative microstructures (SRMs) were reconstructed via DREAM.3D. With the intention of investigating the effect of loading condition/direction, anisotropy and texture, a single-phase equiaxed cubic structure was constructed on a 3153 voxel grid. Based on one voxel per μm and an average grain size of 20 μm, the largest domain contained 7,515 grains. Two different texture states were assigned to the SRMs: random and preferred (100) fiber texture, Fig. 5.4. Effectively, these two textures probe weak versus strong texture.

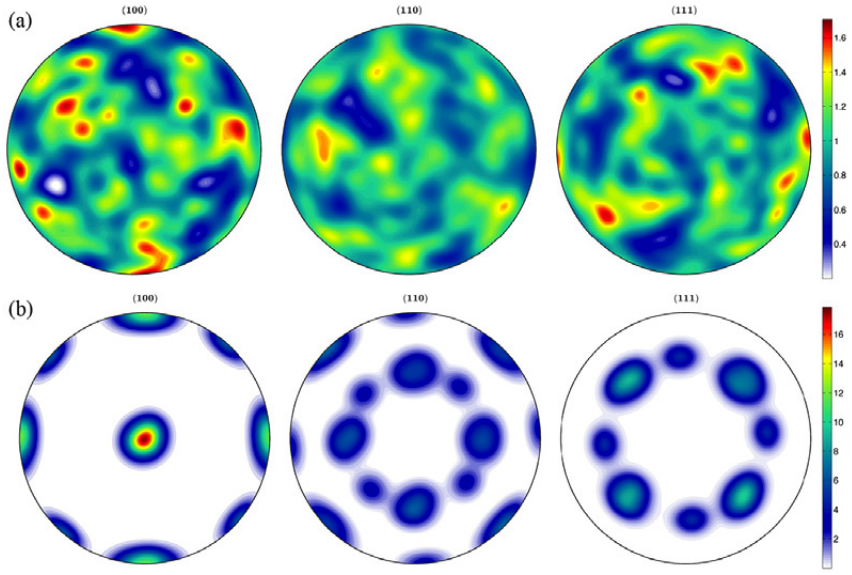

Figure 5.4: Pole Figures showing the crystallographic texture for the synthetically created microstructures: a) Random texture for loading condition/direction and anisotropy analysis; b) (100) fiber texture for analysis of the effect of preferred orientation.

5.1.3 Quantitative SVE size comparison: Pearson correlation coefficient

As mentioned previously, the interest is performing voxel by voxel and mean field comparisons between different sized simulations and determining how well-converged each subset domain is to the reference volume. For describing how closely related two measurements are, statisticians invented a quantity called correlation coefficient. Different from the linear regression methods which are usually preferred for predicting relationships, correlation is calculated between two variables to numerically express the degree of linear relationship. One of the widely used correlation coefficients, Pearson's correlation coefficient, also called Pearson's r, measures the degree of linear correlation between two independent datasets by summing the product of standard scores for all variables of two datasets, and then dividing it by the number of paired observations [131]. It is important to note that Pearson's r by itself does not measure agreement or error in between two datasets, but merely indicates the strength of linearity by taking values between -1 and 1, negative r values meaning negatively correlated, 0 meaning uncorrelated and positive r values meaning positively correlated. Pearson's correlation coeffienct is invariant to location and scale changes between variables, and very sensitive to the outliers which is usually a problem in statistical models [131]. However, in the case of simulation size sensitivity, we value the divergence in outliers as high stress-strain values are indicators of critical events as stress concentrations. Furthermore, plotting the compared points

against each other can infer agreement between two sets if the points lie along the line of equality. Hence, correlation plots combined with Pearson correlation coefficients is chosen as the quantitive approach in SVE size comparison, where a high r value ($\geqslant 0.99$) and cluster along the line of equality is taken as convergence between the compared largest domain size and the subsets of the largest volume.

5.1.4 LSHR results

The elastic stiffness components are chosen as C_{11}= 247 GPa, C_{12}=155 GPa, C_{44}=125 GPa, in line with the experimental data and LSHR mechanical property characterization report [126], giving anisotropy factor of 2.71. The strain boundary condition is chosen as $\varepsilon_1 = \varepsilon_2$= -0.00086 and ε_3 = 0.003 since it is a simulation of tension in the z direction with Poisson's ratio being 0.286. For each SVE, identical strain boundary conditions and elastic coefficients are used to simulate elastic tension. The mean values of maximum principal stress and strain for the two crack neighboring grains are shown in table 5.1. These simulation domains were all based on the experimentally measured (HEDM) volume.

Table 5.1: Number of grains per volume in each simulation domain based on the experimentally measured volume, together with the average stress and strain values for the crack neighbor grains

		512x512x64	256x256x64	128x128x64	121x121x64	81x81x64	64x64x64
	Number of Grains	11780	3114	875	738	356	257
Max Principal Strain [mm/mm]	Lower Grain	0.00273	0.00273	0.00274	0.00274	0.00273	0.00274
	Upper Grain	0.00366	0.00366	0.00367	0.00366	0.00363	0.00361
Max Principal Stress [MPa]	Lower Grain	634.771	634.797	635.927	632.460	629.447	630.690
	Upper Grain	626.559	627.102	627.836	623.704	622.299	624.948

The results presented in table 5.1 are plotted to visualize the convergence trend as a function of the number of grains included in the simulation subset domains, Fig. 5.3. As frequently noted in the literature, of the crack neighbor grains, one grain is stiffer than the other [132] so it has a higher stress but a lower strain. Fig. 5.6 shows the maximum principal stress distributions within the two grains of interest.

In agreement with the convergence trend observed with mean values, the visualization of the local stress distribution in the two grains, Fig. 5.6, also suggests good correlation. To demonstrate this quantitatively, voxel by voxel results are compared between the largest (reference) volume and

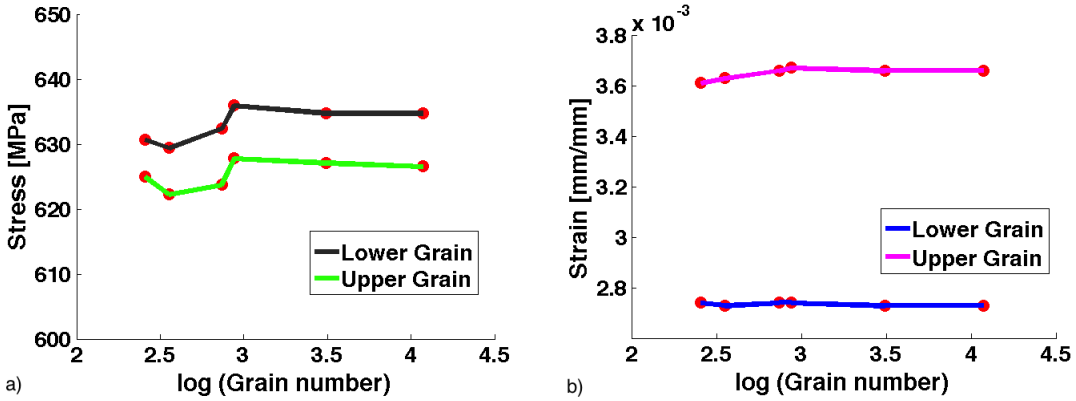

Figure 5.5: a) Average maximum principal stress within the crack neighbor grains as a function of the number of grains in the SVE; b) average max principal strain within the crack neighbor grains versus the log of number of grains in the SVE.

each of the other volumes in turn. Pearson correlation coefficients are presented for maximum principal stress of the crack neighbor grains in table 5.2

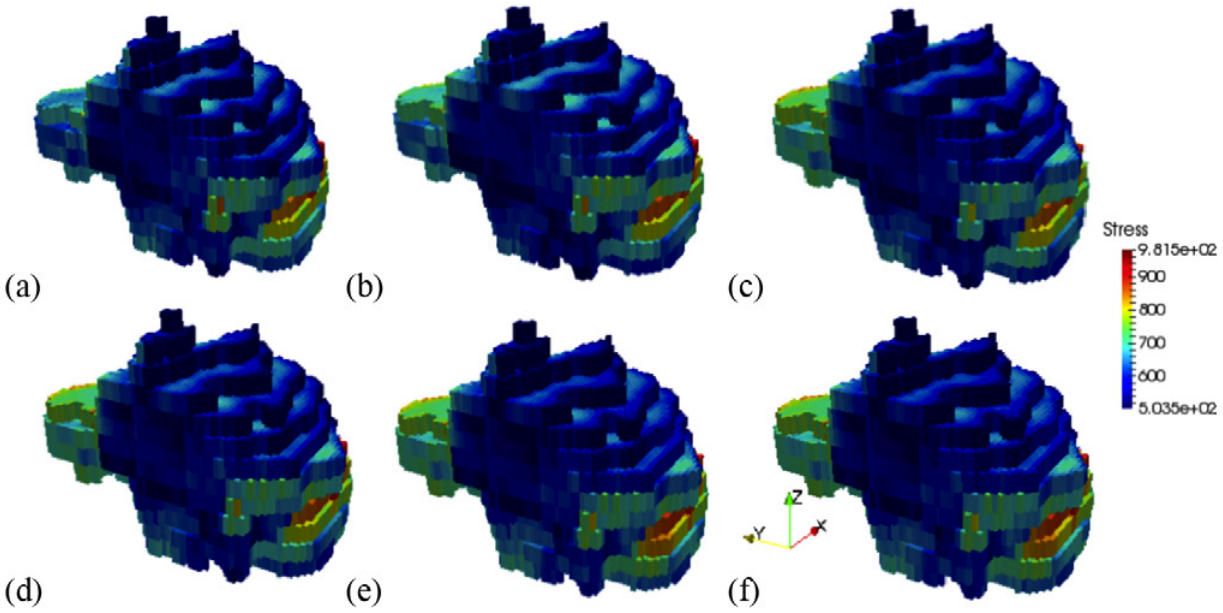

Figure 5.6: Max principal stress distributions for two neighbor grains around the identified microcrack for SVE of a) 512x512x64 b) 256x256x64 c) 128x128x64 d) 121x121x64 e) 81x81x64 f) 64x64x64. The stress values are rescaled with respect to the largest SVE for comparison.

Table 5.2: Pearson correlation coefficients for max principal stress values within the two grains neighboring the crack

	512 vs. 64	512 vs. 81	512 vs. 121	512 vs. 128	512 vs. 256
Lower Grain, Stress	0.96	0.99	0.99	0.99	0.99
Upper Grain, Stress	0.97	0.99	0.99	0.99	0.99

Quantitative voxel by voxel comparison shows that for a correlation larger than r = 0.99, 356 or more grains must be present in the simulation domain. For the LSHR specimen, the convergence trend is observed for 81x81x64 and larger grids, as depicted in the following correlation plots, Fig. 5.7. This result of the sensitivity analysis shows that for the elastic FFT calculation, stress-strain distributions are not very sensitive to the shape of the domain. It is not mandatory to use the entire sample in the simulations, and computation time can be decreased substantially by trimming smaller volumes that contain the region of interest.

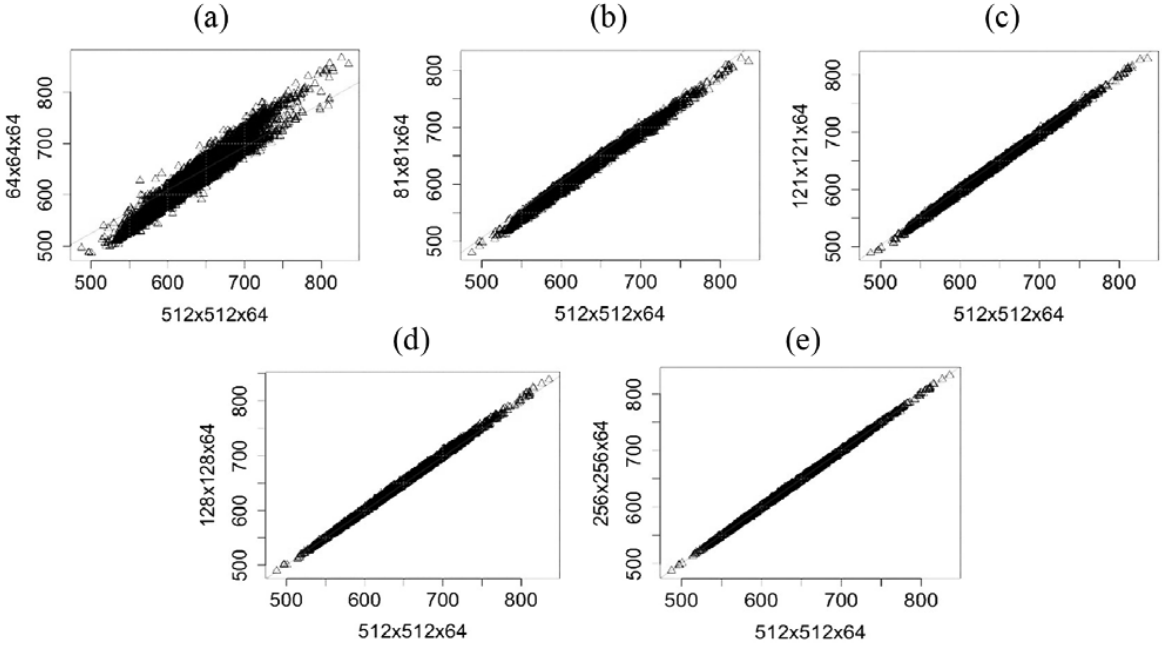

Figure 5.7: Lower grain maximum principal stress correlation plots between values for the reference volume 512x512x64 on the x-axis and values for a) 64x64x64, b) 81x81x64, c) 121x121x64, d) 128x128x64, e) 256x256x64 on the y-axis.

5.1.5 Synthetic results

First, the anisotropy factor effect on convergence is examined with a random texture SRM. The maximum domain is trimmed to voxel dimensions 225^3 (3156 grains), 128^3 (657 grains), 121^3 (613 grains), 81^3 (205 grains) and 64^3 (112 grains) on two different configurations; one set having a shared surface and one set sharing the origin at the center. The structures are covered with four voxels of buffer layers on each side, and three grain pairs from various locations are chosen for convergence study. Fig. 5.8 shows the structures, subdomains and grain pairs of interest with random and preferred structures.

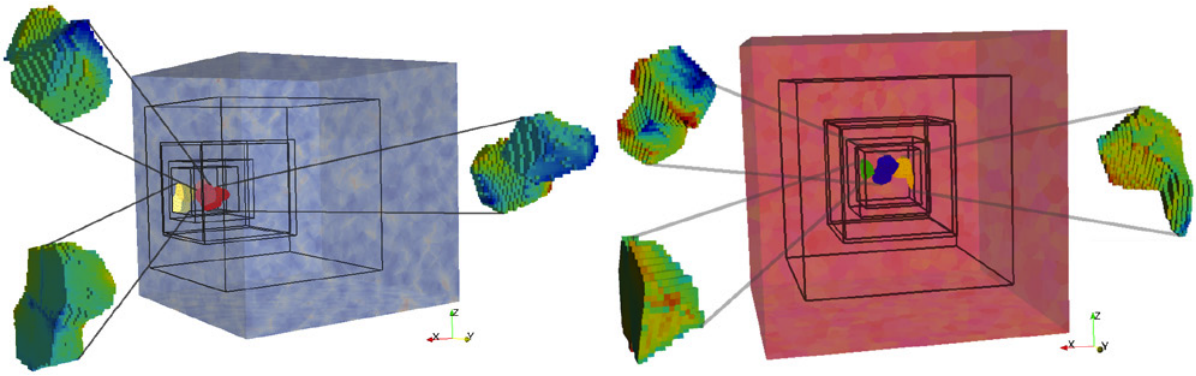

Figure 5.8: SVEs and investigated grain pairs based on the synthetic microstructures: On the left is for the loading condition/direction and anisotropy analysis and on the right is for the texture analysis.

The effect of anisotropy is investigated on one grain pair through the use of Ni elastic properties (5.1.4), Cu elastic properties C_{11}= 168 GPa, C_{12}=122 GPa, C_{44}= 75 GPa corresponding to an anisotropy factor of 3.26, and Al elastic properties C_{11} = 106 GPa, C_{12}=60 GPa, C_{44}= 28 GPa, corresponding to an anisotropy factor of 1.22. Stress distributions in Fig. 5.9 and the Pearson correlation coefficient values presented in table 5.3 indicate that as the anisotropy increases, the correlation decreases; however it is still possible to find convergence in terms of the number of grains. In the case of Al, it is found that even 64^3 is large enough for both the lower and upper grains to exhibit a Pearson correlation coefficient of $\geqslant 0.99$, whereas for Cu, having higher anisotropy, 81^3 is large enough for the lower grain and 128^3 is large enough for the upper grain. Taking anisotropy and the shape of the domain into account, it is concluded that if there is a region of interest, one should include at least to the third nearest neighbor in the simulations.

Table 5.3: Pearson correlation coefficients for anisotropy based on Cu, Ni and Al

		315 vs. 64	315 vs. 81	315 vs. 128	315 vs. 225
Cu (f=3.26)	Lower Grain, Stress	0.98	0.99	0.99	0.99
	Upper Grain, Stress	0.97	0.98	0.99	0.99
Ni (f=2.71)	Lower Grain, Stress	0.98	0.99	0.99	0.99
	Upper Grain, Stress	0.97	0.99	0.99	0.99
Al (f=1.22)	Lower Grain, Stress	0.99	0.99	0.99	0.99
	Upper Grain, Stress	0.99	0.99	0.99	0.99

The effect of loading direction is examined by imposing 0.5 % tension strain along x, y and

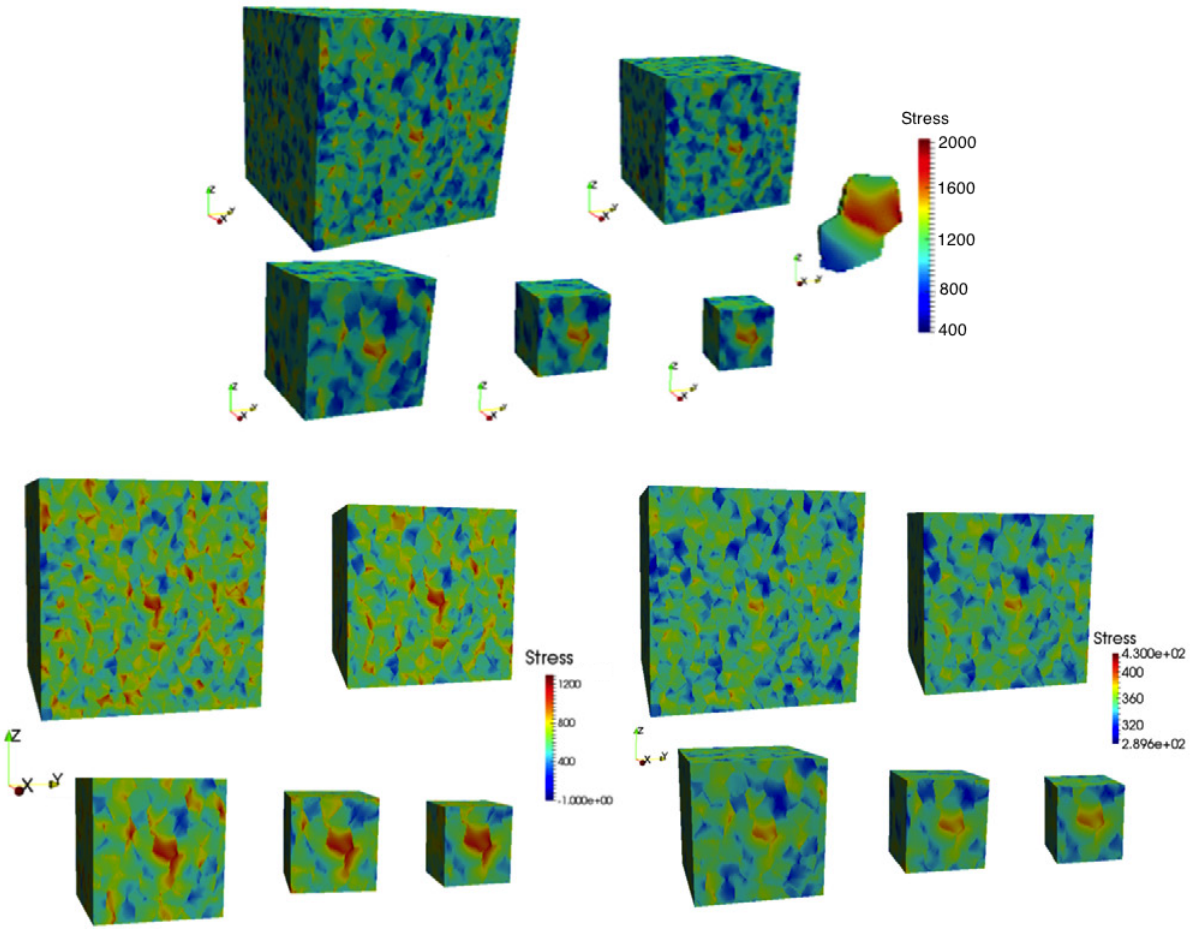

Figure 5.9: Maximum principal stress distributions per domain (315^3, 225^3,128^3, 81^3 and 64^3) for Ni elastic anisotropy parameters on the top, Cu on the bottom left and Al on the bottom right.

z directions on the randomly textured SRMs with Ni elastic properties. For both bulk and surface grains, it is found that for uniaxial x Fig. 5.10.a), y (Fig.5.10.d) and z (Fig.5.10.f) loadings, 121^3 domain size is enough to obtain $r \geqslant 0.99$. A similar trend is observed as the loading condition is changed to combinations of biaxial tension and compression in different directions; convergence is again found on the 121^3 grid (Fig.5.10.b, Fig.5.10.c, Fig.5.10.g,). The assigned texture is found to be the most influential parameter on the sensitivity, especially when the loading is parallel to the preferred orientation (Fig.5.10.h-i). For the case of the (100) preferred texture and tensional x loading along texture fiber, only the largest subset 225^3 having 3156 grains is found to be sufficient for $r \geqslant 0.99$. Pearson correlation coefficients for the combinations of loading state and texture are given in table 5.4.

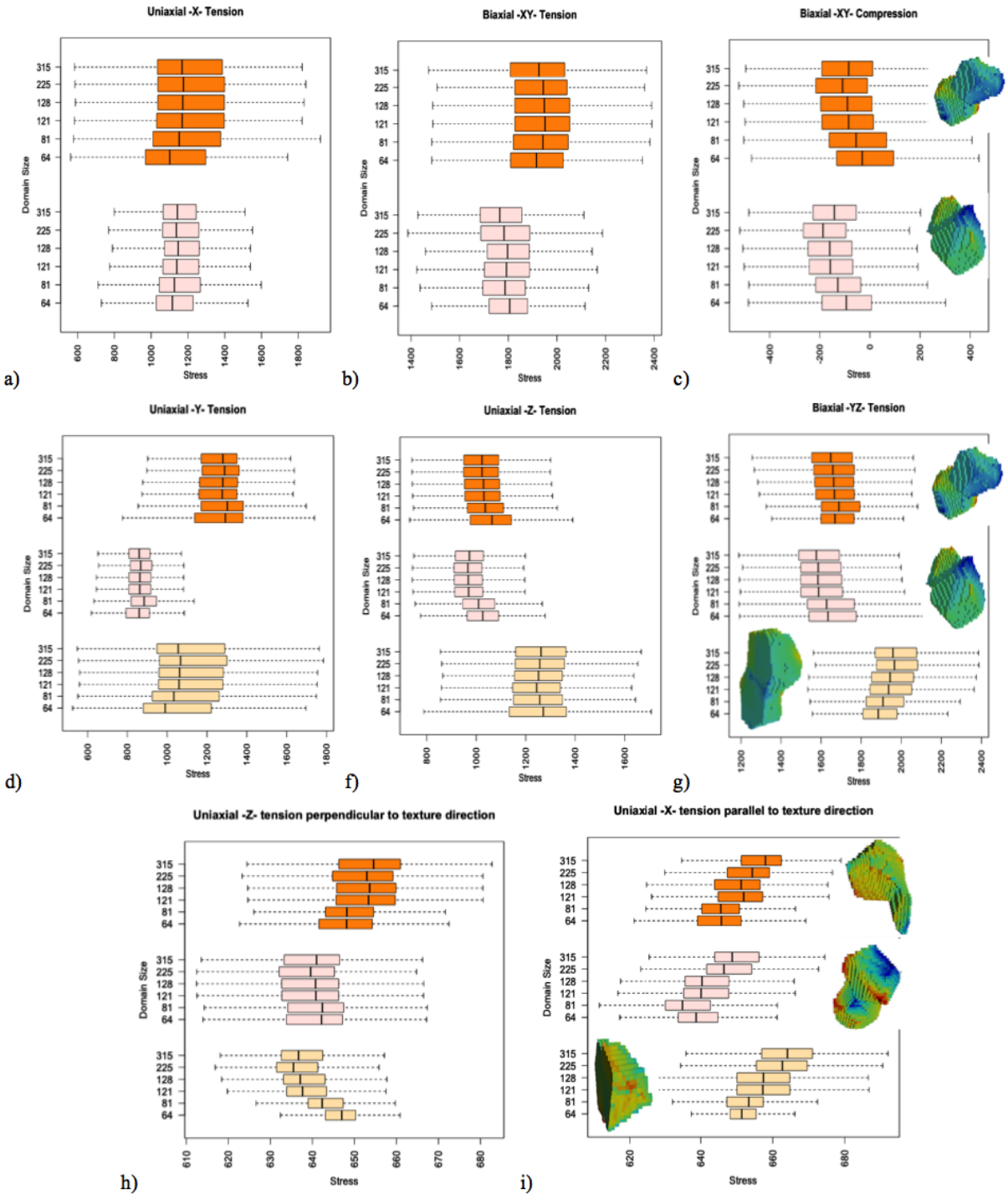

Figure 5.10: Box plots showing the effect of a) loading direction b) loading condition c) texture on the domain size sensitivity.

Table 5.4: Pearson correlation coefficients based on the loading direction, loading condition and texture analyses

		315 vs. 64	315 vs. 81	315 vs. 121	315 vs. 128	315 vs. 225
X Tension	Pair 1	0.97	0.98	0.99	0.99	0.99
	Pair 2	0.97	0.99	0.99	0.99	0.99
XY Tension	Pair 1	0.92	0.96	0.99	0.99	0.99
	Pair 2	0.97	0.99	0.99	0.99	0.99
XY Compression	Pair 1	0.93	0.96	0.99	0.99	0.99
	Pair 2	0.92	0.97	0.99	0.99	0.99
Y Tension	Pair 1	0.98	0.99	0.99	0.99	0.99
	Pair 2	0.95	0.96	0.99	0.99	0.99
	Pair 3	0.97	0.99	0.99	0.99	0.99
Z Tension	Pair 1	0.98	0.99	0.99	0.99	0.99
	Pair 2	0.96	0.98	0.99	0.99	0.99
	Pair 3	0.95	0.98	0.99	0.99	0.99
XZ Tension	Pair 1	0.97	0.98	0.99	0.99	0.99
	Pair 2	0.97	0.98	0.99	0.99	0.99
	Pair 3	0.96	0.99	0.99	0.99	0.99
Z Tension Perpendicular to Texture Fiber	Pair 1	0.89	0.96	0.98	0.99	0.99
	Pair 2	0.97	0.98	0.99	0.99	0.99
	Pair 3	0.96	0.99	0.99	0.99	0.99
X Tension,Along Texture Fiber	Pair 1	0.93	0.93	0.97	0.98	0.99
	Pair 2	0.97	0.93	0.96	0.97	0.99
	Pair 3	0.97	0.98	0.97	0.98	0.99

5.1.6 Discussion

The size, anisotropy, loading condition, loading direction and texture dependence study indicates that the elastic calculation is rather insensitive to the domain size, provided that a few shells of nearest neighbor grains are included. Taking the shape of the domains into account, it is concluded that an SVE can be determined around the region of interest for the local elastic calculations. This provides the researcher the opportunity to map small microstructure regions as in the case of HEDM. Based on the results of the full field elastic FFT calculations on randomly oriented materials with anisotropy factor smaller than 3.26, the local and average mechanical fields are found to be insensi-

tive to the size of the volume when equal or more than third nearest neighbor grains are included in the simulation. For the LSHR analysis this corresponds to 356 total grains in a grid of size 81x81x64 voxels, and for the synthetic structures with 613 total grains in a grid of size 121^3. However, the final remark is such that the texture effect should be considered carefully when combined with the loading conditions and directions.

5.2 Sensitivity Analysis - Viscoplastic and Elasto-Viscoplastic Regimes

5.2.1 Introduction

As stated in Chapter 5.1.1, the purpose of a simulation domain size requirement study is to investigate "How many neighbor grains are required in the simulation, for stress-strain fields to converge for the overall mechanical response and/or for the local response individual grains?". Because the elastic regime results indicate sensitivity to grain interactions with increased contrast, which are defined as texture and anisotropy of the material, the viscoplastic and elasto-viscoplastic responses are expected to be more sensitive to the simulation domain size considering how the plastic regime can induce more anisotropy to the microstructure through lattice reorientation and work-latent hardening. Similar to the elastic case, the sensitivity is tested with both experimentally measured and synthetic microstructures. As the experimental data, the same LSHR HEDM microstructure is used with the same down-sampled volumes, Fig. 5.3. As the synthetic structure, a dual phased titanium microstructure is generated with lath insertion algorithm which is discussed in depth in Chapter VI.

5.2.2 Viscoplastic regime - LSHR results

The same LSHR HEDM dataset is used for the viscoplastic regime domain size sensitivity analysis, with the same down-sampled volumes, which is shown in Fig. 5.3. Using hardening parameters of CRSS (τ_0)= 410.0, initial hardening rate (θ_0)= 280.0, back-extrapolated CRSS (τ_1)= 380.0 and asymptotic hardening rate (θ_1)= 10.0, 40, which are optimized by the non-linear least-squares formulation to fit the experimental data reported by [133], explained in depth in Chapter 4.2.2; strain boundary condition in increment of 0.0025 (adding up to 10 % macroscopic tensional strain) is applied along z direction. Fig. 5.11 shows the von-Mises stress distributions per domain, as well as within the two grains of interest. Although both hot and cold spots seem to align qualitatively from Fig. 5.11, quantitative voxel by voxel comparison, table 5.5 shows that for a correlation larger than

Pearson's r = 0.99, 3114 or more grains must be present in the viscoplastic simulation domain.

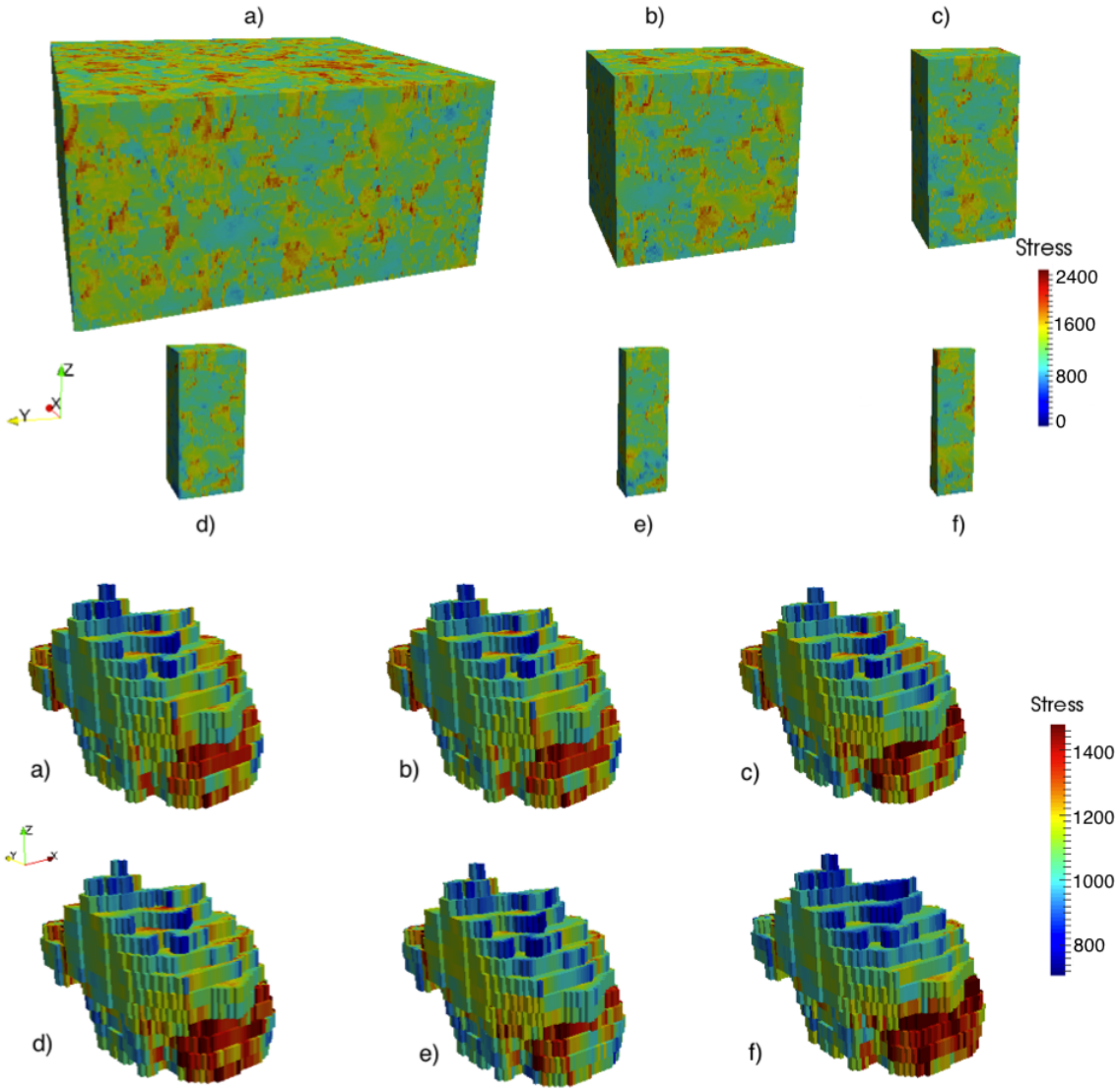

Figure 5.11: Viscoplastic regime von-Mises stress distributions for the SVEs and two neighbor grains around the identified microcrack for domain sizes of a) 512x512x64 b) 256x256x64 c) 128x128x64 d) 121x121x64 e) 81x81x64 f) 64x64x64. The stress values are rescaled with respect to the largest SVE for comparison.

Table 5.5: Viscoplastic regime pearson correlation coefficients for von-Mises stress and strain values within the lower crack neighboring grain

	512 vs. 256	512 vs. 128	512 vs. 121	512 vs. 81	512 vs. 64
Lower Grain, Strain	0.994	0.751	0.794	0.704	0.424
Lower Grain, Stress	0.992	0.869	0.889	0.647	0.512

For both stress and strain fields, r $\geqslant$ 0.99 is only observed for 256x256x64 grid. Depicted in the

von-Mises stress, Fig. 5.12, and von-Mises strain, Fig. 5.13 correlation plots and the r values, strain distribution is found to be more sensitive to the shape of the domain in the viscoplastic regime. A possible explanation is that since Ni has FCC crystal structure and only slip based deformation is activated, the strain tends to localize in bands as a result of dislocation pile up, making strain field more sensitive to the neighborhood. Viscoplastic analysis results indicate that as the contrast ratio of properties increases, in this case because of rate-sensitive constitutive equation and the localized strain bands, so does the sensitivity to the neighborhood interactions. Hence, it can be said that the strain distributions are sensitive to the entire shape of the strained volume.

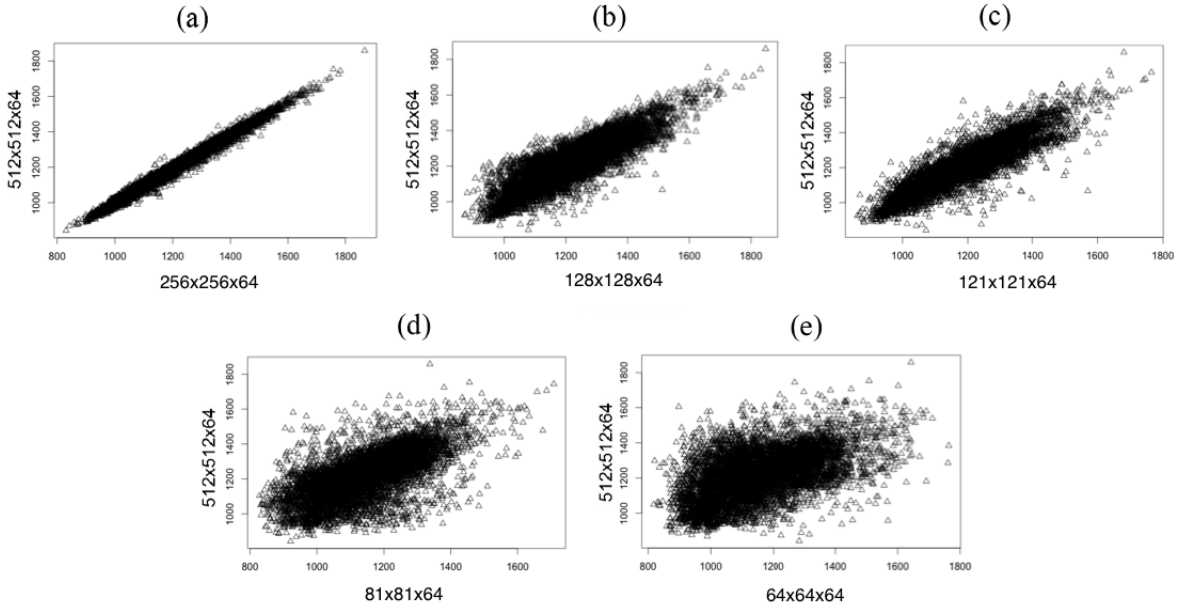

Figure 5.12: Viscoplastic regime lower grain von-Mises stress correlation plots between values for the reference volume 512x512x64 on the x-axis and values for a) 256x256x64, b) 128x128x64, c) 121x121x64, d) 81x81x64, e) 64x64x64 on the y-axis.

5.2.3 Elasto-viscoplastic regime - LSHR results

Following the same methodology as the elastic and viscoplastic sensitivity analyses, LSHR structures are used to check the simulation domain size requirement for converging local stress-strain distributions. The structures are covered with buffer layers in x-y surfaces, and tensional strain is applied along z direction. A total of 10 % macroscopic strain is implemented through 200 deformation steps of 0.0005 increments.

When a region of interest is chosen (such as crack neighbor grains), the distribution is found

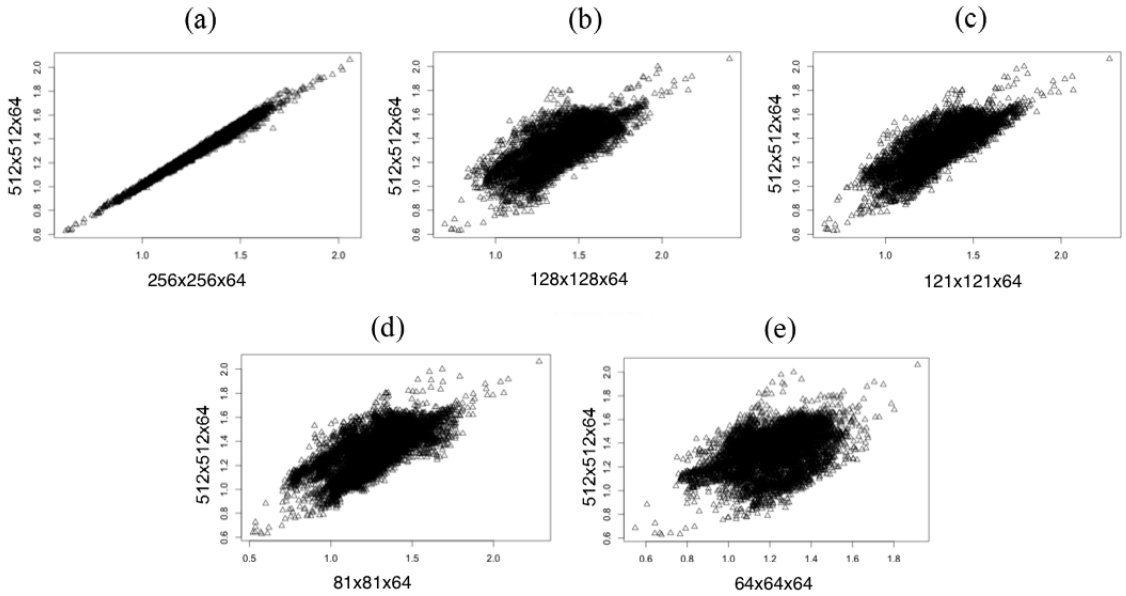

Figure 5.13: Viscoplastic regime lower grain von-Mises strain correlation plots between values for the reference volume 512x512x64 on the x-axis and values for a) 256x256x64, b) 128x128x64, c) 121x121x64, d) 81x81x64, e) 64x64x64 on the y-axis.

somewhat insensitive to the domain size, and a good linear correlation is observed in between the largest and the subsize domains, Fig. 5.15. What is surprising about the analysis is that the local field comparisons between the largest reference domain (512x512x64) and even the smallest one (64x64x64) are not as scattered as the vpFFT study. Elasto-viscoplastic regime is still more sensitive to neighborhood as compared to elastic regime. However, the viscoplastic analysis had shown much lower correlation coefficient values. This is attributed to the fact that the initial elastic step lowers the contrast ratio and smooths the response. Similar to the viscoplastic regime, strain field is found to be more sensitive to the neighborhood effects than the stress field. For r $\geqslant$ 0.99 as convergence criterion, 256x256x64 is the minimum required domain size (total of 3114 grains), table 5.6. A note here is that an intermediate domain between 256x256x64 and 128x128x64 might give r $\geqslant$ 0.99.

Table 5.6: Elasto-viscoplastic regime pearson correlation coefficients for von-Mises stress and strain values within the lower crack neighboring grain

	512 vs. 256	512 vs. 128	512 vs. 121	512 vs. 81	512 vs. 64
Lower Grain, Strain	0.996	0.961	0.931	0.823	0.745
Lower Grain, Stress	0.997	0.974	0.981	0.936	0.887

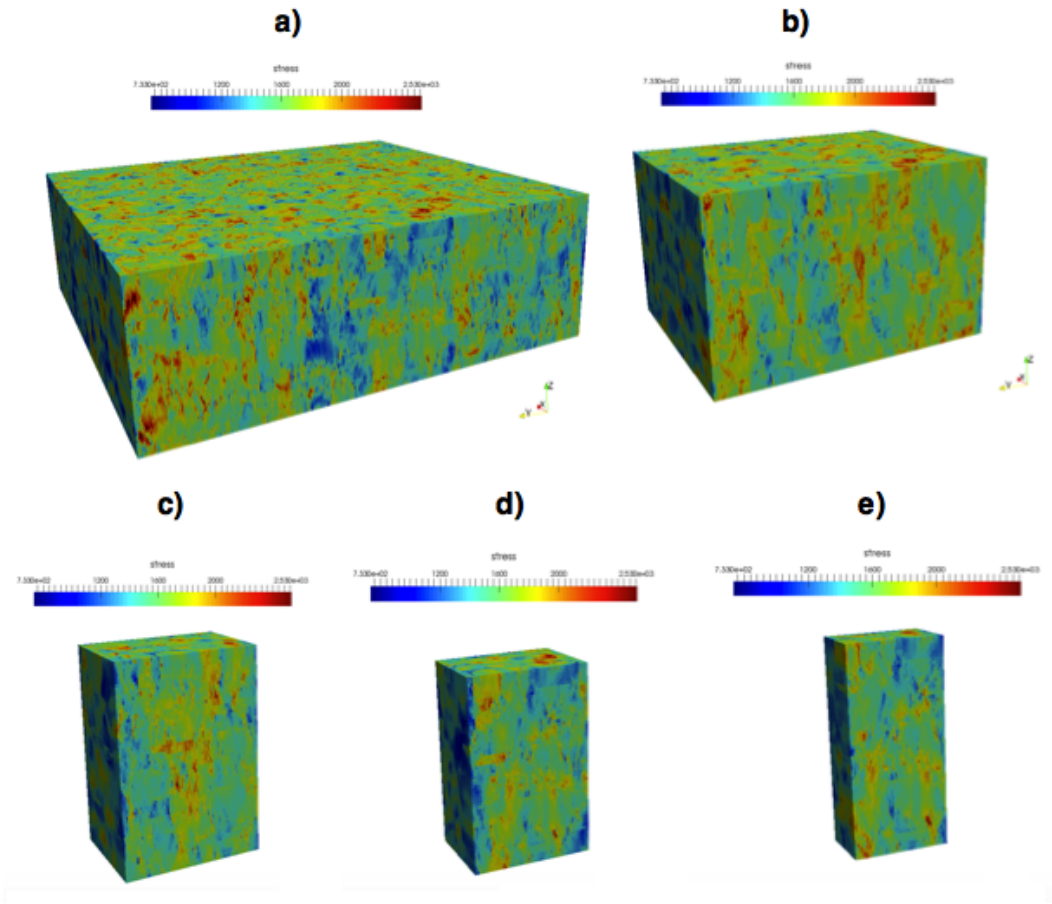

Figure 5.14: Elasto-viscoplastic regime von-Mises stress distributions for the domain sizes of a) 512x512x64 b) 256x256x64 c) 128x128x64 d) 121x121x64 e) 81x81x64. The stress values are rescaled with respect to the largest SVE for comparison.

5.2.4 Elasto-viscoplastic regime - Synthetically generated dual phase titanium results

The domain size sensitivity analysis of the elasto-viscoplastic regime indicated the possibility of finding an intermediate domain size between 256x256x64 and 128x128x64 for convergence of both local and macroscopic mechanical behavior. As we investigate the microstructure-property relationship of titanium alloys in this thesis work, dual phase titanium microstructures with lamellar alpha (hcp structure) laths and retained beta (bcc structure) grains were simulated for the synthetic microstructure based elasto-viscoplastic regime sensitivity analysis. The microstructures were generated via the lath insertion algorithm which is discussed in depth in Chapter VI, where each daughter hcp lath follows BOR of close-packed $\{011\}$ plane of the parent bcc lattice parallel to the close-packed (0001) plane of the hcp lattice, and the $< 111 >$ direction in the bcc lattice parallel to the

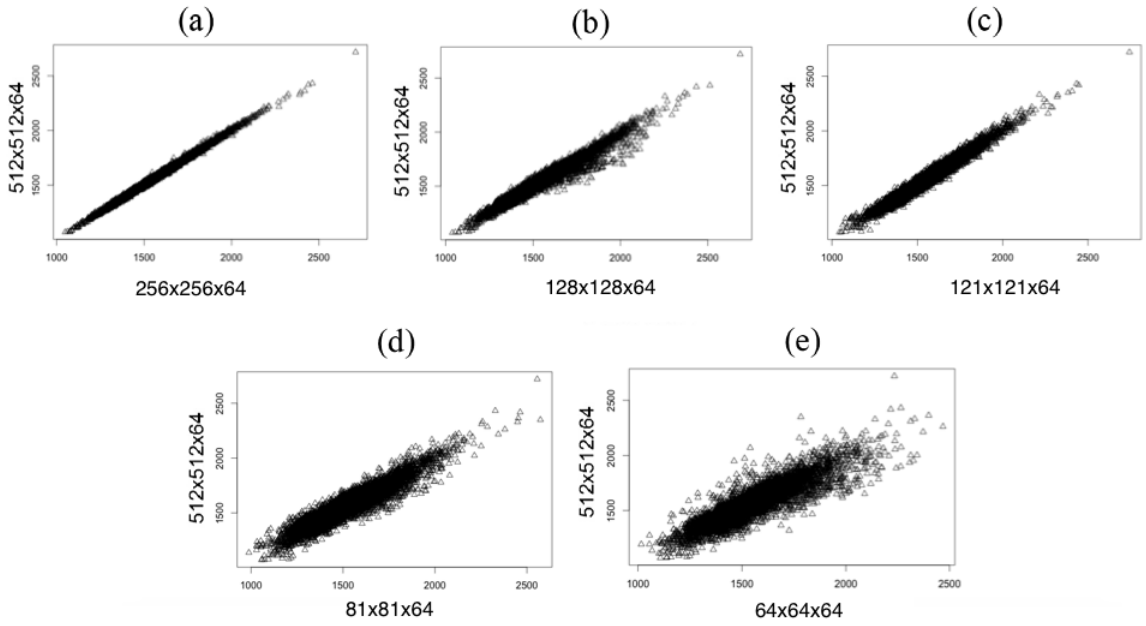

Figure 5.15: Elasto-viscoplastic regime lower grain von-Mises stress correlation plots between values for the reference volume 512x512x64 on the x-axis and values for a) 256x256x64, b) 128x128x64, c) 121x121x64, d) 81x81x64, e) 64x64x64 on the y-axis.

$< 11\bar{2}0 >$ direction in the hcp lattice. In order to obtain the highest level of microstructural heterogeneity, a base microstructure of 216^3 grid size is generated with random variant (12 possible daughter hcp orientations through BOR with parent bcc grain) selection, average alpha lath size of 2 μm, average equiaxed morphology beta grain size of 145 μm, and a 50-50 phase fraction. Two different analyses are performed by modifying the base structure, Fig. 5.16.a:

i) Fourier grid resolution sensitivity study where the 216^3 microstructure is kept the same, but the Fourier grid resolution is changed by a factor of 1.5 and 2, giving grid sizes of 320^3 and 432^3,

ii) Domain size sensitivity study where smaller size structures of 64^3, 128^3 and 196^3 are cropped out from the origin of the base structure. A lath colony with a simulated hot spot is chosen to check local convergence, seen embedded in the 64^3 structure depicted in Fig. 5.16.b.

Using the Voce hardening parameters that are optimized from the bottom 1.a sample of the Ti-6Al-4V tensile dataset, listed in Table B.1, and elastic parameters listed in Table 6.2, structures were deformed to 3 % strain with combined strain/stress boundary conditions. Note that since the microstructure is different and the strong phase α fraction is less than the experimental Ti-6Al-4V data that was used for hardening parameter extraction, the simulated macroscopic stresses are expected to be lower than the experimental data.

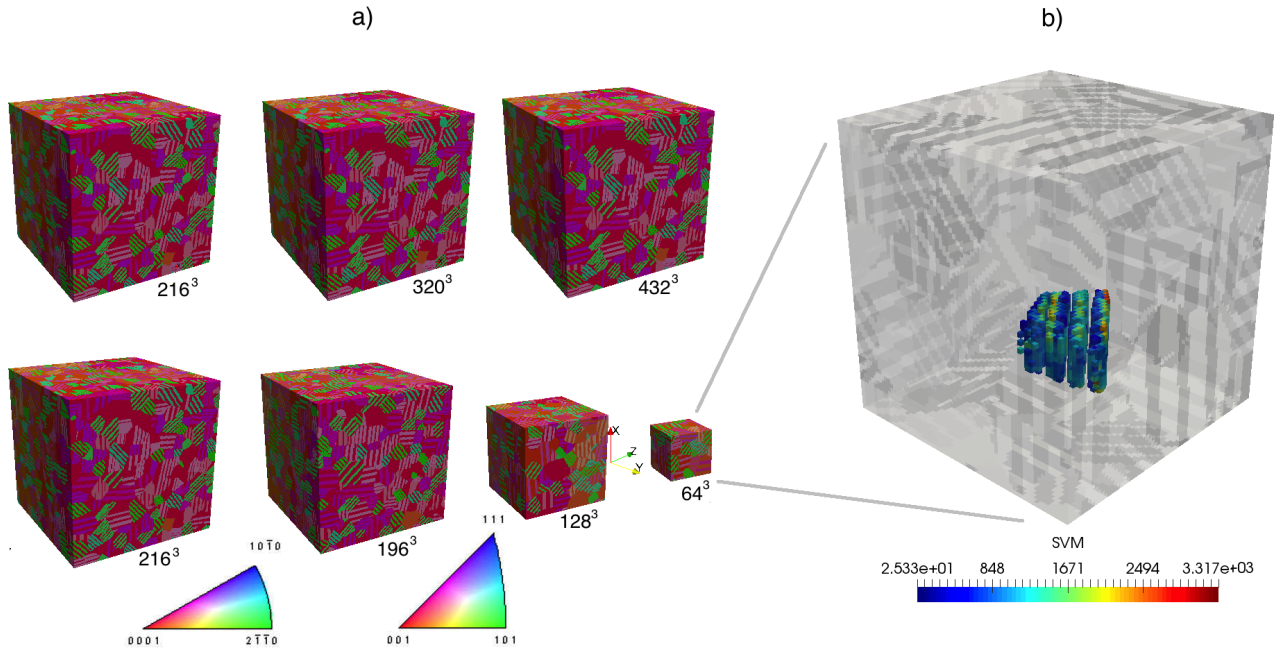

Figure 5.16: a) Dual phase titanium microstructures with phase fractions of 50 % alpha lath and 50 % retained beta, represented in IPF color scheme. The upper row is the Fourier grid resolution study structures, and the lower row is the domain size study structures. b) Alpha lath colony of interest with observed simulated hot-spot, seen embedded in the cropped 64^3 domain

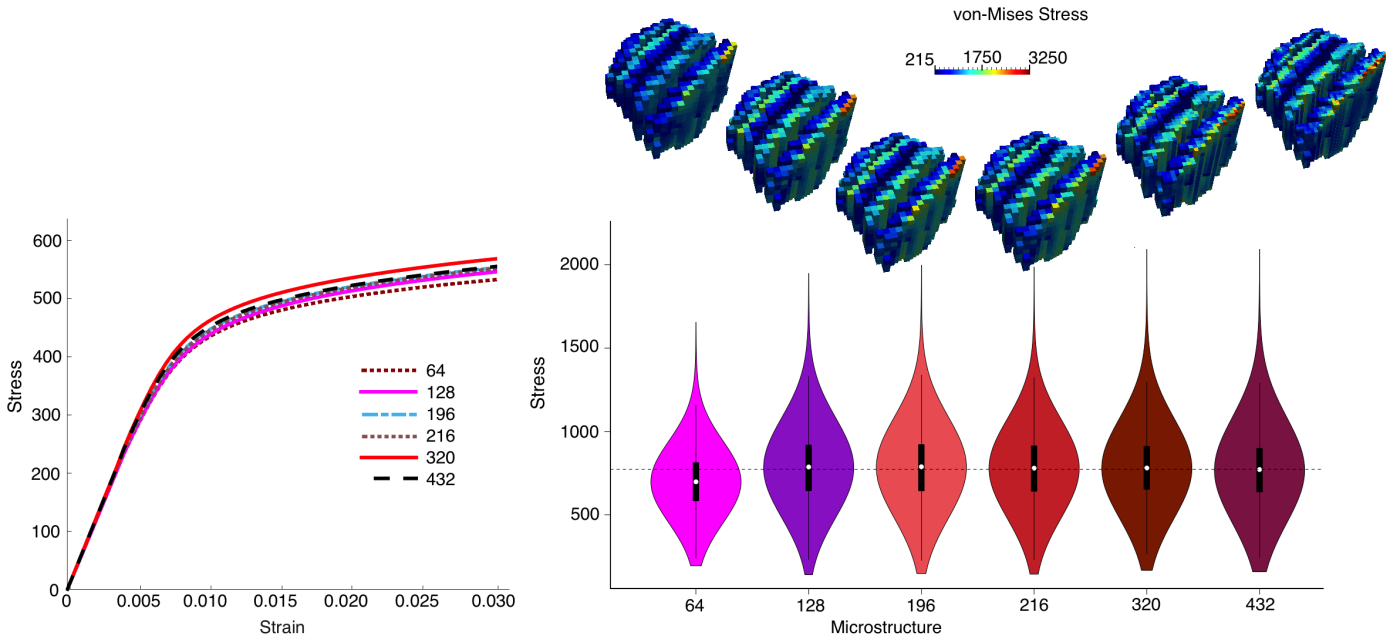

Figure 5.17: Macroscopic stress-strain curves and the local von-Mises stress distributions for simulation domain sizes of 64^3, 128^3, 196^3, 216^3, 320^3 and 432^3. von-Mises stress distributions within the chosen alpha laths are plotted with their corresponding parent structure.

Qualitatively, both the homogenized values represented by the stress-strain curves and the local distributions represented by the violin plots and the von-Mises stress distributions within the chosen alpha laths in Fig. 5.17 indicated that 196^3 structure with 1 μm/voxel Fourier grid resolution is large enough for convergence. It is also checked quantitatively with QQ-plots (comparison of quantiles) and reported Pearson's r values, Fig. 5.18, where the Pearson's r $\geqslant$ 0.99 is reached with the 196^3 structure. Pearson's r is not calculated for the largest two structures as the vector dimensions are incompatible with the 216^3 structure (finer voxelization). While 196^3 is found large enough for convergence, because the local cluster was more accommodating in decomposing the size of 216^3, 216^3 is chosen to be the SRVE to inform the micromechanical study, discussed in Chapter VI.

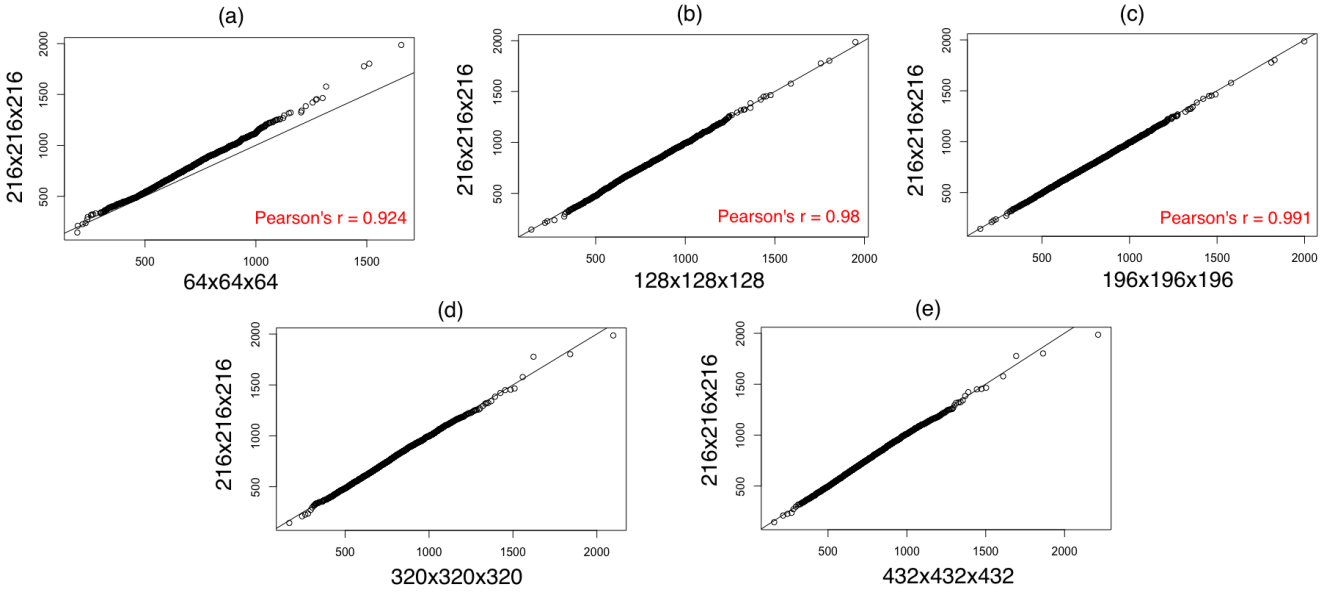

Figure 5.18: Linear correlation comparisons via Q-Q plots between the 216^3 structure and a) 64^3, b) 128^3 c) 196^3, d) 320^3 and e) 432^3.

5.2.5 Discussion

The simulation domain size requirement for the viscoplastic and elasto-viscoplastic FFT solutions is found to be larger than the elastic solution as a result of higher contrast ratio, caused by the rate-sensitive constitutive equation. Especially for the viscoplastic regime where the deformation is controlled by slip activity, dislocation accumulation and strain localization gives sensitivity to neighborhood size, more so for the strain field, while the initial elastic steps of the elasto-viscoplastic regime is hypothesized to lower the contrast ratio and hence the neighborhood size sensitivity by smooth-

ing the response. For both regimes a minimum simulation domain size was successfully determined as 3114 grains on a 256x256x64 grid size for the LSHR structure. Dual-phase titanium study investigated the Fourier grid resolution as well the domain size sensitivity, concluding 1 μm/voxel resolution on a 196^3 grid was large enough for convergence. Taking the size of the domains into account, it is concluded that the elasto-viscoplastic regime is less sensitive to the neighborhood than viscoplastic as a result of elastic smoothening.

Overall, the sensitivity study can be summarized as:

i) As the contrast of properties (e.g., texture, field localization, anisotropy, rate-sensitivity) increases, so does the mimimum simulation domain size requirement. Comparing the neighborhood sensitivity of different deformation regimes, it is found that elastic response<elasto-viscoplastic response<viscoplastic response.

ii) These results support the second part the hypotheses, which was "For increasing the computational efficiency of the Fast Fourier Transform (FFT) based algorithm as a micromechanical modeling technique to study the microstructure-deformation relationship, a simulation domain size sensitivity study is proposed with the expectation of finding a strong relation in between a minimum required simulation domain size, i.e. number of grains included in the calculation, and the contrast ratio of properties for the elastic, viscoplastic and elasto-viscoplastic regimes. Finding a Pearson correlation coefficient r = 0.99 is anticipated when the downsampled simulation results are compared to one another and the largest sized domain."

CHAPTER VI

Effect of microstructure on the elasto-viscoplastic deformation of dual phase titanium structures

6.1 Introduction

Powder-bed based additive manufacturing (AM) of metallic components, in which a 3D shape is written into successive layers of powder using an electron or laser beam under computer control, is increasingly being implemented to produce structural parts. Having a wide range of application in the aerospace, automotive and medical industries, AM of titanium components is now valued because of the near-net shape and reduced machining cost advantages of the technique [1]. However, since titanium is an allotropic element that can exist in more than one crystallographic form depending on the chemo-thermo-mechanical process history, the rapid cooling inherent in the AM technique makes the prediction of the component microstructure and the mechanical properties challenging. For instance, the room temperature alpha, or hexagonal close-packed (hcp), phase can co-exist with the high temperature (above 883 °C) beta, or body-centered cubic (bcc), phase when alloyed with elements such as aluminum and oxygen that stabilize alpha, or elements such as vanadium and molybdenum that stabilize beta [6]. Furthermore, the dual-phase alloys exhibit a wide variety of distinct microstructures such as fully lamellar, duplex, or fully equiaxed, with varying texture evolution as a function of the thermomechanical history [2–4], all of which influence the mechanical properties.

While there are established process - structure - property relationships for different alpha/beta titanium alloys in literature [5], the large thermal gradients and cooling rates inherent in powder-bed metal AM makes for challenges in the prediction of mechanical properties. The beam scanning though successive layers means that each location experiences a series of thermal spikes, whose

precise sequence depends on location in the part. The thermal history also involves slow changes in temperature mainly as a function of build height, resulting in anisotropic and heterogeneous microstructures within each AM component. For instance, it has been shown that depending on the beam power/velocity parameters, a Ti-6Al-4V microstructure can change from martensitic or fine acicular α' structure at the high cooling rate top of the build height, into fine $\alpha+\beta$ lamellae, Widmanstätten, or a mixture of colonized lamellar α and coarse acicular α' phases at the slower cooling rate, middle of the build height sections [15,16,38]. Furthermore, the solidification structure is affected by the cooling rate and thermal gradient dependent prior β morphology and size, which can be varied substantially through control of the process conditions [86,87]. As the α lath thickness and prior β grain size increases with decreased cooling rate, the ultimate tensile strength (UTS) and yield strength (YS) values are known to decrease [2]. This in turn causes a mechanical property anisotropy between the exterior AM regions with finer microstructures, and the coarser interior regions [10].

Since microstructural features are known to determine the microscopic and macroscopic mechanical behavior, it is important to quantify and model the relationships between the properties and the prior β grain size and morphology, the thickness and size of individual α laths, and the volume fraction and orientation distribution of the phases. For this purpose, in this study we present a new methodology to generate dual phase titanium microstructures, a statistically representative volume element (SRVE) simulation size requirement analysis, a synthetic microstructure database, and the micromechanical response modeling of the structures through the full-field fast Fourier transform (FFT) based elasto-viscoplastic technique as to quantify the relative effect of individual microstructure descriptors.

6.2 Dual-phase Titanium Representative Structures with Varying Microstructural Features

Microstructure based crystal plasticity models are extensively operated to simulate the elasto-viscoplastic behavior of polycrystalline materials by using the grain maps as input data. When the interest is in the investigation of structure-property relationships through large dataset analysis, microstructural characterization such as surface mapping via EBSD or 3D mapping via synchrotron based techniques can be time and budget consuming. One possible solution to increase the microstruc-

ture database is the computational approach via digital generation of statistically representative microstructures. Various methods have been developed for three-dimensional statistical microstructure reconstruction, such as the 3D Voronoi tessellation, where a volume is filled with random points and then the point joining line perpendicular bisecting planes are tessellated such that the volume is divided into Voronoi cells, each of which corresponds to a unique grain [134]. Other methods involve packing spheres with a lognormal volume distribution into a domain, and then using the center of masses as tessellation initiation points [135], or using ellipsoid distributions to approximate the grain size and shape distributions that exist in the real microstructures for determining Voronoi seed points [96, 136, 137].

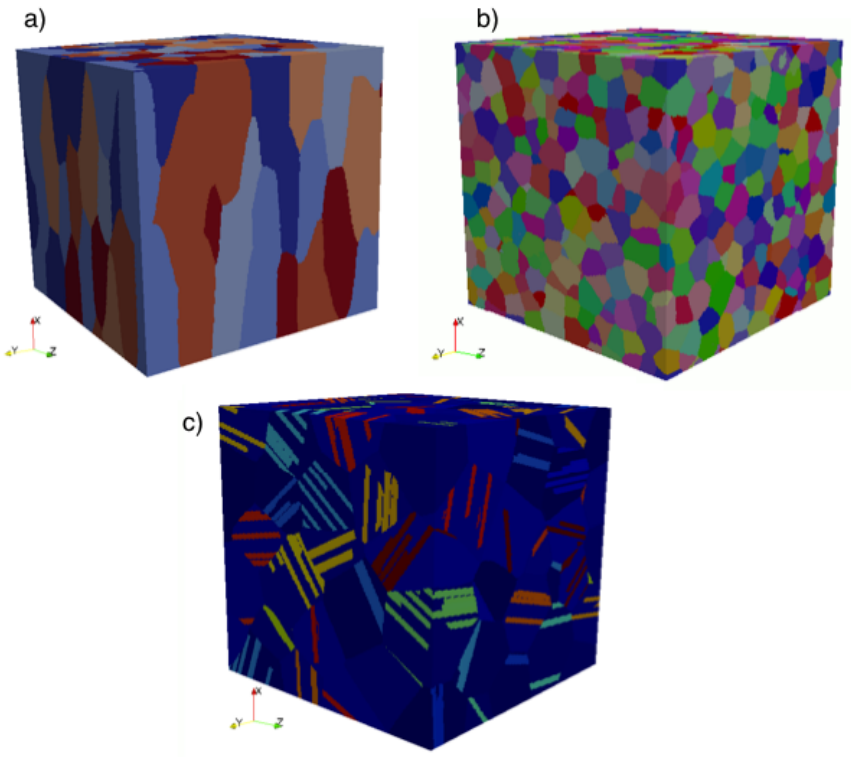

Figure 6.1: Examples of digital microstructures a) A preferred (001) axis columnar prior β structure b) An equiaxed prior β structure c) A dual-phase β matrix - α lath structure

Thanks to ongoing developments in packing algorithms and general computational capability, digital representation of grain-scale microstructures has extended to more complex materials. For dual-phase titanium, examples include: beta processed titanium where the lamellar structure is homogenized for simulation efficiency [60]; a case in which the alpha/beta structure is assumed to be a colony grain structure with random orientation assignment [61]; a microstructure in which grains

are assumed to be cubes, and the lamellar duplex structure is homogenized for meshing efficiency [62]; and, a case in which the bimodal primary alpha+lamellar colony characteristics are represented through size distributions [63]. Although these structures are shown to be statistically representative in various ways, the computational expense limited what could be accomplished with finite element based micromechanical modeling that explicitly describe the lamellar morphology, individual α laths, or Widmanstätten characteristics, because the two-phase lamellar structures require a large element count and correspondingly large number of degrees of freedom. The present study sidesteps this issue by using a meshless, FFT-based full field micromechanical model, which can compute full field solutions directly on image of microstructures with >100 prior β grains and >50000 α laths.

For the purpose of generating statistically representative multi phase digital microstructures to specifically address AM titanium, a set of statistics is extracted from the additively manufactured Ti-6Al-4V literature. This suggests using an average columnar or equiaxed prior β width of 50 μm - 200 μm [138,139], an average α lath size of 0.5 μm - 2 μm [70,140], and a preferred prior β texture of (001) with a Burgers orientation relationship (BOR) between the phases [80,82,138]. The strong texture arises from the near-universal observation of columnar solidification in this alloy, which is unsurprising in view of the unusually small freezing range in this alloy [141]. Since the objective is forming a microstructure-mechanical response database, initial beta microstructures, Fig.6.1, are created via DREAM3D [142] based on the parent grain size statistics, which are then modified to include the features of interest, i.e., the lamellae, by using a transformation phase insertion algorithm. The algorithm consists of operating on each of the parent phase voxel structures to insert additional grains that represent the second (hexagonal) phase by calculating the center of mass and spherical equivalent radius of each parent grain for controlling the lath width and length, until a given number of daughter grains are successfully generated. The daughter grain orientation is defined by rotation from the parent grain in accordance with the applicable orientation relationship. For titanium, the BOR, where the close-packed $\{011\}$ plane of the bcc lattice is parallel to the close-packed (0001) plane of the hcp lattice, and the <111>direction in the bcc lattice is parallel to the <11$\bar{2}$0>direction in the hcp lattice, results in 12 possible variants and each habit plane/direction produces a distinct orientation. The set of axis-angle pair misorientations from parent bcc to daughter hcp grains is given in Table 6.1. In order to illustrate how the parent/daughter orientation relation-

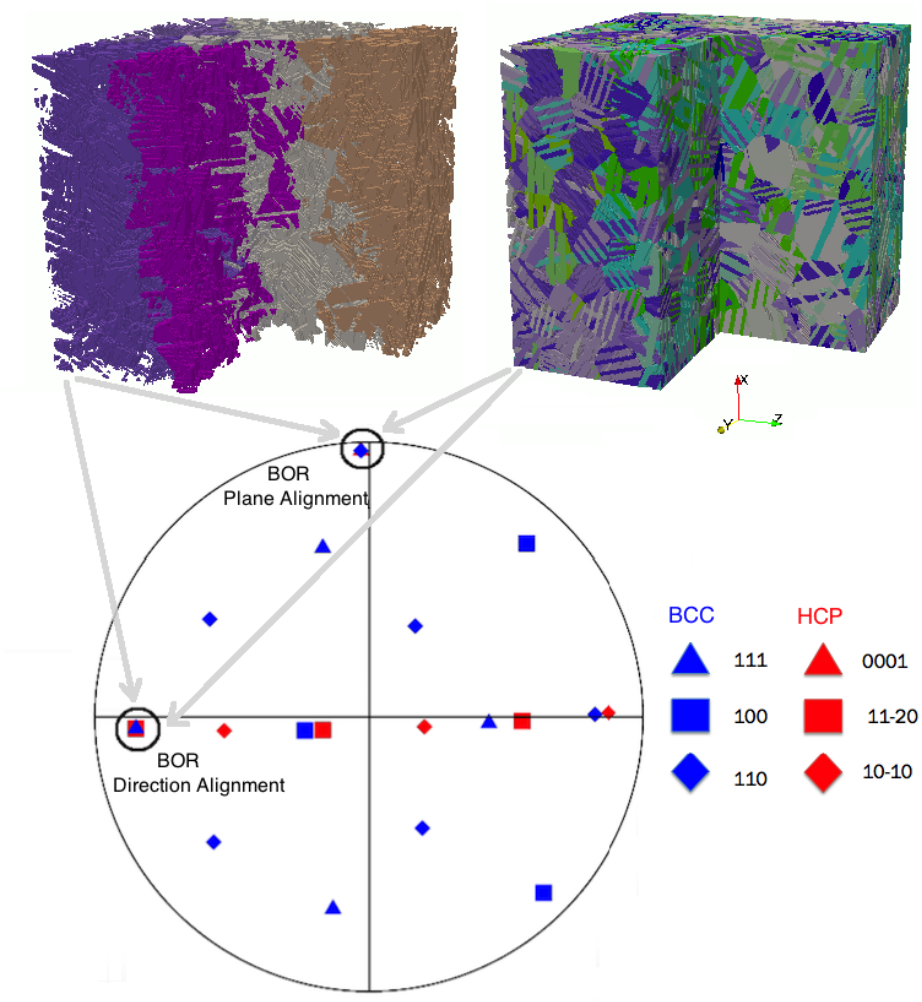

Figure 6.2: Columnar retained beta grains, inserted alpha laths and the Burgers OR (BOR) between the marked beta grain and alpha lath for a 256 x 256 x 256 digital microstructure. The grains are colored by Euler angles on an arbitrary scale.

ship is maintained in the algorithm, columnar retained beta, inserted alpha laths, and BOR between the marked beta grain and alpha lath for a 256x256x256 voxel digital microstructure is shown in Fig. 6.2. To create the dual phase titanium microstructure/mechanical response database, multiple structures with varying features are generated via the insertion method explained above. In Fig. 6.4, statistically representative microstructure generation steps and a subset of the synthetic structures are illustrated.

In this study, a modified version of the Voce [95] hardening model is used for the plastic deformation, which is characterized by an evolution of the threshold stress with accumulated shear strain in the form of

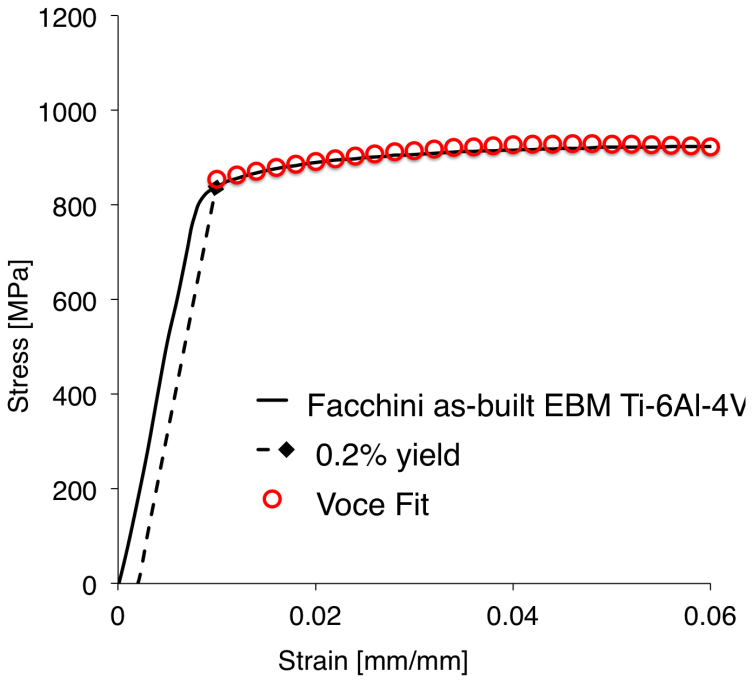

Figure 6.3: Electron beam melted, as built Ti-6Al-4V stress-strain [72] fit for extracting modified Voce hardening parameters

$$\hat{\tau}^S = \tau_0^S + (\tau_1^S + \theta_1^S \Gamma)(1 - exp(-\Gamma|\frac{\theta_0^S}{\tau_1^S}|)) \tag{6.1}$$

giving 4 parameters for each slip system in each individual phase, where τ_0^S is the initial critical resolved shear stress (CRSS), τ_1^S is the initial hardening rate, θ_0^S is the asymptotic hardening rate and θ_1^S is the back-extrapolated CRSS. For titanium alloys, bcc phase is generally accepted to be the softer phase. Furthermore, different hcp systems has different activation barriers (CRSS). For this study, CRSS ratios of 1:0.7:3 [44] are used for basal:prism:pyramidal <c+a> slip in the hcp phase, and CRSS ratios of 1:1:1 are used for slip in the bcc phase. The onset of plastic deformation is identified using a 0.2 % offset line. A set of modified Voce hardening parameters are extracted from a reported set of AM Ti-6Al-4V tensile data [72] by fitting the stress-strain curve for bcc and hcp phases simultaneously via the VPSC model, Fig. 6.3. The parameter optimization process is discussed in depth in Chapter 4.2.2. For the elastic regime, the stiffness values reported by Stapleton et al. [143] are used. Both the elastic and plastic model parameters are listed in Table 6.2. Note that the material parameters are chosen as the basis for all the structures. It is possible to implement different hardening models and parameters without changing the elasto-viscoplastic algorithm.

Table 6.1: Burgers orientation relationship and axis/angle pair for β –>α transformation

	Axis	Angle
$(1\ 1\ 0)_\beta$ // $(0\ 0\ 0\ 1)_\alpha$ $[\bar{1}\ 1\ \bar{1}]_\beta$ // $[1\ 1\ \bar{2}\ 0]_\alpha$	(-0.067, -0.791, -0.607)	125.77
$(1\ 1\ 0)_\beta$ // $(0\ 0\ 0\ 1)_\alpha$ $[1\ \bar{1}\ \bar{1}]_\beta$ // $[1\ 1\ \bar{2}\ 0]_\alpha$	(0.762, -0.642, 0.085)	90.41
$(\bar{1}\ 0\ 1)_\beta$ // $(0\ 0\ 0\ 1)_\alpha$ $[1\ \bar{1}\ 1]_\beta$ // $[1\ 1\ \bar{2}\ 0]_\alpha$	(-0.244, 0.769, 0.590)	56.6
$(\bar{1}\ 0\ 1)_\beta$ // $(0\ 0\ 0\ 1)_\alpha$ $[1\ 1\ 1]_\beta$ // $[1\ 1\ \bar{2}\ 0]_\alpha$	(0.244, 0.769, -0.590)	56.6
$(0\ 1\ 1)_\beta$ // $(0\ 0\ 0\ 1)_\alpha$ $[1\ 1\ \bar{1}]_\beta$ // $[1\ 1\ \bar{2}\ 0]_\alpha$	(0.594 -0.307 -0.742)	69.73
$(0\ 1\ 1)_\beta$ // $(0\ 0\ 0\ 1)_\alpha$ $[\bar{1}\ 1\ \bar{1}]_\beta$ // $[1\ 1\ \bar{2}\ 0]_\alpha$	(0.194, -0.375, -0.906)	129.73
$(0\ 1\ \bar{1})_\beta$ // $(0\ 0\ 0\ 1)_\alpha$ $[\bar{1}\ 1\ 1]_\beta$ // $[1\ 1\ \bar{2}\ 0]_\alpha$	(0.431, 0.833, 0.345)	159.73
$(0\ 1\ \bar{1})_\beta$ // $(0\ 0\ 0\ 1)_\alpha$ $[1\ 1\ 1]_\beta$ // $[1\ 1\ \bar{2}\ 0]_\alpha$	(0.872, 0.451, 0.187)	140.26
$(1\ 0\ 1)_\beta$ // $(0\ 0\ 0\ 1)_\alpha$ $[\bar{1}\ 1\ 1]_\beta$ // $[1\ 1\ \bar{2}\ 0]_\alpha$	(-0.379, -0.120, -0.917)	147.49
$(1\ 0\ 1)_\beta$ // $(0\ 0\ 0\ 1)_\alpha$ $[1\ 1\ \bar{1}]_\beta$ // $[1\ 1\ \bar{2}\ 0]_\alpha$	(-0.244, -0.769, -0.590)	56.6
$(1\ \bar{1}\ 0)_\beta$ // $(0\ 0\ 0\ 1)_\alpha$ $[1\ 1\ \bar{1}]_\beta$ // $[1\ 1\ \bar{2}\ 0]_\alpha$	(-0.762, -0.642, -0.085)	90.41
$(1\ \bar{1}\ 0)_\beta$ // $(0\ 0\ 0\ 1)_\alpha$ $[1\ 1\ 1]_\beta$ // $[1\ 1\ \bar{2}\ 0]_\alpha$	(-0.837, -0.071, -0.542)	114.54

Table 6.2: Bcc and hcp elastic constants and hardening parameters that are used in the micromechanical model

Elastic constants [GPa]	C_{11}	C_{12}	C_{13}	C_{33}	C_{44}
bcc	130	90	90	130	65
hcp	143	110	90	177	40
Modified Voce hardening parameters [MPa]	τ^0	τ^1	θ^0	θ^1	
bcc (for all slip modes)	41.09	99.62	971.27	1.6	
hcp (basal)	184.95	56.75	1160	-18.9	
hcp (pryramidal)	264.21	56.75	1160	-18.9	
hcp (prismatic <a+c>)	792.63	56.75	1160	-18.9	

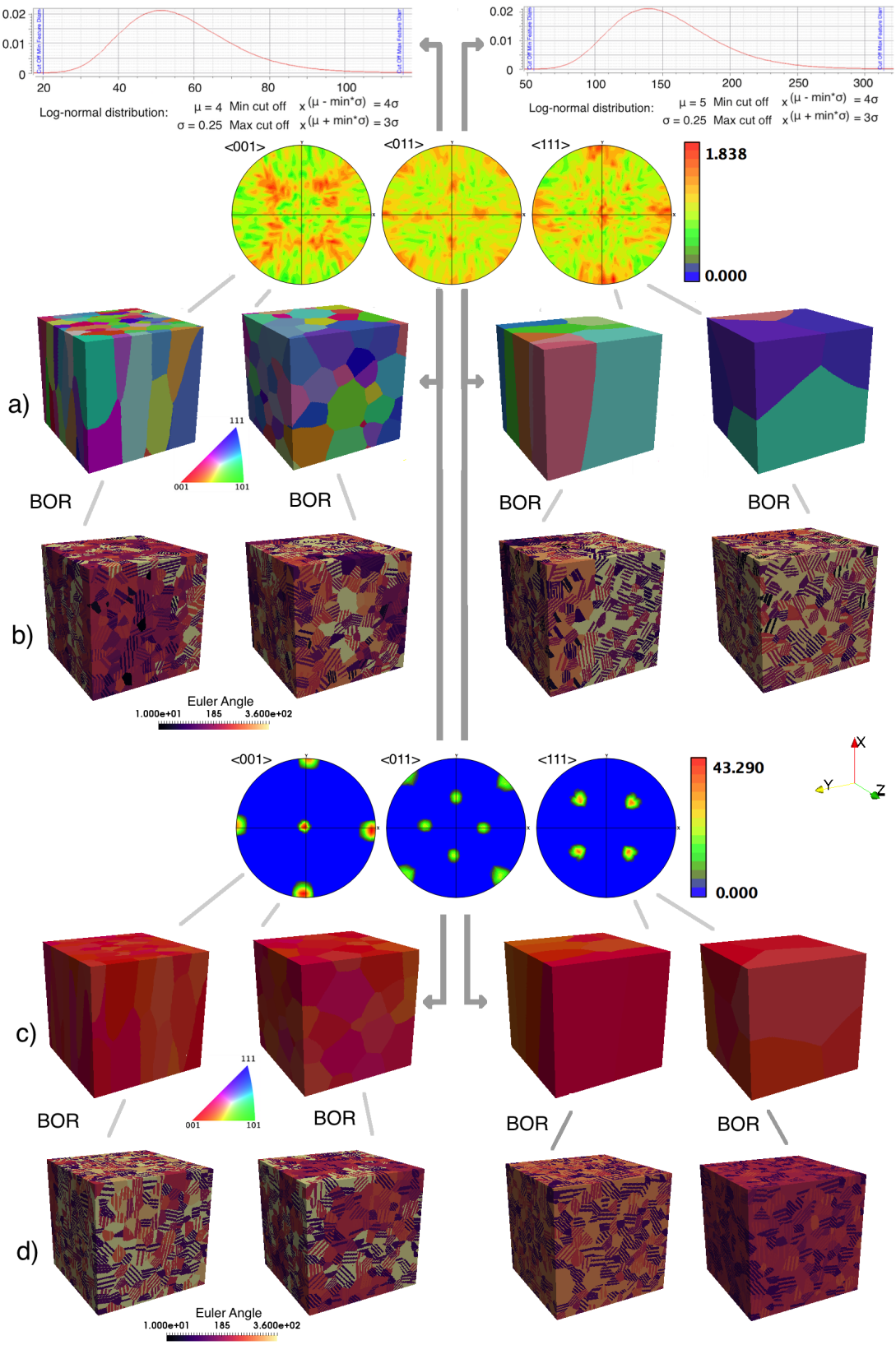

Figure 6.4: Illustration of the synthetic microstructure generation for two different parent prior β grain size distributions, average 50 μm on the left two and average 145 μm on the right two: a) Randomly orientated columnar and equiaxed β parent grains; b) Two phase structure after 50 % α insertion following the BOR; c) (001) textured columnar and equiaxed β parent grains; d) Two phase structure after 50 % α insertion following the BOR.

6.3 Domain Size Sensitivity Analysis Results

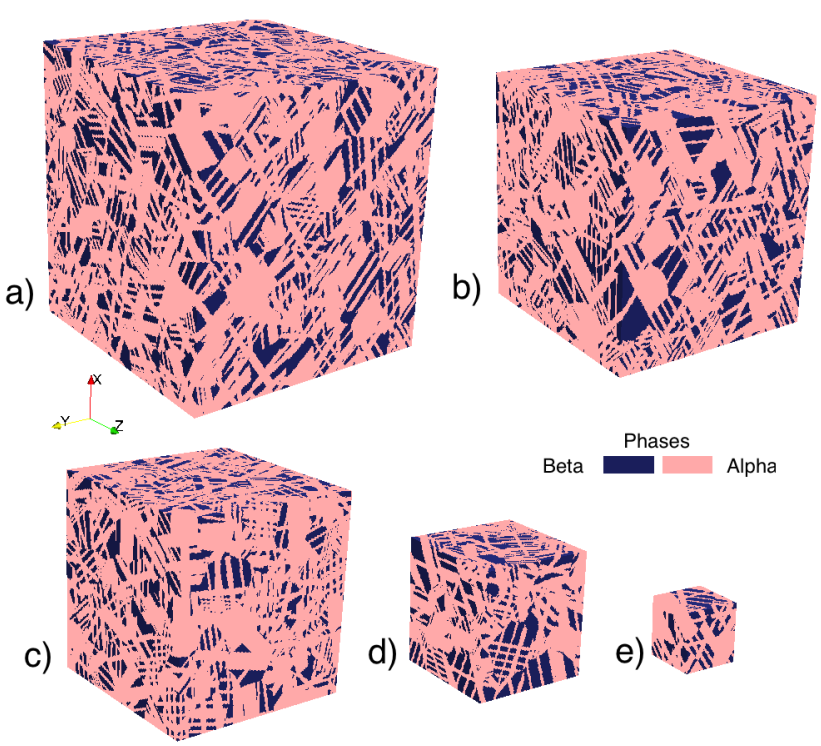

Figure 6.5: Phase maps for generated synthetic 80 α dual-phase microstructures of 256^3, 216^3, 196^3, 128^3 and 64^3 domain sizes.

In the elasto-viscoplastic regime, the deformation is described by a combination of linear (Hooke's law) and non-linear (rate-sensitive approach) relationships. In the elastic regime, the mechanical response is found to be nearly insensitive to the domain size when a few shells of the nearest neighbor grains are included in the simulation [98]. However, it is expected that the non-linear relationship in the plastic regime might cause higher contrast between different cell size domains as a result of n-site non-linear grain interactions. Since large simulations are computationally expensive, it is important to define the smallest statistically representative volume element (SRVE) size without sacrificing the convergence of effective and/or local properties. For instance, the grain size influence on surface roughening has been investigated, revealing an inverse relationship between convergence speed and grain size [144]. It has also been shown that the deviation from the applied strain is more sensitive to grain interactions and less so on grain self-orientation, causing local distribution to be more sensitive to domain size than macroscopic behavior [123]. Since the FFT algorithm calculates homogenized properties from the full-field values, it allows for a thorough domain size sensitivity

study.

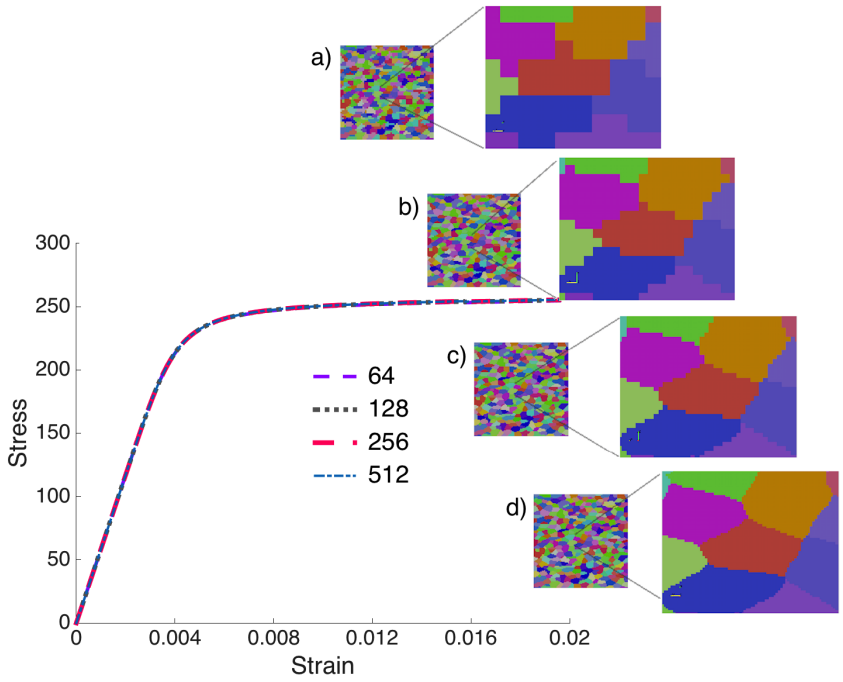

Figure 6.6: Stress-strain curves for similarly deforming randomly oriented equiaxed structures with Fourier point resolution of a) 8 μm/voxel, 64^3 domain; a) 4 μm/voxel, 128^3 domain; c) 2 μm/voxel, 256^3 domain; d) 1 μm/voxel, 512^3 domain.

In choosing a set of microstructures for the domain size analysis, the size of the parent β grains, the lath thickness and fraction of α laths, the orientation distribution and Fourier grid point resolution are all taken into account. Although the modeled field values converge to almost the same values when the grid resolution is changed from 1 μm/voxel to 8 μm/voxel for randomly oriented equiaxed grains, Fig. 6.6, as the lath thickness feature is chosen as 1-2 μm in this study, the Fourier grid point resolution is taken as 1 μm/voxel in all directions. In order to obtain the highest level of microstructural heterogeneity, the parent grain size is chosen as the largest, 145 μm average with columnar morphology, lath thickness is chosen as the thickest, 2 μm average, the daughter fraction is chosen as the highest, 80 %, and the orientation distribution is chosen as random with the expectation that these extreme attributes would result in higher domain size sensitivity.

Using the model parameters listed in Table 6.2, structures were deformed to 5 % strain with combined strain/stress boundary conditions. Note that since the strong phase α fraction is 14 % less than the experimental Ti-6Al-4V data that was used for hardening parameter extraction, the macroscopic field values do not match with Fig. 6.3. Both the local and homogenized values converged at

216^3 simulation size, Fig. 6.7. Hence, 216^3 is chosen to be the SRVE, and all of the microstructures reported in section 6.4 are generated accordingly.

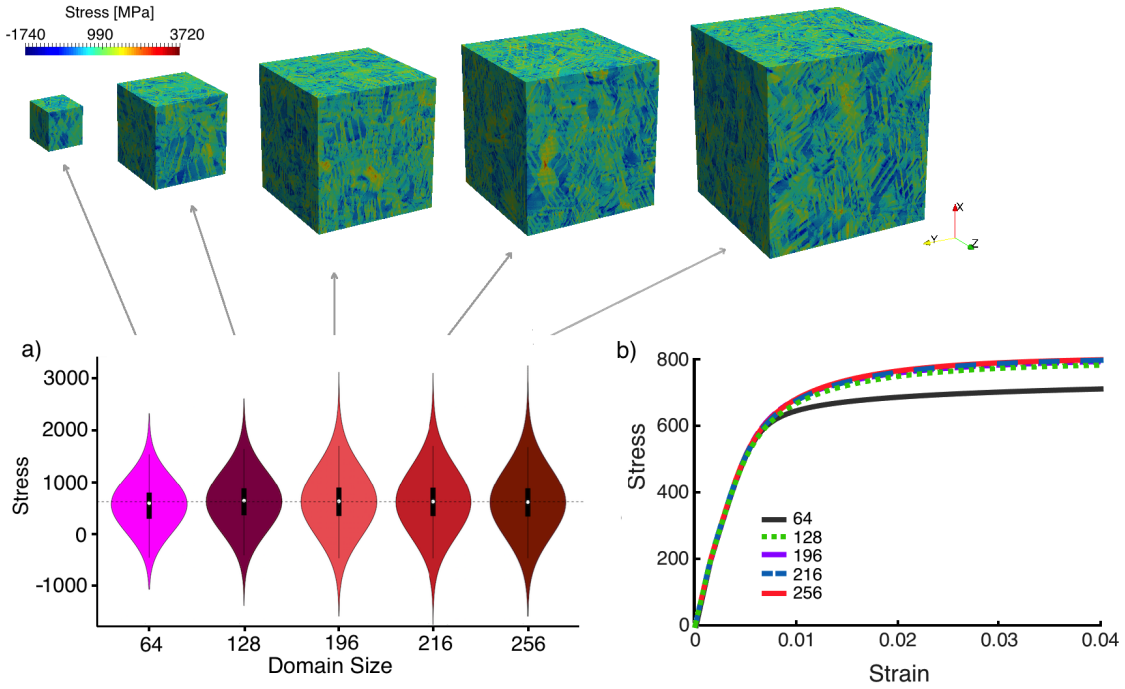

Figure 6.7: Domain size sensitivity analysis using 64^3, 128^3, 196^3, 216^3 and 256^3 microstructures: a) Full-field stress (component along the loading direction) violin plots and stress distributions at 4 % strain for each domain; b) Macroscopic stress-strain curve for each domain.

6.4 Microstructure Sensitivity Analysis Results

In order to investigate the effect of microstructure on mechanical properties, the microscopic and macroscopic fields are simulated for a total of 56 conditions, Fig. 6.8. 36 distinct microstructures with varying prior β grain sizes and morphologies, individual α lath thicknesses and sizes, phase volume fractions, and orientation distributions were generated. Furthermore, the effect of uniaxial loading direction is examined by modeling the response of 20 different Widmanstätten structures for tensile deformation parallel and perpendicular to the long grain axis (axis ODF) direction. Using combined stress/strain boundary conditions, elasto-viscoplastic deformation of the generated microstructure database, Fig. 6.8, was modeled with deformation step increments of 0.0001, up to total 4 % macroscopic tensional strain.

The macroscopic stress-strain response is summarized in Fig. 6.9, where the effect of α fraction for for 50 μm randomly oriented columnar prior β parent structures is shown in Fig. 6.9.a, the effect

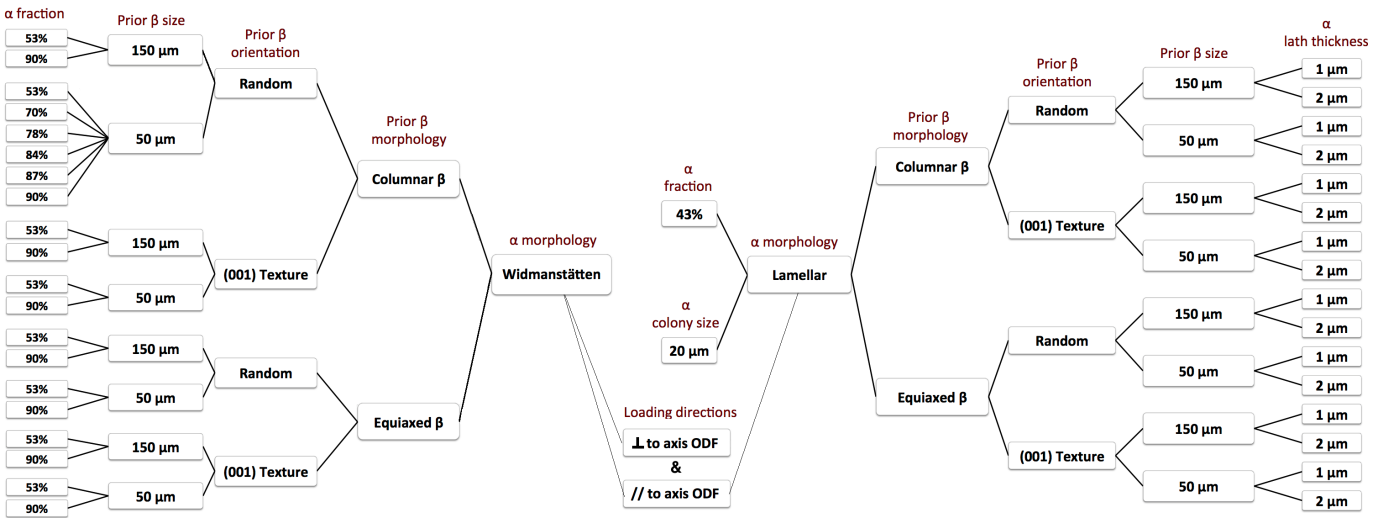

Figure 6.8: Simulated 56 conditions for 36 distinct microstructures with varying prior β grain sizes and morphologies, individual α lath thicknesses and sizes, phase volume fractions, and orientation distributions.

of lath thickness for 150 μm randomly oriented and textured columnar prior β parent structures is shown in Fig. 6.9.b, and the effect of prior β grain size, grain morphology and orientation distribution for 53 % α is shown in Fig. 6.9.c. The response is found to be the most sensitive to α phase fraction and the prior β orientation distribution, such that the increase in α phase enhances the tensile strength, and the increased magnitude of prior β (001) texture decreases the tensile strength. This can be explained by α being the harder phase, and the prior β (001) texture being the soft direction for bcc, with restricted transformed α orientation space as a result of BOR. The phase fraction variability is further investigated by comparing the contribution of each phase against the behavior of dual-phase composite structure, Fig. 6.11, in order to check if the observed alpha fraction effect is simply caused by a larger number of harder phase grains. Phase fraction normalized stress-strain distributions, presented in Fig. 6.10, showed the lack of a master curve for aggregate behavior. Comparing the stress contributions of different phases for 53 %, 78 % and 90 % alpha fraction microstructures, Fig. 6.11.ii showed that the bcc phase is harder in existence of higher alpha fractions, and it carries the strain while the hcp phase carries the stress. This is in agreement with Dawson et al., who demonstrated that the beta phase is the shear strain carrier, which further increases in magnitude with increased alpha volume fraction [59]. Phase separation analysis also showed the near linear individual contribution of the bcc and hcp phases, which deviates from linear rule of mixture for two-phase aggregate response, Fig. 6.11.i. For lower fractions of the

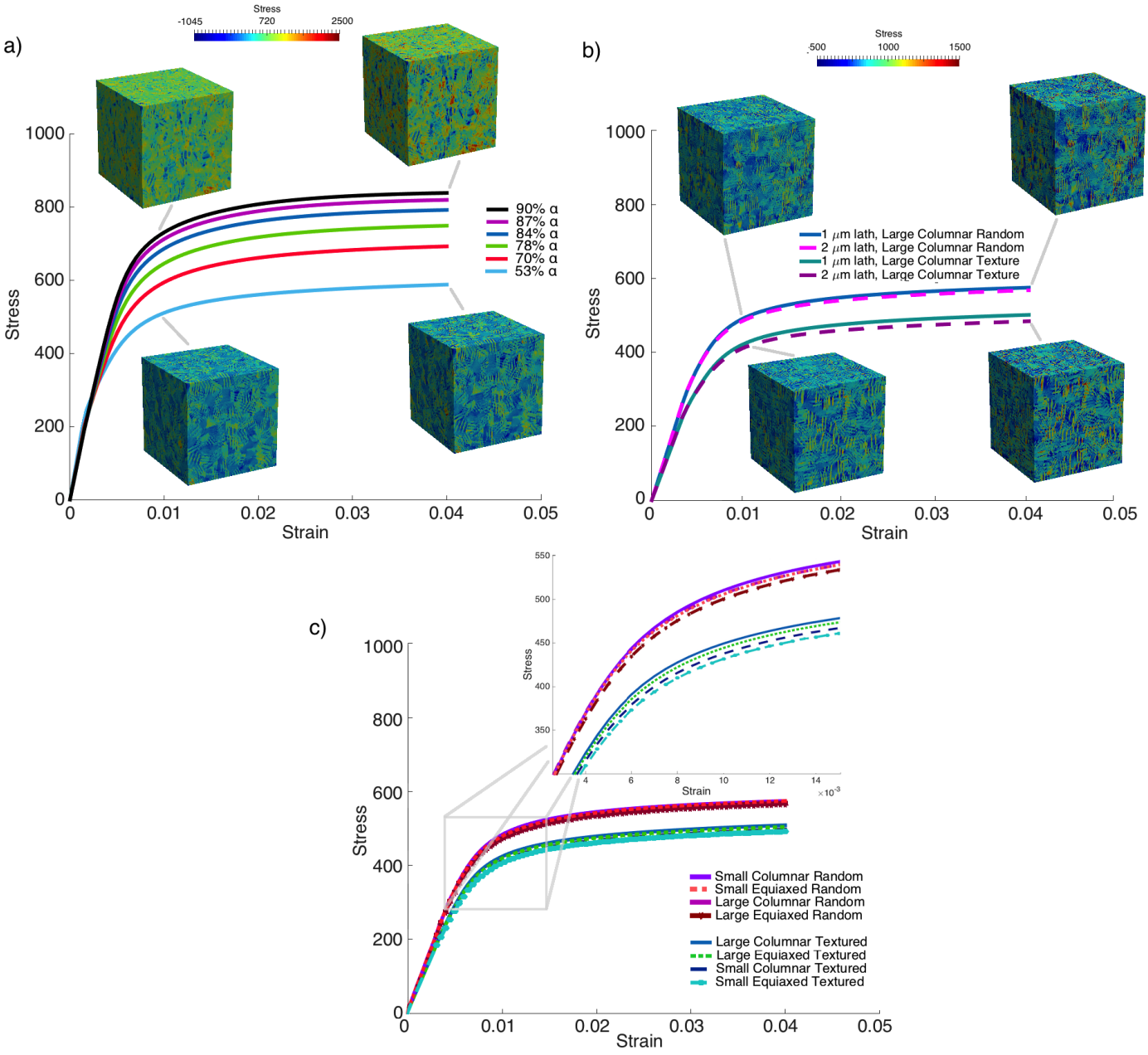

Figure 6.9: Microstructure sensitivity analysis a) Effect of α fraction; comparison shown for 50 μm randomly oriented columnar prior β parent structures; b) Effect of lath thickness; comparison shown for 150 μm randomly oriented and textured columnar prior β parent structures; c) Effect of prior β grain size, grain morphology and orientation distribution; comparison shown for 53 % α Widmanstätten structures.

harder phase, the aggregate response is controlled by both phases, however as the harder phase fraction increases it dominates the behavior and the importance of the softer phase diminishes. In summary, as the fraction of the harder phase is found to affect the behavior of the entire aggregate non-linearly through neighbor interactions, phase fraction is considered a microstructure descriptor

for this study.

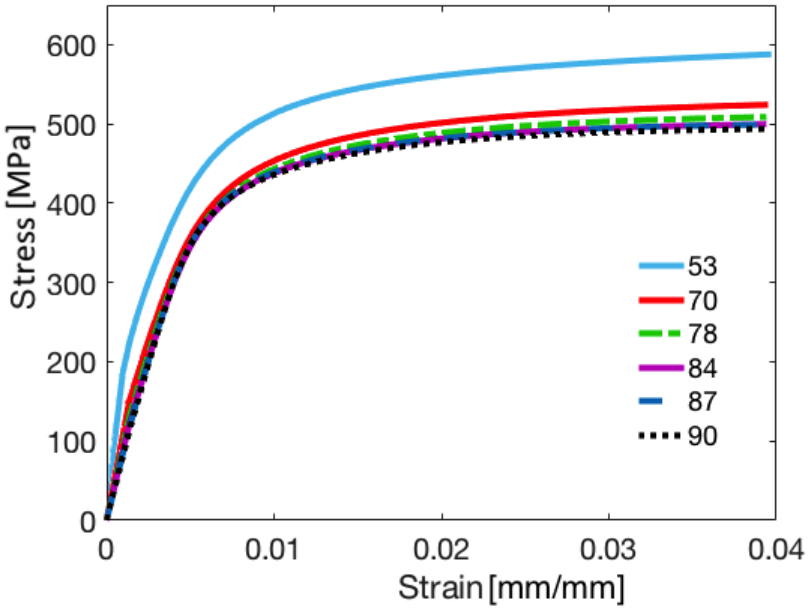

Figure 6.10: Phase fraction normalized von-Mises stress-strain curves, showing the lack of linear rule of mixture

Consistent with the literature, [98], the results in the linear elastic regime indicate an insensitive response to microstructure. However, in the viscoplastic regime, the mechanical behavior is found to be sensitive under all investigated conditions, Fig. 6.9 and Fig. 6.12.

Fig. 6.12 shows the comparison of the local behavior through violin plots of stress components along the loading direction at 4 % strain, for each generated microstructure. The effect of α fraction is depicted in Fig. 6.12.a; for on the x axis 1 denotes loading direction parallel to long grain axis, and 2 denotes loading direction perpendicular to long grain axis. The effect of prior β grain size, grain morphology and orientation distribution is depicted in Fig. 6.12.b; for on the x axis 1 denotes 53 % α fraction and loading direction parallel to long grain axis, 2 denotes 53 % α fraction and loading direction perpendicular to long grain axis, 3 denotes 90 % α fraction and loading direction parallel to long grain axis, and 4 denotes 90 % α fraction and loading direction perpendicular to long grain axis. The effect of lath thickness is depicted in Fig. 6.12.c; for on the x axis 1 denotes α lath thickness of 1 μm, and 2 denotes α lath thickness of 2 μm. The results for both these local, Fig. 6.12 and the macroscopic, Fig. 6.9 responses can be summarized as:

i) Effect of α fraction: Being the harder phase of two, increase in α fraction increases the tensile strength, Fig. 6.9.a.

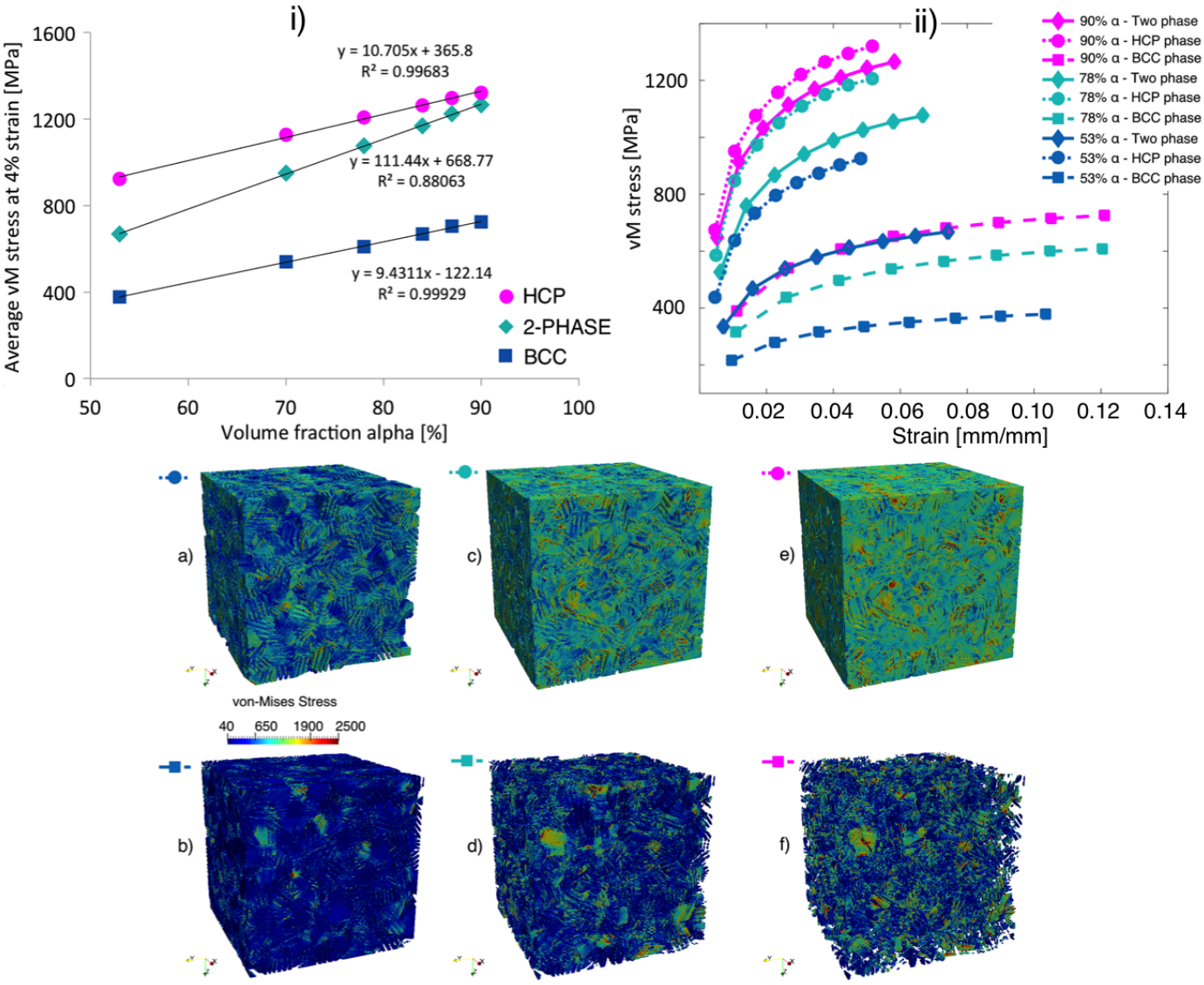

Figure 6.11: Average von-Mises stresses carried by the aggregate, bcc and hcp phases as a function of the alpha phase fraction on the left, and stress-strain curves for the aggregate, bcc and hcp phases with different α fractions on the right. Microstructures a-b) von-Mises stress distributions of the hcp and bcc phases for the 53 % α case, c-d) von-Mises stress distributions of the hcp and bcc phases for the 78 % α case, e-f) von-Mises stress distributions of the hcp and bcc phases for the 90 % α case.

ii) Effect of prior β size: For randomly orientated prior β grains, decrease in prior β size increases the tensile strength very slightly. However, as the epitaxial texture strength of the prior β increases, a direct grain size dependence is observed where increase in prior β size increases the tensile strength, both for columnar and equiaxed β morphologies, 6.9.c.

iii) Effect of prior β morphology: Columnar prior β morphology results in a higher yield point and tensile strength as compared to equiaxed grains. The magnitude of difference is found

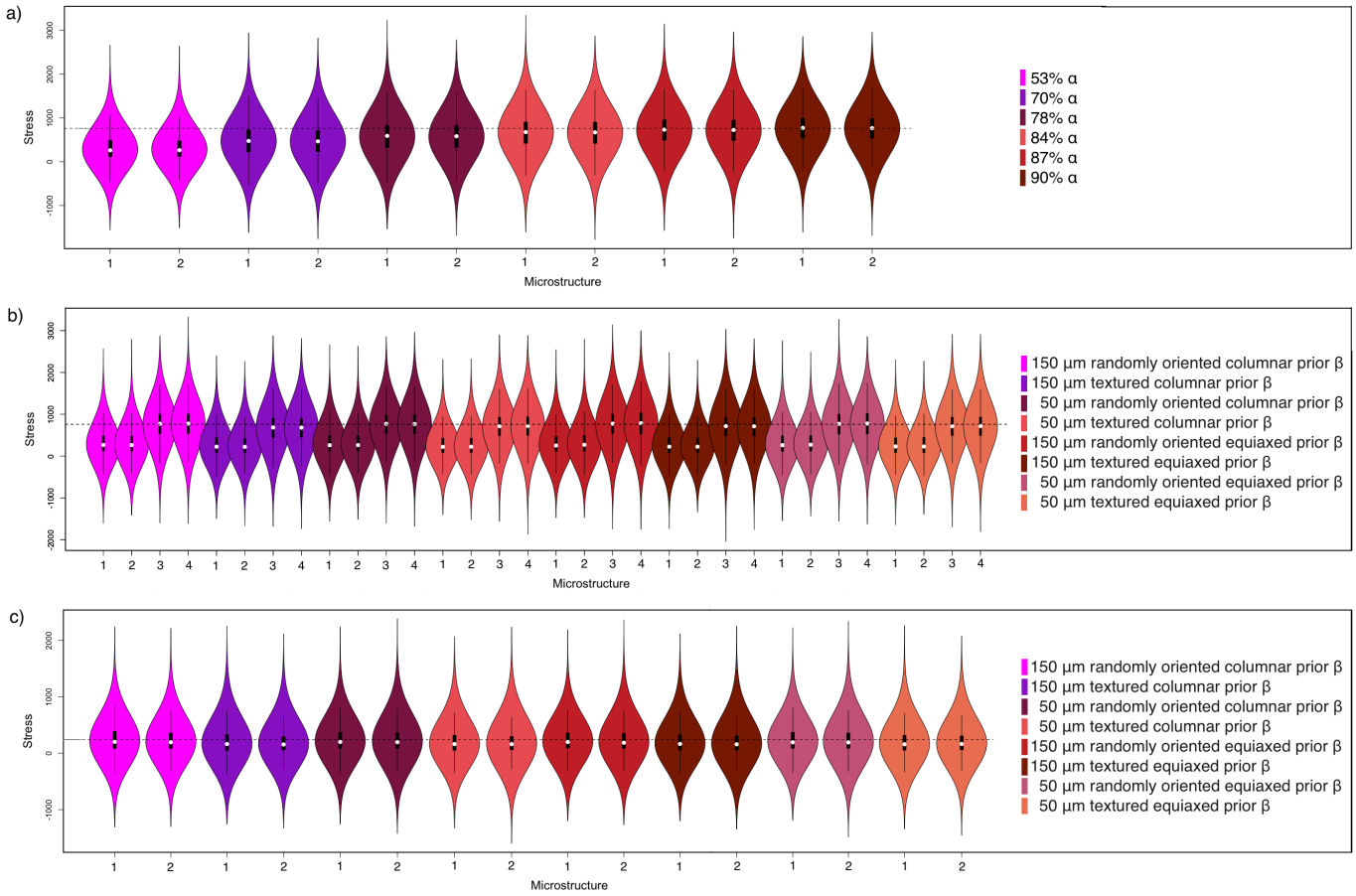

Figure 6.12: Violin plots of stress components along the loading direction at 4 % strain, for each generated microstructure. a) Effect of α fraction for 50 μm randomly oriented columnar prior β parent structures. On the x axis, 1 denotes loading direction parallel to long grain axis, 2 denotes loading direction perpendicular to long grain axis; b) Effect of prior β grain size, grain morphology and orientation distribution. On the x axis, 1 denotes 53 % α fraction and loading direction parallel to long grain axis, 2 denotes 53 % α fraction and loading direction perpendicular to long grain axis, 3 denotes 90 % α fraction and loading direction parallel to long grain axis, 4 denotes 90 % α fraction and loading direction perpendicular to long grain axis; c) Effect of lath thickness. On the x axis, 1 denotes α lath thickness of 1 μm, 2 denotes α lath thickness of 2 μm.

to increase in existence of texture, i.e. difference between columnar grains with (001) texture and equiaxed grains with (001) texture are higher as compared to the difference between their randomly oriented counterparts, 6.9.c.

v) Effect of lath thickness: Increase in α lath thickness decreases the tensile strength 6.9.b. Existence of (001) texture intensifies the effect of lath thickness.

vi) Effect of loading direction: Deformation parallel to long grain axis (axis ODF), which is also the direction of texture fiber, gives marginally higher stress values than texture perpendicular deformation, 6.12.a. However, the effect of loading direction has the least influence on the behavior

when compared with the effect of other descriptors.

iv) Effect of prior β orientation: Increase in (001) fiber texture strength decreases the tensile strength, both for when deformation is parallel and perpendicular to the texture fiber direction, 6.9.c. Although (001) fiber causes a weaker mechanical response, it enhances the effect of other microstructures features for all of the examined conditions, e.g., difference in stress values of columnar vs. equiaxed prior β structures that are randomly oriented or textured, difference in 1μm vs. 2 μm α lath thickness transformed from randomly oriented or textured prior β etc.

6.5 Discussion

The studies carried out have established that a computational approach of concurrent synthetic microstructure generation and micromechanical modeling is useful for investigation of microstructure-deformation relationships in polyphase polycrystalline materials. The sensitivity of mechanical properties to several types of microstructural feature can be quantified. Furthermore, the virtual microstructure database that was generated, combined with the corresponding micro-mechanical data, can be utilized by others for designing new process maps and material systems for additive manufacturing when a particular set of properties are targeted.

In more detail, the spectral full-field FFT based modeling technique was used to quantify partitioning of stress and strain between the harder hcp α phase and softer bcc β phase. Relationships were determined between the alpha fraction/morphology/size, β morphology/size/orientation, loading direction, and the resulting mechanical response in the generated two-phase structures. Some of the results agreed with previous work [2, 6, 15, 16, 38] such that;

1. The response was the most sensitive to the alpha fraction and prior β texture;

2. Increase in α phase enhanced the tensile strength, as the low temperature α phase is harder than the high temperature β phase;

3. Increased magnitude of prior β (001) texture decreased the tensile strength. This can be explained by the prior β (001) texture being the soft direction for the bcc phase;

4. When α phase was present in lamellar configuration, it dominated the behavior. This amplified the effect of α lath thickness as being inversely related to the tensile strength due to

decreased slip length;

5. Columnar prior β grains resulted in higher tensile strength as compared to equiaxed grains.

On the other hand, the result on the effect of prior β grain size was not in full agreement with Lutjering's ductility-prior β grain size relationship theory; that proposes the length of the β size as grain boundary α slip length limiting factor, causing reduced stress concentrations for small β grain sizes, higher ductility and lower tensile strength [2, 6]. With the utilized rate-sensitive crystal plasticity constitutive equation and the hardening model, a reversed effect is observed for random vs. textured β grains; for the random texture case, the tensile strength increased very slightly (almost negligible) with decreased grain size, whereas for the textured case the tensile strength decreased with decreased grain size. The disagreement with literature for randomly oriented prior β case is attributed to the simplicity of the utilized hardening model, where the slip system resistance is not explicitly modified to implement a grain size effect.

CHAPTER VII

Conclusions and Future Work

7.1 Conclusions

In the present work, the microstructure-mechanical property relationship of polycrystalline materials, specifically additively manufactured titanium alloys is investigated by integrated computational and experimental approaches. Adoption of a combined workflow of computational and experimental approaches constituted a unique and robust interdisciplinary materials-physics-mechanics study. As one of the first teams that utilized synchrotron based high-energy X-Ray diffraction techniques for high throughput 3D orientation mapping, we were able to non-destructively capture the effects of build height, process parameters and heat treatment on the resulting microstructure (grain structure, porosity and full-field orientation distribution) of the spatially heterogeneous additively manufactured titanium alloys by successfully pushing the reconstruction and resolution limits of the technique. With the HEDM measurements, we obtained large area orientation measurements that showed the bi-modal size and morphology distributions within the parts, in which the alpha structure can be found in colonized or fine basketweave forms depending on the build height. Furthermore, shared diffraction peaks between alpha (HCP) and beta (BCC) phases, where the (001) diffraction of HCP phase overlaps with (110) diffraction of BCC phase, and (114) diffraction of HCP phase overlaps with (222) diffraction of BCC phase, allowed to reconstruct the prior beta grains by providing enough confidence in fitting the orientation of the cubic phase. The comparisons between the HEDM "pseudo-data" reconstructions and back reconstruction algorithm calculations revealed a significant degree of agreement.

Macroscopic mechanical property measurements revealed a large scatter of properties outside of the natural scatter expectations of tensile tests. First order linear regression analysis of build

height averaged properties showed a weak trend of increasing strength with increased build height. High and low magnification OM micrographs revealed increased prior beta and decreased alpha lath sizes with build height, which are shown to effect the properties by an inverse Hall-Petch and direct Hall-Petch relations. A second order statistical analysis is performed to include the within group variations in the mean, and the modulus, elongation and yield stress is found to be insignificantly affected by build height, and UTS is found just barely significant. So, while the tensile test results were shown to be heterogeneous in relation to build height, the results were inconclusive for finding trends.

Based on the experimental results, the first part of the hypothesis, which was

i) Multi-modal microstructure characterization and mechanical behavior measurements are expected to reveal the heterogeneous microstructure and properties along the build height of powder bed based electron beam melting Ti-6Al-4V parts. Due to expected larger alpha platelets at the top of the build [16, 17] decreased yield and tensile strength and increased elongation is anticipated in relation to build direction. In extracting the location specific material hardening parameters from the tensile stress-strain curves, the Voce hardening model is expected predict the behavior with less than 10 % error based on the work by Gockel [14]. is modified to

i) While the multi-modal microstructure characterization reveals trends microstructure along the build height of powder bed based electron beam melting Ti-6Al-4V parts, i.e. decreased alpha colony fraction with distance from the top, the mechanical properties show statistically insignificant relationship between distance from the build plate and the tensile properties. Despite the large variability in the tensile data, if the Voce parameters are extracted from the experimental values, location specific mechanical behavior can be predicted with less than 10 % error using the VPSC model.

Fast Fourier Transform based algorithm is investigated as a computationally efficient micromechanical modeling technique by first determining a minimum simulation size through a sensitivity study, and then based on the results establishing and testing a methodology to create statistically representative dual phase microstructures, specifically additively fabricated Ti-6Al-4V representative structures to study the microstructure-deformation relationship.

The simulation domain size requirement study showed that in terms of neighborhood sensitivity, elastic response<elasto-viscoplastic response<viscoplastic response, because as the contrast of

properties (e.g., texture, field localization, anisotropy, rate-sensitivity) increases, so does the minimum simulation domain size requirement. Regardless, in all deformation regimes a minimum SVE could be defined giving pearson correlation coefficient r $\geqslant$ 0.99 when the local field value are compared to larger simulations. Specific to the LSHR microstructure, minimum requirement for convergence is found as 356 total grains in a grid of size 81x81x64 in the elastic and 3114 total grains in a grid of size 256x256x64 in the viscoplastic and elasto-viscoplastic regimes. Results of the domain size and Fourier grid resolution sensitivity studies supported the second part of the thesis hypothesis, which was

For the elastic, viscoplastic and elasto-viscoplastic FFT solutions, finding a Pearson correlation coefficient r = 0.99 is anticipated when the downsampled simulation results are compared to one another and the largest sized domain

By a computational approach of concurrent synthetic microstructure generation and micromechanical modeling, microstructure-deformation relationship in dual-phase AM representative titanium materials is established. For microstructures with varying crystal phase fractions, grain sizes/morphologies and orientation distributions, the response is found to be the most sensitive to the alpha fraction and prior beta texture. Modeled deformation showed negligible sensitivity to the prior beta grain size and morphology due to the simplicity of the utilized hardening model. Results on the microstructure/property investigation of multi phase systems partially support the last part of the thesis hypothesis; which was

iii) Being a spectral, image-based, meshless full-field deformation modeling tool, FFT is expected to be able to simulate the large element count and correspondingly large number of degrees of freedom (DOF) two-phase lamellar structures of > 100 parent grain + > 50000 daughter grain composites, and to predict the stress-strain behavior by capturing the relative contribution from varying microstructural features such as phase fractions and texture on both the macroscale effective and mesoscale spatial properties.

As the anticipated prior beta size and morphology effect was not captured with Voce hardening, the hypothesis is modified to

iii) Being a spectral, image-based, meshless full-field deformation modeling tool, FFT based model can simulate the large element count and correspondingly large number of degrees of freedom (DOF) two-phase lamellar structures of > 100 parent grain + > 50000 daughter grain com-

posites, and predict the stress-strain behavior by capturing the relative contribution from varying microstructural features when the model is modified to include the effect of grain size and shape.

7.2 Future Work

The following future work can provide new insights on the experimental and computational microstructure-mechanical deformation relationship investigation of additively manufactured titanium.

1. FFT modeling of the measured HEDM microstructures using the optimized Voce parameters.
2. Introducing a 'prior beta factor' to the elasto-viscoplastic model, in order to more appropriately capture the effect of grain size and morphology. This can be accomplished by evolution of slip resistance in accordance with the apparent grain size seen by active slip systems in the grain (e.g., implementing grain size dependence for each individual active slip system).
3. Introducing a global grain size effect term to the elasto-viscoplastic model.
4. Adding grain boundary alpha generation capabilities to the synthetic microstructure reconstruction algorithm, as grain boundary alpha thickness is shown to play an important role in mechanical properties.
5. Extending the second order statistical analysis that was performed on the tensile data, by using non-parametric methods in assessing the difference of means, especially for the yield stress measurements.
6. Performing tensile tests at different strain rates, and also on annealed samples towards extending the AM Ti-6Al-4V process-structure-property database.
7. Fractography on the tensile specimens, in order to check the existence of unmelted powder regions and pores on the fracture surface.
8. Comparing the HEDM orientation maps with EBSD data collected from the same samples, in order to check the reliability of the reconstruction when the diffraction data is near the resolution limit of the technique.

APPENDIX A

Statistical Analysis of the Measured Tensile Properties

The one-way between subjects ANOVA study, mentioned in Chap. 4.2, is detailed in this section by the SPSS report. The report is formatted to include Levene's test of equality of error variances, ANOVA test results, and measurement mean reports on a single page for yield stress, tensile stress, modulus and elongation. The report then continues with the statistical exploration of all measured tensile properties with presented profile plots. For one-way ANOVA to be valid, measurements must have a normal distribution, and groups should have equal variances, which is tested by the reported Levene's test of equality of error variances ($p<0.05$ means the variances are not equal as there is significant error). Levene's test showed that the modulus variances were not equal, and UTS variance was right at the edge of being equal. For the current work, one-way ANOVA was still conducted despite lack of modulus variance equality to keep the consistency of the study, however a non parametric method is suggested for assessing the difference of means for future analysis.

In summary, elastic modulus [$F(12,26) = 1.235$, $p=0.313$], elongation [$F(12,26) = 1.239$, $p=0.310$] and yield stress [$F(12,26) = 1.810$, $p=0.100$] do not appear to be significantly affected by build height, whereas the ultimate tensile stress [$F(12,26) = 2.127$, $p=0.052$] shows a marginal trend toward significance.

Table A.1: The one-way between subjects ANOVA SPSS report for measured tensile data.

Yield Stress:

CRITERIA = ALPHA (0.05)

Levene's Test of Equality of Error Variances[a]

F-value	DOF1	DOF2	p-value
1.281	12	26	.287

Tests the null hypothesis that the error variance of the dependent variable is equal across groups.[a]

a. Design: Intercept + Distance From Build Plate

Between-Subjects (N=3) Anova Test Results

Source	DOF	Mean Square	F-value	p-value
Corrected Model	12	3367.021	1.810	.100
Intercept	1	25805440.410	13875.232	.000
Error	26	1859.821		
Total	39			
Corrected Total	38			

Yield Stress Means

Distance from Build Plate	Mean	Std. Deviation	Std. Error	95% Confidence Interval	
				Lower Bound	Upper Bound
1	780.333	72.113	24.899	729.154	831.513
2	787.667	46.361	24.899	736.487	838.846
3	771.333	25.929	24.899	720.154	822.513
4	829.333	42.736	24.899	778.154	880.513
5	779.333	45.004	24.899	728.154	830.513
6	794.000	53.507	24.899	742.820	845.180
7	796.000	19.000	24.899	744.820	847.180
8	801.000	20.518	24.899	749.820	852.180
9	837.667	29.484	24.899	786.487	888.846
10	851.000	20.809	24.899	799.820	902.180
11	826.333	25.146	24.899	775.154	877.513
12	836.667	35.162	24.899	785.487	887.846
13	884.000	74.081	24.899	832.820	935.180

Ultimate Tensile Stress:

CRITERIA = ALPHA (0.05)

Levene's Test of Equality of Error Variances[a]

F-value	DOF1	DOF2	p-value
2.170	12	26	.048

Tests the null hypothesis that the error variance of the dependent variable is equal across groups.[a]

a. Design: Intercept + Distance From Build Plate

Between-Subjects (N=3) Anova Test Results

Source	DOF	Mean Square	F-value	p-value
Corrected Model	12	3156.541	2.127	.052
Intercept	1	33013433.450	22249.362	.000
Error	26	1483.792		
Total	39			
Corrected Total	38			

Ultimate Tensile Stress Means

Distance from Build Plate	Mean	Std. Deviation	Std. Error	95% Confidence Interval	
				Lower Bound	Upper Bound
1	884.610	77.347	22.240	838.896	930.324
2	895.244	47.306	22.240	849.530	940.958
3	882.149	30.662	22.240	836.435	927.863
4	944.030	24.779	22.240	898.316	989.744
5	892.998	30.892	22.240	847.284	938.712
6	909.748	38.584	22.240	864.033	955.462
7	898.904	7.227	22.240	853.190	944.618
8	899.657	12.378	22.240	853.943	945.371
9	940.102	21.600	22.240	894.388	985.816
10	952.420	21.510	22.240	906.706	998.134
11	929.481	15.398	22.240	883.767	975.195
12	939.792	22.398	22.240	894.078	985.506
13	991.560	72.096	22.240	945.846	1037.274

Modulus:

CRITERIA = ALPHA (0.05)

Levene's Test of Equality of Error Variances[a]

F-value	DOF1	DOF2	p-value
2.956	12	26	.010

Tests the null hypothesis that the error variance of the dependent variable is equal across groups.[a]

a. Design: Intercept + Distance From Build Plate

Between-Subjects (N=3) Anova Test Results

Source	DOF	Mean Square	F-value	p-value
Corrected Model	12	11739085.3	1.235	**.313**
Intercept	1	509968659500.0	53670.717	.000
Error	26	9501804.4		
Total	39			
Corrected Total	38			

Modulus Means

Distance from Build Plate	Mean	Std. Deviation	Std. Error	95% Confidence Interval	
				Lower Bound	Upper Bound
1	111400.313	3503.28552	1779.682	107742.124	115058.502
2	114051.096	313.86052	1779.682	110392.907	117709.284
3	114277.810	1446.02997	1779.682	110619.621	117935.999
4	115382.354	1078.42474	1779.682	111724.165	119040.542
5	116654.612	2998.62383	1779.682	112996.424	120312.801
6	114932.967	488.51988	1779.682	111274.778	118591.155
7	114854.279	300.71760	1779.682	111196.090	118512.467
8	113357.839	1296.42955	1779.682	109699.650	117016.027
9	113100.510	4050.39138	1779.682	109442.321	116758.698
10	113790.011	826.14893	1779.682	110131.823	117448.200
11	113752.666	2205.03262	1779.682	110094.477	117410.855
12	111945.740	1291.82607	1779.682	108287.552	115603.929
13	119061.001	8560.21049	1779.682	115402.812	122719.190

Elongation:

CRITERIA = ALPHA (0.05)

Levene's Test of Equality of Error Variances[a]

F-value	DOF1	DOF2	p-value
1.443	12	26	.210

Tests the null hypothesis that the error variance of the dependent variable is equal across groups.[a]

a. Design: Intercept + Distance From Build Plate

Between-Subjects (N=3) Anova Test Results

Source	DOF	Mean Square	F-value	p-value
Corrected Model	12	.000	1.239	.310
Intercept	1	.760	4203.821	.000
Error	26	.000		
Total	39			
Corrected Total	38			

Elongation Means

Distance from Build Plate	Mean	Std. Deviation	Std. Error	95% Confidence Interval	
				Lower Bound	Upper Bound
1	.121	.0162271	.008	.105	.137
2	.151	.0175216	.008	.135	.166
3	.143	.0036928	.008	.127	.159
4	.142	.0052924	.008	.126	.158
5	.144	.0153483	.008	.128	.160
6	.146	.0113106	.008	.130	.162
7	.144	.0136624	.008	.128	.160
8	.135	.0094769	.008	.119	.151
9	.149	.0184571	.008	.133	.165
10	.139	.0098081	.008	.123	.155
11	.132	.0205127	.008	.116	.148
12	.142	.0146313	.008	.126	.158
13	.127	.0052423	.008	.111	.143

Statistical Exploration of All Measured Tensile Properties

CRITERIA = ALPHA (0.05)

			Statistic	Std. Error
Modulus	Mean		114350.8613	511.61670
	95% Confidence Interval for Mean	Lower Bound	113315.1474	
		Upper Bound	115386.5751	
	Median		114340.2991	
	Variance		10208314.170	
	Std. Deviation		3195.04525	
	Minimum		107752.51	
	Maximum		127364.83	
	Range		19612.32	
	Interquartile Range		2368.92	
	Skewness		1.607	.378
	Kurtosis		6.849	.741
Elongation	Mean		.139623	.0022334
	95% Confidence Interval for Mean	Lower Bound	.135102	
		Upper Bound	.144144	
	Median		.141065	
	Variance		.000	
	Std. Deviation		.0139475	
	Minimum		.1028	
	Maximum		.1699	
	Range		.0671	
	Interquartile Range		.0206	
	Skewness		-.073	.378
	Kurtosis		.375	.741
Yield	Mean		813.44	7.739
	95% Confidence Interval for Mean	Lower Bound	797.77	
		Upper Bound	829.10	
	Median		812.00	
	Variance		2335.779	
	Std. Deviation		48.330	
	Minimum		706	
	Maximum		960	
	Range		254	
	Interquartile Range		69	
	Skewness		.350	.378
	Kurtosis		1.106	.741

UTS	Mean		920.0534	7.18265
	95% Confidence Interval for Mean	Lower Bound	905.5129	
		Upper Bound	934.5939	
	5% Trimmed Mean		919.5641	
	Median		915.5762	
	Variance		2012.029	
	Std. Deviation		44.85564	
	Minimum		799.48	
	Maximum		1067.68	
	Range		268.19	
	Interquartile Range		55.51	
	Skewness		.341	.378
	Kurtosis		2.822	.741

Tests of Normality

CRITERIA = ALPHA (0.05)

	Kolmogorov-Smirnov[a]			Shapiro-Wilk		
	Statistic	DOF	p-value	Statistic	DOF	p-value
Modulus	.187	39	.001	.841	39	.000
Elongation	.061	39	.200*	.987	39	.931
Yield	.067	39	.200*	.976	39	.547
UTS	.115	39	.200*	.948	39	.068

* This is a lower bound of the true significance.

a. Lilliefors Significance Correction

Yield Stress Profile Plots

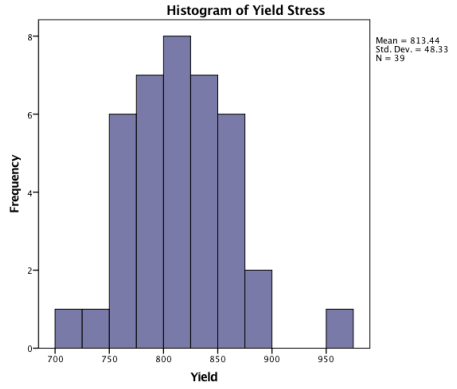

a)

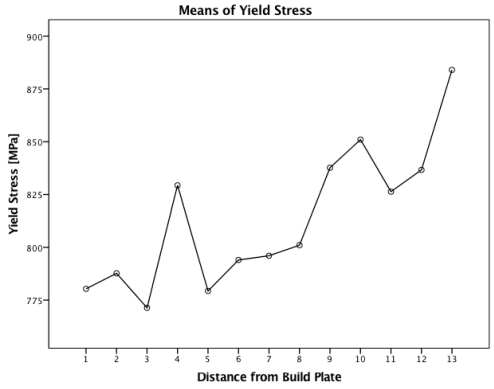

b)

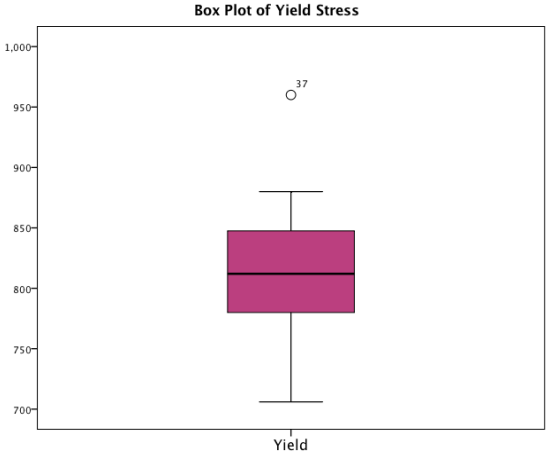

c)

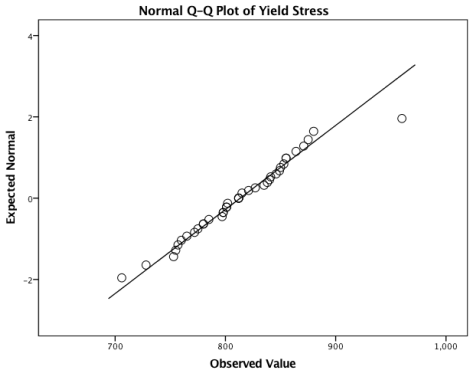

d)

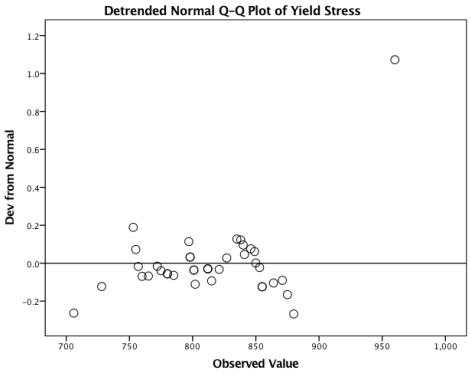

e)

Ultimate Tensile Stress (UTS) Profile Plots

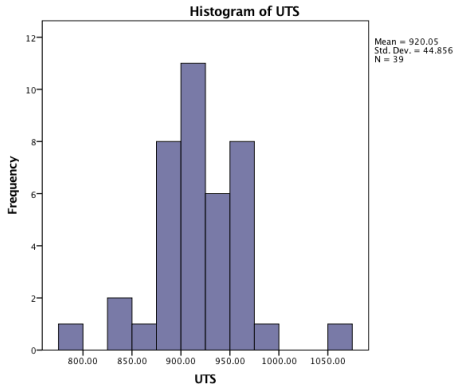

a)

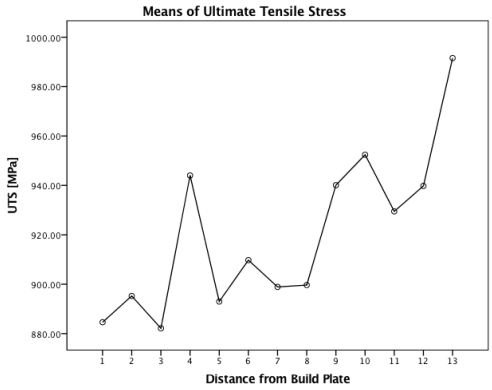

b)

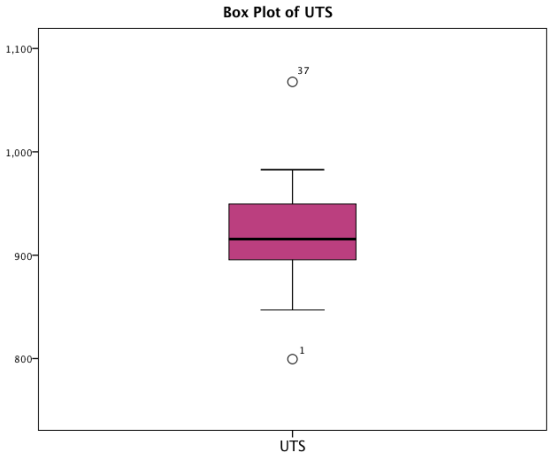

c)

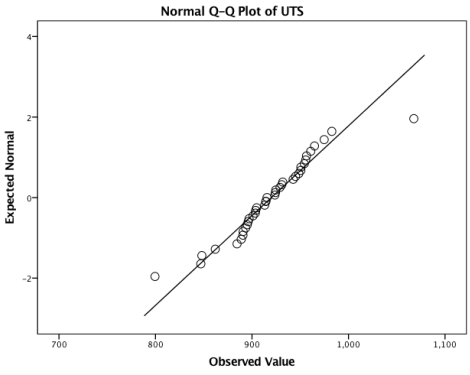

d)

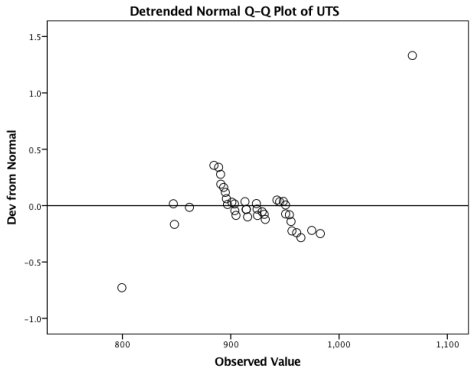

e)

Modulus Profile Plots

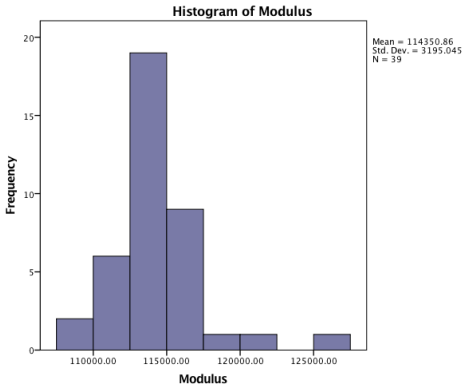

a)

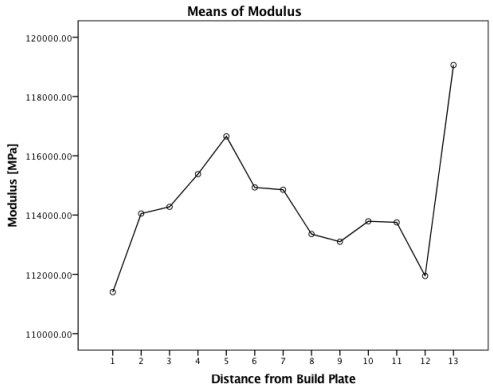

b)

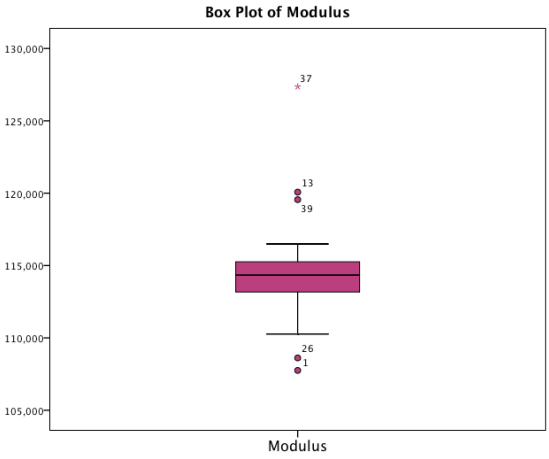

c)

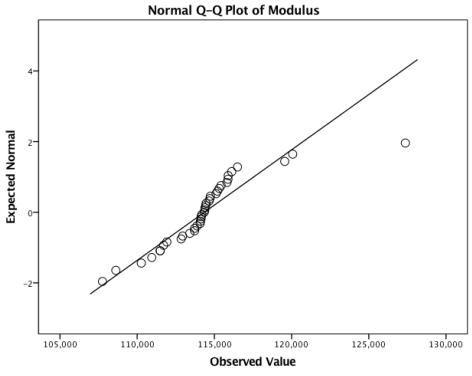

d)

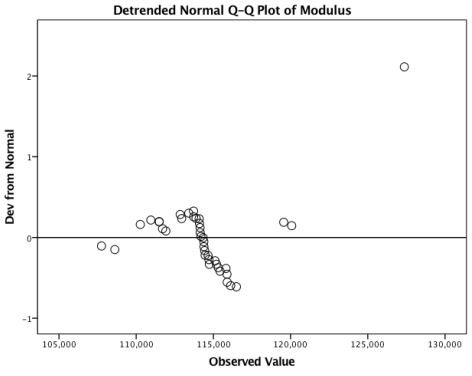

e)

Elongation Profile Plots

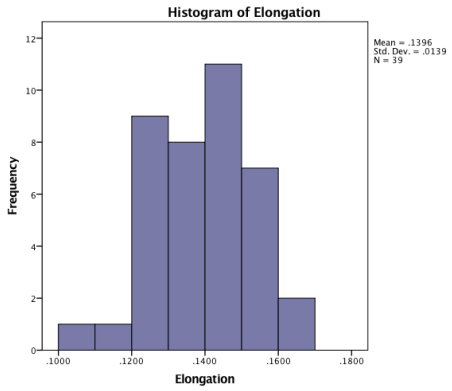

a)

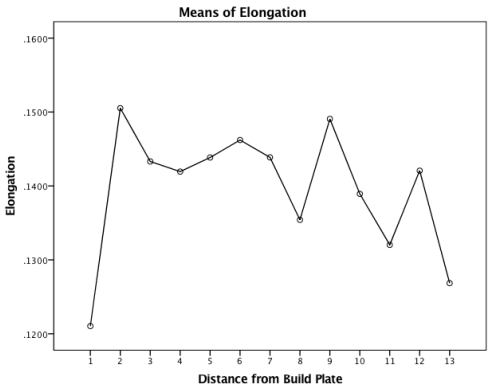

b)

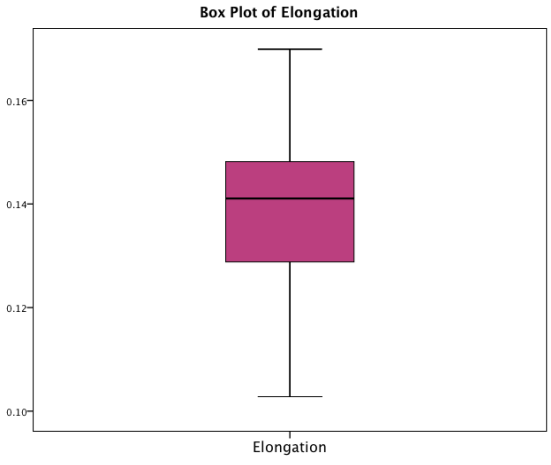

c)

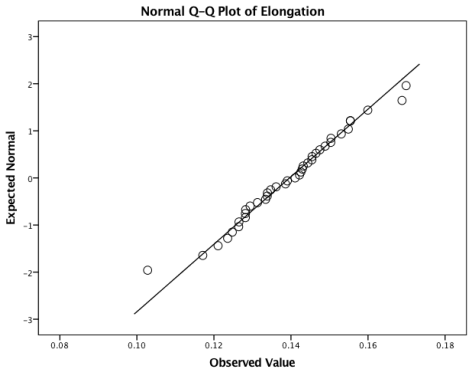

d)

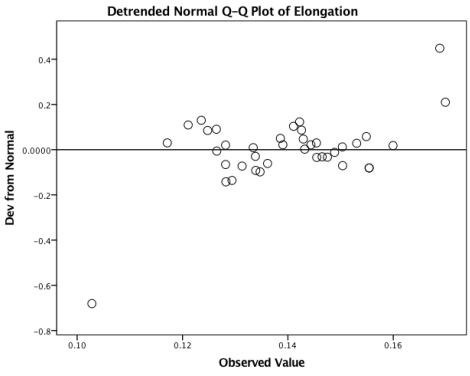

e)

APPENDIX B

Optimized Voce Parameters for Two Phase Behavior

Described in Chap. 4.2, in order to show the extend of data variability and to provide the fit Voce parameters that are optimized from the plastic regime stress-strain curves of additively manufactured Ti, which is rarely found in literature as most of the reported data is in the form of tensile property values, the results of the VPSC parameter calibration study is provided in the Table B.1.

Table B.1: Full list of optimized Voce parameters for BCC slip systems and HCP basal slip system

Sample from bottom	BCC				HCP				% error
	τ_0	τ_1	θ_0	θ_1	τ_0	τ_1	θ_0	θ_0	
1.a	228.676	99.9689	322.364	14.8734	268.806	200.541	701.978	-499.062	3.93977
1.b	255.628	60.6898	45.7228	15.7071	326.806	121.816	765.791	-181.292	3.47937
1.c	311.627	53.6513	40.5835	15.0355	294.162	126.047	928.587	-180.136	6.06574
2.a	173.194	70.1569	45.9253	16.2235	300.487	146.674	610.009	-274.435	3.53492
2.b	132.13	99.1229	170.705	24.9986	346.238	235.564	513.537	-482.354	6.16931
2.c	215.652	53.8544	309.064	8.7276	297.139	120.248	920.577	-165.195	6.3578
3.a	220.206	43.6695	25.8413	2.34296	289.151	85.7775	777.491	-85.6036	2.40214
3.b	0.00148	48.5094	483.823	1.33899	352.598	205.194	581.848	-427.042	3.52286
3.c	196.673	53.7009	29.9961	7.81531	296.456	127.095	1046.02	-167.675	6.4951
4.a	224.554	99.7225	215.77	23.4952	335.583	229.043	630.826	-499.986	5.29046
4.b	656.864	79.3277	326.815	27.4075	311.698	152.117	583.051	-222.679	5.00584
4.c	611.258	90.5537	296.105	26.1265	284.129	144.593	790.277	-202.796	6.2379
5.a	253.372	98.7907	30.029	12.9172	307.241	140.253	668.768	-240.044	3.48389
5.b	629.956	18.6147	78.8389	41.4436	293.302	100.552	722.918	-99.6775	4.15888
5.c	680.836	69.3265	488.034	8.40542	261.969	104.021	863.509	-100	7.19445
6.a	260.888	44.518	67.3943	5.53123	326.435	93.0579	838.732	-94.5099	3.30018
6.b	210.78	43.6217	76.1352	6.15418	295.782	92.5809	1018.47	-84.6752	3.44085
6.c	163.651	74.5816	65.1867	12.2322	312.628	136.837	722.117	-225.006	4.70573
7.a	271.697	32.0095	10.7158	1.89115	306.095	106.845	729.139	-130.917	3.72187
7.b	592.027	77.1816	1016.13	19.0921	275.335	86.2301	951.69	-57.5557	5.14022
7.c	176.781	66.9682	30.1261	8.53341	325.503	183.668	555.988	-338.524	4.91036
8.a	285.304	34.5421	44.2448	12.0393	304.405	100.756	718.048	-125.417	3.21602
8.b	550.962	80.078	690.258	1.70757	276.205	79.7407	990.28	-41.1569	3.10199
8.c	5.00E-05	53.654	400	5.75655	362.409	151.079	495.397	-304.048	3.17402
9.a	538.738	73.3486	110.504	17.317	306.555	155.461	495.909	-225.256	4.45146
9.b	614.273	81.8197	859.226	10.1382	290.435	89.2885	901.286	-62.1683	4.02308
9.c	177.464	73.1206	81.2464	16.8467	346.949	133.681	668.274	-235.282	3.02846
10.a	374.601	6.08884	276.262	9.51061	326.714	92.1335	761.324	-80.0865	2.62972
10.b	657.046	63.3134	1170.38	17.4194	297.797	88.9172	909.432	-64.3405	3.8658
10.c	179.054	61.8746	62.4029	14.0377	333.6	121.902	653.54	-197.447	3.35924
11.a	304.481	46.1969	63.1509	6.67815	317.968	94.0586	865.909	-99.611	3.01889
11.b	618.99	60.9061	438.816	12.0911	288.678	107.326	739.094	-114.904	5.36836
11.c	126.95	14.8822	308.329	6.26466	335.048	86.1412	842.153	-88.7266	2.44171
12.a	538.486	65.6796	226.419	16.2594	313.173	228.731	531.89	-397.326	4.85854
12.b	266.53	58.5087	37.5592	10.8635	303.816	109.497	904.041	-124.466	4.9717
12.c	177.968	57.5333	95.4664	9.04836	341.336	115.189	774.473	-197.294	3.12856
13.a	388.559	56.4597	273.885	5.59707	361.975	213.984	780.414	-459.377	5.01585
13.b	270.064	37.8563	59.228	6.16521	307.22	108.839	999.339	-142.099	4.56825
13.c	122.88	99.9607	261.697	24.0569	364.359	206.629	558.648	-472.87	4.50562

BIBLIOGRAPHY

[1] Frazier W.E. (2014). "Metal additive manufacturing: A review". *Journal of Materials Engineering and Performance*, 23(6):1917-28.

[2] Lutjering G. (1998). "Influence of processing on microstructure and mechanical properties of $\alpha + \beta$ titanium alloys." *Materials Science and Engineering: A*, 243(1-2):32-45.

[3] Semiatin S.L., Seetharaman V., Weiss I. (1996). "The thermomechanical processing of alpha/beta titanium alloys." *Journal of Materials*, 49(6):33-39.

[4] Kobryn P. A., Semiatin S.L. (2003). "Microstructure and texture evolution during solidification processing of Ti-6Al-4V." *Journal of Materials Processing Technology*, 135:330-339.

[5] RMI Titanium Company (2000). "Titanium Alloy Guide." RMI Titanium Company an RTI International Metals, Inc. Company, pp. 1-45.

[6] Lutjering G., Williams J. C. (2003). "Titanium." (New York:Springer).

[7] Leyens C., Peters M. (2003). "Titanium and titanium alloys." (Germany:Wiley-VCH Verlag).

[8] Welk B. A. (2010). "Microstructural and property relationships in titanium alloy Ti-5553." (Electronic Thesis or Dissertation). The Ohio State University. Retrieved from https://etd.ohiolink.edu/.

[9] Tiley J. (2003). "Modeling of microstructure-property relationships in Ti-6Al-4V." (Electronic Thesis or Dissertation). Retrieved from https://etd.ohiolink.edu/.

[10] Beese A. M. et al. (2015). "Anisotropic tensile behavior of Ti-6Al-4V components fabricated with directed energy deposition additive manufacturing." *Acta Materialia*, 87:309-320.

[11] Collins P. (2004). "A combinatorial approach to the development of composition-microstructure-property relationships in titanium alloys using directed laser deposition." (Electronic Thesis or Dissertation). The Ohio State University. Retrieved from https://etd.ohiolink.edu/.

[12] Baufeld B., Van der Biest O. Gault R. (2010). "Additive manufacturing of Ti-6Al-4V components by shaped metal deposition: Microstructure and mechanical properties." *Materials and Design*, 31:S106-S1116.

[13] Wang F., Williams S., Colegrove P., Antonysamy A. A. (2013). "Microstructure and mechanical properties of wire and arc additive manufactured Ti-6Al-4V." *Metallurgucal and Materials Transactions A*, 44A:968-977.

[14] Gockel B. T. (2016). "Constitutive Response of a Near-Alpha Titanium Alloy as a Function of Temperature and Strain Rate." The Ohio State University. (Electronic Thesis or Dissertation), Carnegie Mellon University.

[15] Zhai Y., Galarraga H., Lados D.A. (2015). "Microstructure Evolution, Tensile Properties, and Fatigue Damage Mechanisms in Ti-6Al-4V Alloys Fabricated by Two Additive Manufacturing Techniques." *Procedia Engineering*, 114:658-666.

[16] Murr L. E., Esquivel E.V. et al. (2009). "Microstructures and mechanical properties of electron beam-rapid manufactured Ti-6Al-4V biomedical prototypes compared to wrought Ti-6Al-4V." *Materials Characterization*, 60:96-105.

[17] Wang P., Nai M. L. S., Sin W. J., Wei J. (2015). "Effect of building height on microstructure and mechanical properties of big-sized Ti-6Al-4V plate fabricated by electron beam melting." *MATEC Web Conf.*, 30:02001

[18] Hook J. R. and Hall H. E. (2010). "Solid State Physics." (West Sussex, England: John Wiley & Sons).

[19] Callister W. D., Rethwisch D. G. (2010). "Materials Science and Engineering: An Introduction." (New York: John Wiley & Sons).

[20] Kocks U. F., Tome, C. N., Wenk, H. R. (2000). "Texture and anisotropy: preferred orientations in polycrystals and their effect on materials properties." (Cambridge: Cambridge University Press).

[21] Schwartz A. J., Kumar M., Adams B. L., Field D. P. (2000) "Electron Backscatter Diffraction in Materials Science." New York:Springer.

[22] Bunge, H. J. (1965). "Zur darstellung allgemeiner texturen." *Zeitschrift Fur Metallkunde*, 56(12): 872-874.

[23] Roe R. J. (1965). "Description of crystallite orientation in polycrystalline Materials III, general solution to pole figure inversion." *Journal of Applied Physics*, 36(6): 2024-2031.

[24] Kocks U. F. (1988). "A symmetric set of Euler angles and oblique orientation space sections." *Eighth International Conference on Textures of Materials*, (Warrendale,PA:TMS), 31-36.

[25] Courtney, T. H. (2000). "Mechanical behavior of materials." (New York: McGraw-Hill).

[26] Tome C. N. et al. (2007). "Self-consistent modelling of the mechanical behaviour of viscoplastic polycrystals incorporating intragranular field fluctuations." *Philosophical Magazine*, DSL WC.

[27] Voigt W. (1887). "Theoretische Studien ber die Elasticittsverhltnisse der Krystalle." *Abh.Kgl.Ges.Wiss.Gttingen, Math.Kl.*, 34: 3-51.

[28] Reuss A. (1929). "Berechnung der Fliegrenze von Mischkristallen auf Grund der Plastizittsbedingung fr Einkristalle." *Journal of Applied Mathematics and Mechanics*, 9: 49-58

[29] Hill R. (1965). "A Self-Consistent Mechanics of (Warrendale,PA:TMS) Materials." *J.Mech.Phys.Sol.*, 13:213-222.

[30] Mori T., Tanaka K. (1973). "Average Stress in the Matrix and Average Elastic Energy of Materials with Misfitting Inclusions." *Acta metall.*, 21:571-574.

[31] Sachs G. (1928). "Plasticity problems in metals." *Trans. Faraday Soc.*, 24:84-92.

[32] Taylor G. I. (1938). "Plastic strain in metals." *Journal of the Institute of Metals*, 62:307-324

[33] Prakash A., Lebensohn R.A. (2009) "Simulation of micromechanical behavior of polycrystals: finite elements versus fast Fourier transforms." *Modelling and Simulation in Materials Science and Engineering*, 17:064010.

[34] Lebensohn R.A. (2001). "N-site modeling of a 3D viscoplastic polycrystal using Fast Fourier Transform." *Acta Materialia*, 49:2723-37.

[35] Donachie M. J. (2000). "Titanium: A technical guide." ASM International, The Minerals Information Society.

[36] Gammon L. M., Briggs R. D., Packard J. M. et al. (2004). "Metallography and microstructures of titanium and its alloys." *ASM Handbook*, 9:899-917.

[37] Ahmed T., Rack H. J. (1998). "Phase transformations during cooling in $\alpha+\beta$ titanium alloys." *Materials Science and Engineering A*, 243(1-2):206-211.

[38] Swarnakar A. K., Van der Biest O., Baufeld B. (2010). "Thermal expansion and lattice parameters of shaped metal deposited Ti-6Al-4V." *Journal of Alloys and Compounds*, 509(6):2723-28.

[39] Bhattacharyya D., Viswanathan G. B., Denkenberger R., Furrer D. Fraser H. L. (2003). "The role of crystallographic and geometrical relationships between α and β phases in an $\alpha-\beta$ titanium alloy." *Acta Materialia*, 51(16):4679-4691.

[40] Stanford N., Bate P. S. (2004). "Crystallographic variant selection in Ti-6Al-4V." *Acta Materialia*,52(17):5215-5224.

[41] Obasi G. C., Birosca S., Quinta da Fonseca J., Preuss M. (2012). "Effect of β grain growth on variant selection and texture memory effect during $\alpha-\beta-\alpha$ phase transformation in Ti-6 Al-4V." *Acta Materialia*, 60(3):1048-1058.

[42] McHargue C. J. (1953). "The crystallography of the titanium transformation." *Acta Crystallographica*, 6(6):529-530.

[43] Karthikeyan T., Saroja S., Vijayalakshmi M. (2006) "Evaluation of misorientation angle-axis set between variants during transformation of bcc to hcp phase obeying burgers orientation relation." *Scripta Materialia*, 55(9):771 Ð 774.

[44] Bieler T.R., Semiatin S.L. (2002). "The origins of heterogeneous deformation during primary hot working of Ti-6Al-4V." *International Journal of Plasticity* 18(9):1165-1189.

[45] Smith W. F. (1981). "Structure and Properties of Engineering Alloys." (New York: McGraw-Hill).

[46] Dunst D., Mecking H. (1996). "Analysis of experimental and theoretical rolling textures of two-phase titanium alloys." *Z. Metallkde* 87, 498-507.

[47] Lebensohn R. A., Canova G. R. (1997). "A self-consistent approach for modelling texture development of two-phase polycrystals: application to titanium alloys." *Acta Materialia* 45, 3687-3694.

[48] Bieler T. R., Semiatin S. L. (2001). "The effect of crystal orientation and boundary misorientation on tensile boundary cavitation during hot tensile deformation of Ti-6Al-4V." *Lightweight Alloys for Aerospace Applications VI* (Warrendale,PA:TMS),161-170.

[49] Hall E.O. (1951). "The deformation and ageing of mild steel: III Discussion of results." *Proc. Phys. Soc. B* 64:747-753.

[50] Petch N.J. (1953). "The cleavage strength of polycrystals." *J. Iron Steel Institute* 174:25-28.

[51] Bache M. R., Evans W. J. (2001). "Impact of texture on mechanical properties in an advanced titanium alloy." *Materials Science and Engineering A* A319-321:409-414.

[52] Gupta R. K., Kumar V. A., Mathew C., Rao G. S. (2016). "Strain hardening of Titanium alloy Ti6Al4V sheets with prior heat treatment and cold working." *Materials Science and Engineering A* 662:537-550.

[53] Chen G., Ren C., Qin X., Li J. (2015). "Temperature dependent work hardening in Ti-6Al-4V alloy over large temperature and strain rate ranges: Experiments and constitutive modeling." *Materials and Design* 83:598-610.

[54] Venkatesh B. D., Chen D. L., Bhole S. D. (2009). "Effect of heat treatment on mechanical properties of Ti-6Al-4V ELI alloy." *Materials Science and Engineering A* 506:117-124.

[55] Galan-Lopez J., Naghdy S., Verleysen P., Kestens L. A. I. et al. (2015). "Mechanical behavior and texture prediction of Ti-6Al-4V based on elastic viscoplastic self-consistent modelling." *IOP Conf. Series: Materials Science and Engineering* 82:012027.

[56] Collins P. C., Haden C. V., Ghamarian I., Hayes B. J. et al. (2014). "Progress Toward an Integration of Process-Structure-Property-Performance Models for Three-Dimensional (3-D) Printing of Titanium Alloys." *JOM* 66(7):1299-1309.

[57] Glavicic M. G., Goetz D. R., Barker D. R., Shen G. (2008). "Modeling of Texture Evolution during Hot Forging of Alpha/Beta Titanium Alloys." *Metallurgical and Materials Transactions A* 39(4):887.

[58] Shi X., Zeng W., Sun Y., Han Y. et al. (2015). "Microstructure-Tensile Properties Correlation for the Ti-6Al-4V Titanium Alloy." *Journal of Materials Engineering and Performance* 24:1754-1762.

[59] Barton N. R., Dawson P. R. (2001). "On the spatial arrangement of lattice orientations in hot-rolled multiphase titanium." *Modelling Simul. Mater. Sci. Eng.* 9:433-463.

[60] Venkataramani G., Kirane K., Ghosh S. (2008). "Microstructural parameters affecting creep induced load shedding in Ti-6242 by a size dependent crystal plasticity FE model." *International Journal of Plasticity*, 24:428-454.

[61] Thomas J., Groeber M., Ghosh S. (2012). "Image-based crystal plasticity FE framework for microstructure dependent properties of Ti-6Al-4V alloys." *Materials Science and Engineering A*, 553:164-175.

[62] Zhang M., Zhang J., McDowell D.L. (2007). "Microstructure-based crystal plasticity modeling of cyclic deformation of Ti-6Al-4V." *International Journal of Plasticity*, 23:1328-1348.

[63] Przybyla C.P., McDowell D.L. (2010). "Simulation-based extreme value marked correlations in fatigue of advanced engineering alloys." *Procedia Engineering*, 2:1045-1056.

[64] Murr L. E., Martinez K.N., Amato S.M. et al. (2012). "Fabrication of metal and alloy components by additive manufacturing: Examples of 3D materials science." *Journal of Materials Research and Technology*, 1(1):42-54.

[65] Huang R., Riddle M., Graziano D. et al. (2016). "Energy and emissions saving potential of additive manufacturing: theÊcase of lightweight aircraft components." *Journal of Cleaner Production*, 135:1559-157.

[66] Korner C. (2016). "Additive manufacturing of metallic components by selective electron beam melting - a review." *International Materials Reviews*, 61(5)-361-377.

[67] Seifi M., Salem A., Satko D., Shaffer J., Lewandowski J, J. (2017). "Defect distribution and microstructure heterogeneity effects on fracture resistance and fatigue behavior of EBM Ti-6Al-4V." *International Journal of Fatigue*, 94:263-287.

[68] Cunningham R., Narra S. P., Ozturk T., Beuth J., Rollett A. D. (2016). "Evaluating the effect of processing parameters on porosity in electron beam melted Ti-6Al-4V via synchrotron x-ray microtomography." *JOM*, 68(3):765-771.

[69] Seifi M., Salem A., Satko D., Shaffer J., Lewandowski J, J. (2015). 'XCT analysis of the influence of melt strategies on defect population in Ti-6Al-4V components manufactured by selective electron beam melting." *Materials Characterization*, 102:47-61.

[70] Gong H., Gu H., Zeng K., Dilip J. J. S. et al. (2014). "Melt pool characterization for selective laser melting of Ti-6Al-4V pre-alloyed powder." *Solid Freeform Fabrication Proceedings*, 256-267.

[71] Dutta B., Froes FHS. (2014). "Additive manufacturing of titanium alloys." *Adv. Mater. Res*, 1019:19-25.

[72] Facchini L., Magalini M., Robotti P., Molinari A. (2009). "Microstructure and mechanical properties of Ti-6Al-4V produced by electron beam melting of pre-alloyed powders." *Rapid Prototyping Journal* 15(3):171-178.

[73] McLouth T., Chang Y., Wooten J., Yang J. (2015). "The effects of electron beam melting on the microstructure and mechanical properties of Ti-6Al-4V and γ-TiAl." *Microsc. Microanal.*, 21(588):1177-1178.

[74] Edwards P., O'Conner A., Ramulu M. (2013). "Electron beam additive manufacturing of titanium components: properties and performance." *J. Manuf. Sci. Eng.*, 135(6):061016.

[75] Ackelid U., Svensson M. (2009). "Additive manufacturing of dense metal parts by electron beam melting." *In Materials Science and Technology Proceedings*, 2711-2719.

[76] Hrabe N., Quinn T. (2013). "Effects of processing on microstructure and mechanical properties of a titanium alloy (Ti-6Al-4V) fabricated using electron beam melting (EBM). Part 2. Energy input, orientation, and location." *Materials Science and Engineering A*, 573:271-277.

[77] Rafi K., Karthik N., Starr T.L., Stucker B.E. (2012). "Mechanical property evaluation of Ti-6Al-4V parts made using electron beam melting." *Solid Freeform Fabrication Proceedings*, 526-535.

[78] Shunmugavel M., Polishetty A., Littlefair G. (2015). "Microstructure and mechanical properties of wrought and Additive manufactured Ti-6Al-4V cylindrical bars." *Procedia Technology*, 20:231-236.

[79] Seifi M., Lewandowski J. J. (2016). "Metal Additive Manufacturing: A Review of Mechanical Properties." *Annual Review of Materials Research*, 46:151-186.

[80] Al-Bermani S.S, Blackmore M.L., Zhang W., Todd I. (2010). "The Origin of Microstructural Diversity, Texture, and Mechanical Properties in Electron Beam Melted Ti-6Al-4V." *Metallurgical and Materials Transactions A*, 41(13):3422-3434.

[81] Tan X., Kok Y., Toh W. Q. et al. (2010). "Revealing martensitic transformation and α/β interface evolution in electron beam melting three-dimensional-printed Ti-6Al-4V." *Scientific Reports*, 6:26039.

[82] Antonysamy A.A., Meyer J., Prangnell P.B. (2013). "Effect of build geometry on the β-grain structure and texture in additive manufacture of Ti-6Al-4V by selective electron beam melting." *Materials Characterization*, 84:153-168.

[83] Lu S. L., Tang H. P., Ning Y. P. et al. (2015). "Microstructure and Mechanical Properties of Long Ti-6Al-4V Rods Additively Manufactured by Selective Electron Beam Melting Out of a Deep Powder Bed and the Effect of Subsequent Hot Isostatic Pressing." *Metallurgical and Materials Transactions A*, 46A:3824-3834.

[84] Tan X., Kok Y., Tan Y. J. et al. (2015). "Graded microstructure and mechanical properties of additive manufactured Ti-6Al-4V via electron beam melting." *Acta Materialia*, 97:1-16.

[85] Germain L., Gey N., Humbert M. (2007). "Reliability of reconstructed ğ-orientation maps in titanium alloys." *Ultramicroscopy*, 107:1129-1135.

[86] Bontha S., Klingbeil N.W., Kobryn P.A., Fraser H.L. (2009). "Effects of process variables and size-scale on solidification microstructure in beam-based fabrication of bulky 3D structures." *Materials Science and Engineering A*, 513-514:311-318.

[87] Gockel J., Beuth J. (2013). "Understanding Ti-6Al-4V Microstructure Control in Additive Manufacturing via Process Maps." *Solid Freeform Fabrication Proceedings*, 666-674.

[88] Eshelby J.D. (1957). "The Determination of the Elastic Field of an Ellipsoidal Inclusion and Related Problems." *Proceedings of the Royal Society of London Series A - Mathematical Physical and Engineering Sciences*, A241:376-396.

[89] Molinari A., Canova G.R., Ahzi S. (1987). "A self consistent approach of the large deformation polycrystal viscoplasticity." *Acta Metallurgica*, 35:2983-94.

[90] Lebensohn R.A., Turner P.A., Signorelli J.W., Canova G.R., Tomé S.N. (1998). "Calculation of intergranular stresses based on a large-strain viscoplastic self-consistent polycrystal model." *Modelling and Simulation in Materials Science and Engineering*, 6(4):447-65.

[91] Moulinec H., Suquet P. (1998). "A numerical method for computing the overall response of nonlinear composites with complex microstructure." *Computer Methods in Applied Mechanics and Engineering*, 157(1-2):69-94.

[92] Lebensohn R.A., Liu Y., Ponte Castañeda P. (2004). "On the accuracy of the self-consistent approximation for polycrystals:comparison with full-field numerical simulations." *Acta Materialia*, 52:5347-61.

[93] Lebensohn R.A., Kanjarla A.K., Eisenlohr P. (2012). "An elasto-viscoplastic formulation based on fast fourier transforms for the prediction of micromechanical fields in polycrystalline materials." *International Journal of Plasticity*, 32:59-69.

[94] Mura T. (1988). "Micromechanics of Defects in Solids." (Dodrecht: Martinus-Nijhoff)

[95] Voce E. (1955). "A practical strain hardening function." *Metallurgia* 51:219-226.

[96] Groeber M.A., Ghosh S., Uchic M.D., Dimiduk D.M. (2007). "Developing a robust 3-D characterization-representation framework for modeling polycrystalline materials." *Journal of Materials*, 59(9):32-36.

[97] Pokharel R., Lind J., Kanjarla A. K. et al. (2014). "Polycrystal Plasticity: Comparison Between Grain Scale Observations of Deformation and Simulations." *The Annual Review of Condensed Matter Physics*, 5:317-246.

[98] Ozturk T. et.al. (2016). "Simulation domain size requirements for elastic response of 3D polycrystalline materials." *Modelling and Simulation in Materials Science and Engineering*, 24:-015006.

[99] Turner T. J., Shade P. A., Bernier J. V. et al. (2017). "Crystal Plasticity Model Validation Using Combined High-Energy Diffraction Microscopy Data for a Ti-7Al Specimen." *Metallurgical and Materials Transactions A*, 48:-627.

[100] Pokharel R., Lebensohn R. A. (2017). "Instantiation of crystal plasticity simulations for micromechanical modelling with direct input from microstructural data collected at light sources." *Scripta Materialia*, 132:-73-77.

[101] Lienert U., Li S. F., Hefferan C. M. et al. (2011). "High-energy diffraction microscopy at the advanced photon source." *JOM*, 63(7):70-77.

[102] Ludwig W., Reischig P., King A. et al. (2009). "Three-dimensional grain mapping by x-ray diffraction contrast tomography and the use of friedel pairs in diffraction data analysis." *Review of Scientific Instruments*, 80(3):033905.

[103] Larson B. C., Yang W., Ice G. E., et al. (2002). "Three dimensional x-ray structural microscopy with submicrometre resolution." *Nature* 15(6874):887-890.

[104] Poulsen H. F. (2004). "Three-dimensional X-ray diffraction microscopy: mapping polycrystals and their dynamics." (Germany:Springer).

[105] Suter R. M. et al. (2006). "Forward modeling method for microstructure reconstruction using x-ray diffraction microscopy: Single-crystal verification." *Review of Scientific Instruments*, 77(12):123905.

[106] Suter R. M. et al. (2008) "Probing Microstructure Dynamics With X-Ray Diffraction Microscopy." *Journal of Engineering Materials and Technology*, 130(2):021007.

[107] Li S.F., Suter R.M. (2013). "Adaptive reconstruction method for three-dimensional orientation imaging." *Journal of Applied Crystallography*, 46: 512-24.

[108] Menasche D. (2016). "Error Analysis of near-field High Energy Diffraction Microscopy." (Electronic Thesis or Dissertation), Carnegie Mellon University.

[109] Li S. F. "IceNine." https://github.com/FrankieLi/IceNine.

[110] Miller M. P. et al. (2005). "Experimental measurement of lattice strain pole figures using synchrotron X-rays." *Review of Scientific Instruments*, 39:358-368.

[111] Murr L. E., Esquivel E.V. et al. (2009). "Microstructures and mechanical properties of electron beam-rapid manufactured Ti-6Al-4V biomedical prototypes compared to wrought Ti-6Al-4V." *Materials Characterization*, 60:96-105.

[112] Machry T., Eatock D., Meyer J. et al. (2016). "Effect of microstructure on the tensile strength of Ti6Al4V specimens manufactured using additive manufacturing electron beam process." *Powder Metallurgy*, 59:41-50.

[113] Beuth J. and Klingbeil N. (2001). "The Role of Process Variables in Laser-Based Direct Metal Solid Freeform Fabrication." *JOM*, 53(9):36-39.

[114] Narra S. P., Cunningham R., Christiansen D. et al. (2015). "Toward Enabling Spatial Control of Ti-6Al-4V Solidification Microstructure in the Electron Beam Melting Process." *Proceedings of Solid Freeform Fabrication Symposium*, 626-635.

[115] Wielewski E., Menasche D., Callahan P., Suter R. M. (2015). "3-D alpha colony characterisation and prior-beta grain reconstruction of a lamellar Ti-6Al-4V specimen using near-field high energy x-ray diffraction microscopy." *Journal of Applied Crystallography*, 48:116501171.

[116] Ranger C., Tari V., Farjami S., et al. "Austenite Reconstruction Elucidates Prior Grain Size Dependence of Toughness in a Low Alloy Steel.", in preparation.

[117] Mandal S. et al. (2017). "Simulation of plastic deformation in Ti-5553 alloy using a self-consistent viscoplastic model." *International Journal of Plasticity*, in press.

[118] Ghosh S., Dimiduk D. (2011). "Computational Methods for Microstructure-Property Relationships." (New York: Springer). 1:199-238, 393-441.

[119] Gusev, A. A. (1997). "Representative volume element size for elastic composites: A numerical study." *Journal of the Mechanics and Physics of Solids*, 45(9):1449-1459.

[120] Kanit T. et al. (2003). "Determination of the size of the representative volume element for random composites: statistical and numerical approach." *International Journal of Solids and Structures*, 40:3647-3679.

[121] Ammar K., Appolaire B., Cailletaud G., Forest S. (2009). "Combining phase field approach and homogenization methods for modelling phase transformation in elastoplastic media." *European Journal of Computational Mechanics*, 18(5-6):485-523.

[122] Nakamachi E., Tam, N.N., Morimoto H. (2006). "Multi-scale finite element analyses of sheet metals by using SEM-EBSD measured crystallographic RVE models." *International Journal of Plasticity*, 23:450-489.

[123] Boyle K.P., Curtin W. A. (2005). "Grain Interactions in Crystal Plasticity." *NUMISHEET2005*, 778:433-438.

[124] Stein C., Lee S., Rollett A. (2012). "An analysis of fatigue crack initiation using 2D orientation mapping and full-field simulation of elastic stress response." *Superalloys 2012* (Hoboken: Wiley & Sons).

[125] Stein C. et al. (2014). "Fatigue crack initiation, slip localization and twin boundaries in a nickel-based superalloy." *Current Opinion in Solid State and Materials Science*, 18:244-252.

[126] Gabb T. P. et al. (2005). "Thermal and mechanical property characterization of the advanced disk alloy LSHR." *NASA/TM*, 2005-213645.

[127] Cerrone et al. (2015). "Implementation and verification of a microstructure-based capability for modeling microcrack nucleation in LSHR at room temperature." *Modelling and Simulation in Materials Science and Engineering*, 23(3):035006.

[128] Semiatin S.L., Air Force Research Laboratory, Materials and Manufacturing Directorate, Wright-Patterson AFB, OH 45433. Unpublished results.

[129] Marrow T.J. et al. (2004). "High resolution X-ray tomography of short fatigue crack nucleation in austempered ductile cast iron." *International Journal of Fatigue* 26: 717-725.

[130] Ludwig W., Buffiere J-Y., Savelli S., Cloetens P. (2003). "Study of the interaction of a short fatigue crack with grain boundaries in a cast Al alloy using X-ray microtomography." *Acta Materialia*, 51: 585-598.

[131] Navidi W. (2011). "Statistics for Engineers and Scientists." (New York: McGraw-Hill).

[132] Miao J., Pollock T. M., Wayne Jones J. (2009). "Crystallographic fatigue crack initiation in nickel-based superalloy Rene 88DT at elevated temperature." *Acta Materialia*, 57(20):5964-74.

[133] Gabb T. P., Telesman J., Banik A., McDevitt E. (2014). "Use of Slow Strain Rate Tensile Testing to Assess The Ability of Several Superalloys to Resist Environmentally-Assisted Intergranular Cracking." *NASA/TM*, 2014-0017059.

[134] Kanit T., Forest S., Galliet I. Mounoury D. Jeulin D. (2003). "Determination of the size of the representative volume element for random composites: statistical and numerical approach." *International Journal of Solids and Structures*, 40(13-14):3647-3679.

[135] Fan Z.G., Wu Y., Zhao X., Lu Y. (2004). "Simulation of polycrystalline structure with Voronoi diagram in Laguerre geometry based on random closed packing of spheres." *Computational Materials Science*, 29(3):301-308.

[136] Groeber M.A., Ghosh S., Uchic M.D., Dimiduk D.M. (2008). "A framework for automated analysis and simulation of 3D polycrystalline microstructures. Part 2: Synthetic structure generation." *Acta Materialia*, 56(6):1274-1287.

[137] Saylor D.M., Fridy J., El-Dasher B.S., Jung K.Y., Rollett A.D. (2004). "Statistically representative three-dimensional microstructures based on orthogonal observation sections." *Metallurgical and Materials Transactions A*, 35A(7):1969-1979.

[138] Simonelli M., Tse Y.Y., Tuck C. (2012). "Further understanding of Ti-6Al-4V selective laser melting using texture analysis." *Solid Freeform Fabrication Proceedings*, 480-491.

[139] Gong X., Lydon J., Cooper K., Chou, K. (2014). "Beam speed effects on Ti-6Al-4V microstructures in electron beam additive manufacturing." *Journal of Materials Research*, 29(17):1951-1959.

[140] Nassar A.R., Reutzel E.W. (2015). "Additive Manufacturing of Ti-6Al-4V Using a Pulsed Laser Beam." *Metallurgical and Materials Transactions A*, 46(6):2781-2789.

[141] Elmer J.W., Palmer T.A., Babu S.S, Zhang W., DebRoy T. (2004). "Phase transformation dynamics during welding of Ti-6Al-4V." *Journal of Applied Physics*, 95(12):8327-8339.

[142] Groeber M.A., Jackson M. (2014). "DREAM.3D: A digital representation environment for the analysis of microstructure in 3D." *Integrating Materials and Manufacturing Innovation*, 3:5.

[143] Stapleton A.M. et al. (2008). "Evolution of lattice strain in Ti-6Al-4V during tensile loading at room temperature." *Acta Materialia* 56:6186-6196.

[144] Werner E., Wesenjak R., Fillafer A., Meier F., Krempaszky C. (2016). "Microstructure-based modelling of multiphase materials and complex structures." *Continuum Mechanics and Thermodynamics*, 28:1325-1346.

[145] Lind J. (2013). "In-situ High-Energy Diffraction Microscopy Study of Zirconium Under Uniaxial Tensile Deformation." (Electronic Thesis or Dissertation), Carnegie Mellon University.